Coulomb drag in high-mobility quantum wires and short quantum wires

Simon Bilodeau

Master of Science

Department of Physics

McGill University

Montréal, Québec, Canada

August 2018

A thesis submitted to McGill University in partial fulfillment of the degree of Master of Science

À mes parents, qui m'ont tout donné, et Marie-Joëlle qui m'a aussi longtemps soutenu.

Acknowledgements

First and foremost, I want to thank Dr. Dominique Laroche without whom this project would have been written off as impossible long ago. I am grateful for the devices used in this work and your excellent and patient mentoring. I am also indebted to your great company when I was far from home in Florida and New Mexico, be it during long days at the lab or when pausing for a "Classique Panda". Your future students will be very fortunate to have you as a supervisor.

Speaking of mentors, I can never thank Benjamin Schmidt enough for always being eager to come in to provide guidance about all aspects of low temperature physics. Similarly, I thank Dr. Keyan Bennaceur for demystifying the cleanroom and his early teachings which I have carried ever since.

Gervaislab could not have achieved a fraction of what it did without Pierre-François Duc's energy, enthusiam and efficiency. Thank you for the help with machining, Python, cooldowns, and everything else. Thanks to Matei Petrescu's exquisite care of the apparatus, everything runs more smoothly than could be expected : thank you. Paul Thulstrup, thank you for having diligently followed me in my crazy schemes so long. Finally, thank you Oulin Yu, Eli Gerber, Olivier Cyr-Choinière, and Samuel Gaucher for all the technical assistance you gave me, and thank you Eli Martel, Simon Bernier, Qian Luo, Camille Bowness, Chunwei Hsu, and countless others for also having made Gervaislab such a homely place.

Gervaislab is more than Lab 019. Thank you John Smeros, Robert Gagnon and Richard Talbot for always going above and beyond to help and give advice, especially in an "installation-heavy" timeframe like the last few years. Specific thanks are extended to Richard Talbot for having so generously provided his technical drawing expertise. John Li and Sasa Ristic's technical assistance in the cleanroom also deserves recognition.

Large amounts of this M.Sc. were conducted outside of Rutherford Physics. Thank you Alexander Vlasov and Prof. Thomas Szkopek for making my brief stint in McConnell so painless. I thank the staff of the Center for Integrated Nanotechnologies for making my stay there so productive, and I thank Dr. Jian-Sheng Xia and Prof. Neil Sullivan of the Microkelvin

Facility for providing the technical assistance, equipment, and helium necessary to attempt running all of our experiments. Special thanks are also extended to our collaborators at Sandia and Princeton without whom none of this would have been possible.

On another note, I want to thank all the family and friends, too many to name, who have walked by my side through the ups and downs of the last few years.

Last but not least, I thank my supervisor Prof. Guillaume Gervais for his unconditional support throughout this endeavour. Your tireless efforts to sustain a world-class laboratory while offering daily guidance do not go unnoticed. Thank you for having provided so many opportunities to a young unassuming student. My time in your lab has toughened me and sharpened my spirit. I am certain this will be of great use in any challenges the future holds.

Finally, I acknowledge that portions of this work were performed, in part, at the National High Magnetic Field Laboratory, which is supported by National Science Foundation Cooperative Agreement No. DMR-1157490 and the State of Florida, as well as at the Center for Integrated Nanotechnologies, a U.S. DOE Office of Basic Energy Sciences user facility. Sandia National Laboratories is a multi-program laboratory managed and operated by Sandia Corporation, a wholly owned subsidiary of Lockheed Martin Corporation, for the U.S. Department of Energy's National Nuclear Security Administration under contract DE-AC04-94AL85000. I also acknowledge financial support from the Natural Sciences and Engineering Research Council of Canada (NSERC), from the Fonds Québécois de la Recherche sur la Nature et les Technologies (FQRNT), and from McGill University, specifically the Physics department and the Wolfe Chair in Scientific and Technological Literacy.

Abstract

When electrons are constrained to one dimension, interparticle interactions should become a determining feature for the underlying quantum ground state. In essence, the effectively non-interacting *Fermi liquid* description ubiquitous in higher dimensions is expected to fail. In its stead, the strongly-interacting *Luttinger liquid* theory has been proposed, and is remarkable in that it is a mathematically exact theory. Discerning the genuine interaction-induced Luttinger liquid physics from the surrounding Fermi liquid environment has shown difficult in experiments.

A promising approach is to probe not a single one-dimensional wire, but a set of coupled wires. In this case, signals will necessarily be due to interactions between the electronic systems in the wires, therefore magnifying the impact of electron-electron interactions. *Coulomb drag*, that is the appearance of a voltage in a conductor when a current is driven in a nearby distinct conductor, has in the past yielded results consistent with Luttinger liquid predictions when performed in a set of vertically-integrated quantum wires.

In this thesis, Coulomb drag in such coupled quantum wires is studied in two previously unexplored regimes. The fabrication process and characterization procedure of the devices are maintained from past experiments, yet they are now performed in A) wires with a similar length but defined in a heterostructure with a higher unpatterned mobility, and B) shorter wires with a design similar to the previously-used heterostructure. Similar positive-to-negative high-density drag features as a function of subband occupancy are observed in all types of working devices, demonstrating the robustness to this so-far not fully explained effect. In addition, the effect of bias cooling and light-emitting diode illumination on the high-mobility device are reported. Finally, a lower magnitude of the drag signal was observed in the shorter wires, which merits further study to check for consistency with theoretical predictions.

Abrégé

Lorsque des électrons sont confinés en une seule dimension, les interactions entre particules devraient devenir de la plus haute importance dans la description de l'état fondamental quantique sous-jacent. Essentiellement, la description de particules indépendantes capturée par le *liquide de Fermi*, omniprésente dans les dimensions supérieures, devrait échouer. À sa place, le *liquide de Luttinger* aux interactions fortes a été proposé, et ce dernier est remarquable de par son exactitude mathématique. Départager entre la physique fortement interactive attribuable au liquide de Luttinger de celle de l'environnement effectivement noninteractif est toutefois difficile expérimentalement.

Une approche prometteuse consiste en l'étude non pas d'un seul fil unidimensionel, mais d'une paire de fils couplés. Dans ce cas, les signaux développés seront nécessairement dus aux interactions entre les systèmes électronique dans les fils, magnifiant l'impact des interactions entre électrons. La *traînée de Coulomb*, c'est-à-dire l'apparition d'une tension dans un conducteur lorsqu'un courant est imposé dans un conducteur distinct à proximité, a par le passé offert des résultats en accord avec les prescriptions du liquide de Luttinger lorsque effectuée entre des fils quantiques verticalement intégrés.

Dans ce mémoire, la traînée de Coulomb entre deux fils quantiques de ce type est étudiée dans deux nouveau régimes. Le processus de fabrication et de caractérisation des dispositifs est maintenu par rapport aux expériences du passé, mais est maintenant effectué avec A) des fils de même longueur, mais définis dans une hétérostructure avec plus haute mobilité de base, et B) des fils plus courts dans un design d'hétérostructure similaire à celui utilisé préalablement. Les oscillations positives-à-négatives à haute densité électronique en fonction de l'occupation des sous-bandes de fils similaires sont observées dans tous les types de dispositifs, ce qui démontre une robustesse à cet effet encore non-totalement expliqué. De plus, l'effet du refroidissement sous biais appliqué et sous illumination sur les couches électronique du dispositif à haute mobilité est rapporté. Finalement, une traînée de Coulomb plus faible qu'à l'habitude a été observée dans les fils plus courts, ce qui mérite une étude plus approfondie pour vérifier la concordance avec les prédictions théoriques.

Contributions

The author's principal contributions were in acquiring and analyzing the data of Ch. 4 and Ch. 5, as well as the ideas on 1D-1D thermoelectricity developed in Appendix E. This work was presented by the author at various conferences. The experiments closely follow the Ph.D. work of Dr. Dominique Laroche, and Ch. 2 and Ch. 3 summarize the theory and methods developed there with additions where warranted. All devices were fabricated at Sandia National Laboratories' Center for Integrated Nanotechnologies, with technical assistance from the staff there.

Device A was fabricated by Dr. Laroche prior to the author's arrival. It was defined in material provided by Dr. Loren Pfeiffer and Ken West of Princeton University. It was characterized by the author at the Microkelvin Facility, and as such the experimental setup used was designed by Dr. Jian-Sheng Xia. Many of the cooldowns during these experimental runs were also performed by the Microkelvin Facility staff, although after some time the author became proficient with the apparatus and did many of the routine manipulations.

Device B was also mainly fabricated by Dr. Laroche, but with assistance from the author. It was defined in material provided by Dr. Mike Lilly and Dr. John Reno of Sandia National Laboratories. It was characterized in a new refrigerator in Prof. Gervais' lab. An experimental stage had to be designed as reported in Appendices B and C. This was performed by the author with assistance by Richard Talbot. The necessary machining was done by the Rutherford Physics machine shop staff, as well as fellow lab members Pierre-François Duc and Oulin Yu.

Contents

Chapter 1

Introduction

Over a hundred years after Planck's initial hypothesis, quantum mechanics still fascinates scientists. This is in large part due to the rich phenomena that become possible when extending the theory to collections of quantum particles allowed to interact and influence each other. Condensed matter physics is concerned with such assemblies in "condensed" phases of matter, for instance liquids or solids. This field has given rise to models explaining the peculiar physics of collective behaviour, often to stunning agreement with experiment, showing that indeed, "more is different" [1]. Such emergent phenomena of collections of particles – and, often, their crucially-important solid-state background – include superconductivity, superfluidity, and the fractional quantum Hall effect, to name only a few.

On the technological side, the field has spawned the band theory of solids which has proven fundamental to the ongoing development of world-altering technologies such as solid-state lasers or transistors. It does, however, only account for the effect of the crystal lattice on individual electrons. In the regime where the effectively non-interacting Fermi Liquid theory is applicable, *i.e.* when particles are free to move as in two or three dimensions, this is a good approximation. However, as downscaling continues to be pursued by the microelectronics industry, the effects of reduced dimensionality are coming into play and the mutual interaction between charge carriers in regular conductors is expected to become non-negligible. Ultimately, Fermi liquid theory is expected to fail. When electrons are purely constrained in one dimension, the strongly-interacting Luttinger liquid theory is seen as <u>the</u> alternative, but experimental investigations of these strong correlations are often stymied by the noninteracting surroundings.

One way to ensure the relevance of electron-electron interactions in experiments is to look at the transconductance between two nearby systems only allowed to interact via the Coulomb potential. Formally known as *Coulomb drag*, this effect now forms an essential tool in the study of electrons in condensed matter systems [2]. A platform was developed by Laroche *et al.* to perform such experiments between independently-contacted and tunable quantum wires [3], thereby allowing Coulomb drag to be performed in the 1D-1D regime [4]. Luttinger Liquid signatures were observed in the drag [5], and forms the basis for further experiments.

In this thesis, Coulomb drag experiments in such systems are presented. The first two chapters are dedicated to reviewing the background and methods relevant this study. Chapters 4 and 5 report new results : Coulomb drag in wires defined in a higher mobility heterostructure, and Coulomb drag in wires shorter than ever studied before in this specific platform. Considerable amount of effort was also spent evaluating the scientific feasability of thermoelectric experiments in the drag devices; this work unrelated to the main thrust of this thesis is summarized in Appendix E.

Chapter 2

Background

Charge transport is semi-classically described by the Drude-Sommerfeld formalism. In this picture, an electric field favours electron motion, but frequent scattering events with the conductor's crystal lead to a linear current density response characterized by a conductivity σ (or equivalently, a conductance G between current and voltage). This model however fails to capture quantum effects that coexist at the frontier between individual atoms and bulk matter. This can be the case because the quantum nature of particles is not completely scrambled by the abovementionned scattering events. Such *mesoscopic* physics include for instance fluctuation, interference, or confinement effects. To engineer a platform for this regime, the relevant scales of this fascinating problem must carefully be considered.

2.1 Mesoscopic transport

The naive application of Schrödinger's equation to an Avogadro's number of pairwise interacting nuclei and electrons required for a "constructionist" calculation of materials' properties will remain computationally intractable for the foreseeable future. As a first simplification, the Born-Oppenheimer approximation exploits the $\sim 10^3$ lighter electron mass as compared to ionic masses to consider the electronic and ionic Hilbert spaces separately [6]. For the electrons, the "slow" ions can then be modeled as a lattice *i.e.* a perfect one-body periodic potential with extraneous scattering terms due to imperfections such as crystal vibrations, defects, or charged impurities. A transport lifetime τ characterizes this scattering.

The problem remains complete, since we are still left with a macroscopic number of mutually interacting fermions. To address this, Landau proposed in the late 1950s the Fermi liquid phenomenology [7]. Resulting from this approach is the remarkable concept of *quasiparticles*, or excited states of the interacting electron liquid characterized by the same quantum numbers

System	n (m^{-d})	T_F (K)	λ_F (m)	μ (cm^2/Vs)	ℓ (m)
Cu ($d = 3$)	$8{\times}10^{28}$	$8{\times}10^{4}$	$5{\times}10^{-10}$	5×10^1 ($\approx 293K$)	4×10^{-8}
High-μ 2DEG ($d = 2$)	$2{\times}10^{15}$	$9{\times}10^{1}$	$6{\times}10^{-8}$	1×10^6 ($\approx 1K$)	$7{\times}10^{-6}$

Table 2.1: Scale of physical quantities associated with electrons in bulk copper (Cu) and a GaAs/AlGaAs high mobility two-dimensional electron gas (High-μ 2DEG). Here, d is the dimension used in calculations, n is the electronic density (intrinsic in the case of Cu and representative of our samples' doping for the 2DEG), T_F and λ_F are the calculated Fermi temperatures and Fermi wavelengths, $\mu \equiv \frac{e\tau}{m_{eff}}$ is a representative electron mobility at the quoted temperature, and $\ell \equiv v_F \tau$ is the associated mean free path for the given μ, material-dependent band mass m_{eff}, and n (via the Fermi velocity v_F).

as the noninteracting electron gas. Within the quasiparticle lifetimes, the physics derived from this solvable model are preserved, most notably the exclusionary filling of bands' single-particle Bloch states leading to a well-defined Fermi surface. Fortunately for the applicability of the theory, a diverging quasiparticle lifetime is expected in 2D and 3D for energy scales (in practice, temperatures) lower than the Fermi energy. The implicit postulate of Drude-Sommerfeld theory, that "electrons" can be treated individually, is thus motivated in many scenarios.

The second key idea of the Drude model is the frequent scattering of the charge carriers. To enter the mesoscopic regime, then the limit of few scattering events must be reached. This implies that the quasiparticle extent of order Fermi wavelength λ_F should be below the τ-dependent mean free path ℓ (as defined in Table 2.1). The length L over which transport occurs should also not exceed ℓ significantly[1]. Furthermore, for quantum confinement effects to be relevant, the transverse dimensions to transport W should also be on the order of λ_F.

Table 2.1 displays these scales for a regular metal and a semiconductor system similar to those used in this work. For the metal, the high electron density implies a large Fermi temperature such that a Fermi liquid is expected even in ambient conditions. The mean free path at these temperatures is however small enough that metals in practically relevant situations behave as classical objects addressable by the Drude model. Yet, because λ_F is on the order of lattice spacing and smaller than ℓ, quantum-sized effects can be observed if electrons are made to cross a region of the metal with $W, L \lesssim 10$ nm, *e.g.* in break-junctions [8]. Historically, the study of mesoscopic transport was first initiated in semiconductors due to their high degree of customizability.

[1] Another key lengthscale, the electron phase relaxation length ℓ_ϕ, is relevant in some contexts. Indeed, it is possible to observe coherent electron physics on lengthscales beyond ℓ if the scattering does not scramble phase information.

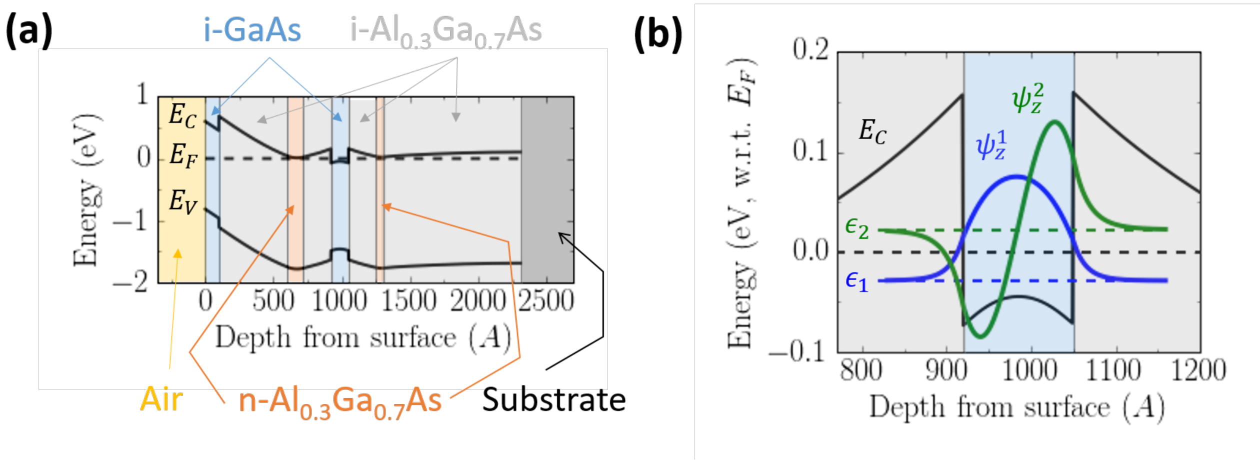

Figure 2.1: (a) Calculated conduction band (E_C, top) and valence band (E_V, bottom) profiles of an example GaAs/$Al_{0.3}Ga_{0.7}As$ modulation-doped symmetric quantum well. The heterostructure layers are color-coded, with the i-label used for intrinsic materials and n- for $10^{18}/cm^3$ silicon doping. (b) Zoom on the quantum well region showing the calculated ground ($n = 1$, blue) and first excited ($n = 2$, green) bound state wavefunctions ψ_z^n (arb. scale) about their energies ϵ_n relative to the Fermi energy E_F. The states are nested in the potential well formed by E_C.

2.1.1 Semiconductor heterostructures

The versatility of semiconductors lies foremost in their eV-range bandgaps. By adjusting the Fermi level, for instance by doping or application of a small gate voltage, conduction can be tuned from hole-dominated, to charge neutral, to electron-dominated. Stacking different semiconductors to form a "heterostructure" allows further control by developing "quasi-electric" forces within the material due to the different bandstructures of the materials and net charge effects [9]. Molecular beam epitaxy reaches the ultimate limit of this idea by achieving atomic resolution of the semiconductor layers along the growth direction.

The application of most interest to us of this technology is the formation of high-mobility GaAs/AlGaAs quantum wells. A representative illustration is given in Fig. 2.1a in terms of design, well size, and electronic density. The specific profiles displayed were obtained with a Schrödinger-Poisson algorithm [10, 11]. The interplay between the more conducting GaAs, more insulating AlGaAs, as well as net charge densities leads to band bending and to the formation in the middling GaAs of a ~ 15 nm conducting layer in the growth direction. This is smaller than the Fermi wavelength, since the converged electron density in the well is estimated to yield a value close to the one given in Table 2.1. Quantization is therefore expected in this direction, and the calculated wavefunctions then reveal bound states confined to the well, as displayed Fig. 2.1b. Occupation of any excited state will be exponentially suppressed below

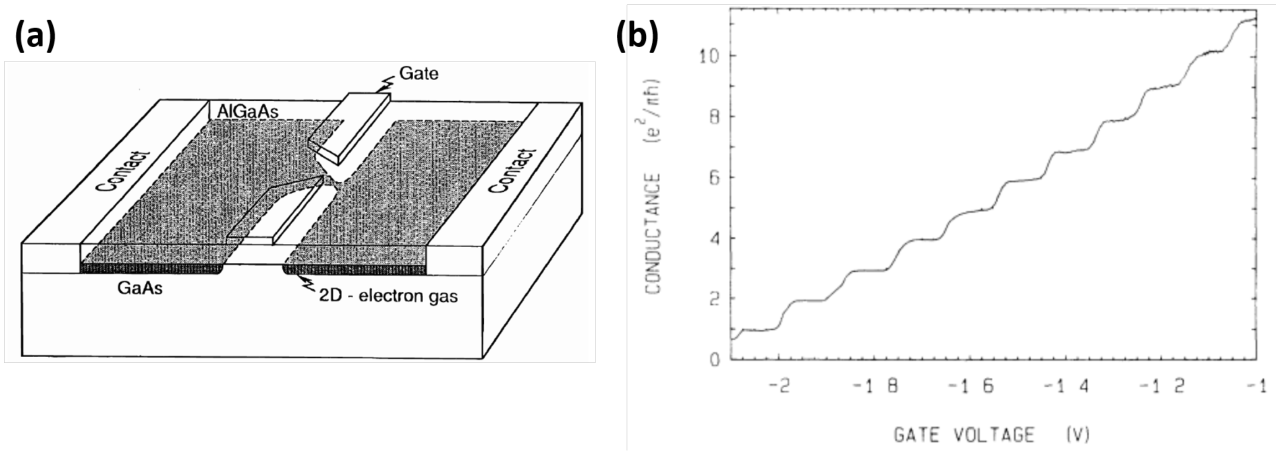

Figure 2.2: (a) Schematic of QPC split-gates over a GaAs quantum well. (b) Conductance of the QPC quantized in units of $e^2/\pi\hbar = 2e^2/h$. Figure from [14].

a temperature $(\epsilon_2 - E_F)/k_B \sim 200$ K, leading to a true 2D system referred to as a two-dimensional electron gas (2DEG) *i.e.* eliminating the z degree of freedom for electrons in the well. Cryogenic temperatures are then required to get the degenerate, 2D Fermi liquid behaviour, *e.g.* $T < T_F \approx 90$ K as calculated in Table 2.1.

The $> 10^7$ cm^2/Vs mobilities that can be obtained nowadays in GaAs/AlGaAs quantum wells are due to many factors [12]. One worth mentionning is the similar lattice constant of GaAs and AlGaAs (0.14% difference for maximal Al substitution) which limits lattice defects. Another is the design choice of spatially separating the electrons of the well and the charged donor ions, known as modulation doping [13], which reduces charged impurity scattering. Yet another is the cryogenic temperature required which limits electron-phonon scattering. This, and more, leads to ℓ of a several micrometers, which is large enough for mesoscopic effects to be observed.

For transport experiments to be performed in the buried 2DEG, it must be electrically contacted to the heterostructure's surface. Typically, a metal – often indium or a mixture of gold, nickel and germanium – is deposited at a specific location on the wafer and annealed. The metal diffuses through the semiconductor layers down to the 2DEG, yielding an "ohmic" contact of linear current-voltage characteristic. Using electron-beam lithography, metallic structures on the wafer's surface can further be patterned with ~ 200 nm resolution, say in a split-gate geometry as in Fig 2.2a. Applying a voltage on these gates allows local modulation of the electrostatic potential in the 2DEG, which for large enough voltages can result in bias-dependent confinement of the electrons in the second transverse direction to transport. This was first achieved nearly simultaneously by groups at Delft [14] and Cambridge [15] in the late 1980's. Such a geometry was termed a quantum point contact (QPC). In effect, it creates a conducting channel with effective length $L \sim 200$ nm and width $W < 200$ nm, putting it squarely in the mesoscopic regime for a GaAs 2DEG. For temperatures lower than the energy splitting between transverse electron energy levels, the conductance G turns out to be given by $M \cdot 2e^2/h$, as displayed in Fig. 2.2b. M is a positive integer until a large enough voltage has completely "pinched-off" the channel, ultimately driving the conductance to zero.

2.1.2 Transport in single quantum wires

The Drude-Sommerfeld conductivity is $\sigma = en\tau/m_{eff}$ (variables defined in Table 2.1) for a full conductance of $G = \sigma\frac{W}{L}$. Reducing the width of the conducting 2DEG section through electrostatic gating should therefore lead to linearly, not stepwise, decreasing conductance[2]. More problematic is that, for $L < \ell$, there is little scattering and the behaviour of σ is not well-defined. The observation of plateaus in the conductance at low temperatures as the width is reduced requires a completely different explanation.

Interpreting transport as electron transmission offers a solution to this problem, and this was first proposed by Landauer and then later refined by Büttiker [16]. Their formalism is schematically represented in Fig. 2.3, and its general result is an expression for the current in a conductor as a function of the electron distributions in its contacts

$$I_{DS} = \frac{2e}{h}\sum_{m}^{M}\int_{-\infty}^{\infty}\Gamma_m(E)\left[f_F^S(E,m) - f_F^D(E,m)\right]dE, \tag{2.1}$$

where f_F^S and f_F^D are respectively the Fermi functions of the source (S) and drain (D) reservoirs between which a current I_{DS} and voltage V_{DS} are hosted. Here, m runs over all M channels participating in the transport, each of which hosting two 1D *subband* with electron states of energies $E = \epsilon_i + \frac{\hbar^2 k_x^2}{2m_{eff}}$ (with ϵ_i the fixed transverse energy and k_x the Bloch states' wavevectors along the channel). The factor of 2 is due to the two-fold spin degeneracy which effectively dedoubles every 1D subband when there is no magnetic field. Finally, $\Gamma_m(E)$ is an energy and channel-dependent transmission that captures the effects due to scattering[3].

In its simplest form at zero temperature and with energy-independent classical trans-

[2] In fact, this is what is obtained at temperatures higher than the energy spacing between transverse energy levels, where the Fermi functions are broadened over the level separation.

[3] For this result, source-to-drain transmission symmetry is also assumed; otherwise, the left and right moving currents must be computed separately.

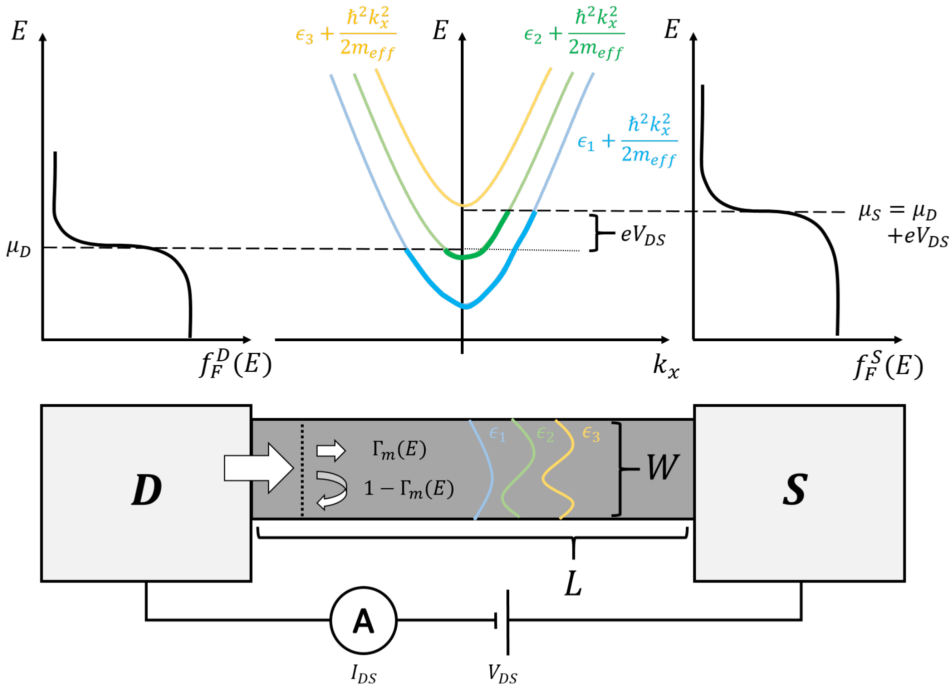

Figure 2.3: Schematic (top) and pictorial (bottom) representations of the Landauer-Büttiker formalism. A channel (dark gray) is contacted by leads (light gray) characterized by local Fermi distributions that are in equilibrium with left movers for the drain D or right movers for the source S. Each orthogonal mode m in the channel (different colours) contributes a 1D subband along the wire with populated states contributing to transport (bolded). The current I_{DS} arises from these net movers in the conductor which depend on the applied energy bias eV_{DS} and mode and energy-dependent transmissions $\Gamma_m(\epsilon)$.

mission[4], $I_{DS} = \frac{e^2}{h} V_{DS} \sum_m^M \Gamma(L)$ with $\Gamma(L) = \frac{\ell}{L+\ell}$. This result allows the ballistic $L << \ell$ (quantized conductance) regime to be recovered, since in this case $\Gamma(L) \to 1$, yielding $G \equiv \frac{I_{DS}}{V_{DS}} = M \cdot \frac{2e^2}{h}$ in GaAs QPCs. It also recovers the classical diffusive $L >> \ell$ (Drude) limit with $G = \sigma \frac{W}{L}$, since W scales with M and $\Gamma(L) \to \ell/L$, reintroducing the effect of $\ell \propto \tau$ in the equation. In-between, that is for $L \sim \ell$, $G = M\Gamma\frac{2e^2}{h}$ and plateaus may be observed, albeit not necessarily at $2e^2/h$ spacing due to $0 < \Gamma < 1$.

At this point, an important interjection must be made. Critically, both the Drude-Sommerfeld and Landauer-Büttiker formalisms have relied on the assumption of independent charge carriers to explain electron transport in 1D channels. But as stated early on, Fermi liquid theory breaks down in 1D, since there is no energy window for which the quasiparticle lifetime diverges [17]. Interestingly, there exists a solution for interacting one-dimensional electrons which is analytically exact : the Luttinger liquid model.

[4] *i.e.* we assume that the electron phase is randomized on a length $\ell_\phi << \ell$; the intermediate regime where scattering occurs but coherent electron physics are observed is more difficult to model.

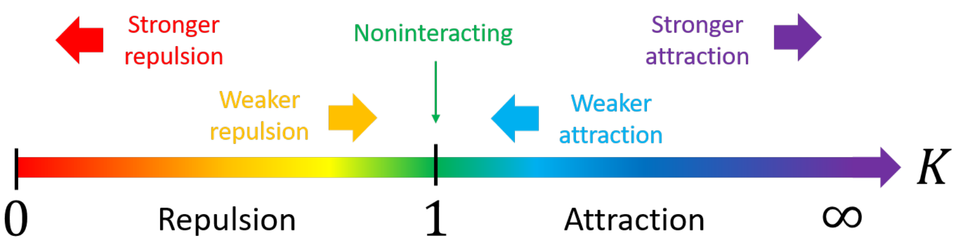

Figure 2.4: Physical meaning of the Luttinger interaction parameter K as defined in Eq. 2.2. $K = 1$ for a non-interacting electron gas, $0 < K < 1$ for repulsive interactions and $K > 1$ for attractive interactions. The magnitude of K is directly related to the strength of the interaction.

2.2 The Luttinger liquid

If only states near the Fermi energy are considered (so that two independent "branches" of linear-dispersion right and left movers can be used as a basis), the generic 1D fermion liquid Hamiltonian can be "bosonized" and its various parameters more simply rewritten as [17]

$$H = \frac{\hbar}{2\pi} \sum_{i=\sigma,\rho} \int dx \left[u_i K_i \left(\pi \Pi_i(x)\right)^2 + \frac{u_i}{K_i} \left(\nabla \phi_i(x)\right)^2 \right]. \tag{2.2}$$

This Hamiltonian is remarkable in that it is an exact description to a macroscopic number of mutually interacting particles. Its low-lying excitations, in contrast with those of the Fermi liquid, are collective and correspond to independent density waves of spin ($i = \sigma$) and charge ($i = \rho$). They are described by the bosonically-commuting fields $\phi_i(x)$ and $\Pi_i(x)$, a labeling field related to the density and its canonical momentum conjugate. The Luttinger liquid parameters u_i and K_i ultimately depend on the matrix elements for intrabranch or interbranch scattering. The first captures the density wave velocity which need not be equal for the spin and charge density waves, leading to "spin-charge separation". The second captures the strength and orientation of inter-particle interactions as explained in Fig. 2.4. The enhanced effect of interactions in Luttinger liquids leads to power-law correlation functions, greatly contrasting to the decaying exponentials of 2D and 3D free fermions.

A related bosonization formalism was first proposed by Tomonaga [18] in 1950. It was then generalized by Luttinger [19] in 1963 with corrections from Mattis and Lieb shortly after [20]. In the 1980's, Haldane accounted for interactions to formalize the idea into today's *Tomonaga-Luttinger liquid*, or more simply *Luttinger liquid* [21]. Many systems are believed to host Luttinger liquids, notably quantum Hall edges, nanotubes and nanowires, striped "quasi-1D" organic materials, and long split-gate quantum wires, as described in Sec. 2.1.1. However, experimental evidences of Luttinger liquids, especially in transport experiments, are rare due to the the difficulty of isolating a 1D system from surrounding non-1D environment.

2.2.1 The source-drain problem

The conductance of a doubly spin-degenerate Luttinger liquid can be calculated directly from the Hamiltonian in Eq. 2.2 [22] and is given by

$$G = \frac{2e^2}{h} \cdot K_\rho. \tag{2.3}$$

Hence, the lowest subband conductance of an electronic Luttinger liquid with $0 < K_\rho < 1$ should be lower than the Landauer-Büttiker value even for $\Gamma = 1$. As shown in Fig. 2.1b, this is not observed for quantum point contacts, which one could argue is due to their "point" length, whereas Eq. 2.3 is derived for an infinite Luttinger liquid. Yet, the 1D conductances of longer systems such as high-mobility micrometer-long quantum wires in GaAs [23] or mm-long single-wall carbon nanotubes [24] have also been found consistent with Landauer-Büttiker when accounting for finite ℓ.

The physical reason for this is still debated. One can see transport experiments in contacted 1D systems as a measurement of two semi-infinite $K_\rho = 1$ Luttinger liquids (the effectively noninteracting contacts) in series with a finite $K_\rho < 1$ Luttinger liquid. A careful calculation of the low-frequency G in this configuration is believed by some to make the results of such experiments indistinguishable from what is predicted by Landauer-Büttiker [25, 26]. Alternatively, others have argued that the total electric field is renormalized in a one-dimensional conductor, so while the current at constant bias is indeed modified as per the calculations of [27, 28] to yield Eq. 2.3 without further correction, Eq. 2.1 is recovered for DC conductance when accounting for the change in total field [29]. In any case, more involved experiments need to be designed to obtain evidence of Luttinger liquids.

2.2.2 Previous experimental signatures

A direct probe of Luttinger liquid physics in single-wall carbon nanotubes can be obtained via angle-resolved photoemission spectroscopy [30]. Tunneling effects in these systems have also been found consistent with Luttinger liquid theory [31]; tunneling experiments were also the first to give unambiguous credence to the presence of Luttinger liquid in GaAs/AlGaAs quantum wire systems.

In a tunneling experiment, electrons are removed from a system and introduced in another. The energy of the tunneling electron-hole pair is determined by an applied bias voltage between the two systems, and its total momentum is set by a perpendicular magnetic field. The resulting current is proportional to the number of accessible states at the relevant momentum and energies, allowing reconstruction of the spectrum of excitations. In the past, tunneling between bulk systems and/or 2DEGs was found in agreement with Fermi liquid theory [32].

Yacoby's group performed such tunneling experiments between cleaved-edge overgrown quantum wires in GaAs [33] which showed striking differences to these non-1D results, notably an anomalous zero-bias peak [34], and the effects of spin-charge separation [35] and charge partitionning [36]. Tunneling between arrays of 1D wires in GaAs and a 2DEG in GaAs was also studied by the Ritchie group to similar conclusions [37], and perhaps even reached the still-debated nonlinear Luttinger liquid regime [38]. These results suggest that coupling two quantum wires via their 1D section can circumvent the source-drain problem by being a sensitive probe to the physics happening within the 1D sections and not the noninteracting contacts.

2.3 Coulomb drag

Coulomb drag represents the orthogonal geometry to tunneling : a current is driven along a system (the *drive* layer or wire), which causes charge accumulation along a closely-spaced second conductor left floating (the *drag* layer or wire) purely due to "frictional" forces [2]. It is characterized by a *drag resistance*

$$R_D = -\frac{V_{drag}}{I_{drive}}, \tag{2.4}$$

where V_{drag} is the voltage developed in the drag layer and I_{drive} is the current imposed in the drive layer. The negative sign is present to ensure that R_D is positive in typical circumstances. Coulomb drag is also an equilibrium phenomenon, as opposed to other "ratchet" effects which are nonlinear in nature.

Many competing models exist to theoretically describe R_D. Importantly, different behaviour as a function of various system parameters (intersystem separation, systems' densities, temperature, material parameters such as effective Bohr radius, etc.) are expected for the free particles of Fermi liquids and strongly-correlated excitations of Luttinger liquids, since Coulomb

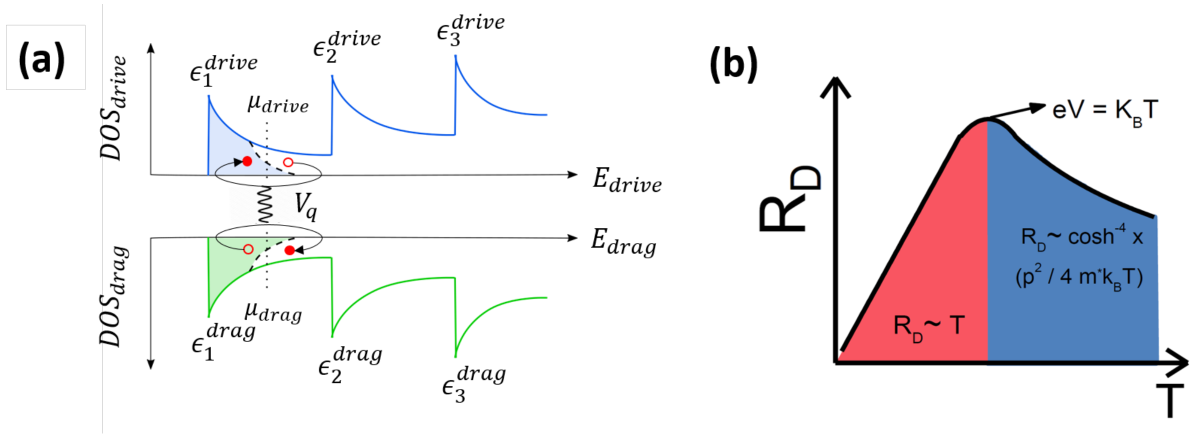

Figure 2.5: (a) Schematic representation of the drag mechanism between Fermi liquids. Coulomb scattering mediates momentum transfer from the (driven out-of-equilibrium) drive layer to the (passive) drag layer. Shown are the multichannel 1D density of states (DOS) in each wire as a function of energy (ϵ_i^{label} being the subband energies in each wires). Shaded areas are the occupied states from Fermi statistics at finite temperature. Momentum is related to energy via the free electron dispersion $E = \hbar^2 k^2 / 2m_{eff}$, keeping in mind that the bias in the drive wire breaks the $\pm k$ symmetry. (b) Prediction of R_D between 1D Fermi liquids. Figure from [3] using results of [41].

drag ultimately depends on the nature of interactions [39, 40].

2.3.1 Theoretical studies of Coulomb drag

For Fermi liquids, the mechanism for frictional drag is interlayer momentum transfer. As such, the signal is theorized to decay with decreasing temperature as the availability of electron-hole pairs about the Fermi levels for this sort of process diminishes. In 2D, this dependence can be calculated to be quadratic [42, 43] with logarithmic corrections [44]. If the same assumptions are made in 1D, a linearly-decaying drag resistance is rather expected for identical wires below a characteristic temperature $k_B T \sim eV_{drive}$ [41]. Above this temperature, the behaviour is reversed, and the drag starts decreasing with increasing temperature [45]. This is schematically represented in Fig. 2.5. For wires with differing electronic density, the full calculation reveals that the drag should exponentially be suppressed with density mismatch at low temperature.

For infinite Luttinger liquids with identical density, a renormalization group analysis can be performed to account for the strongly-correlated nature of the system [46]. In this picture, at low enough temperatures where backscattering dominates, the charge density waves of the systems are expected to “lock” and in response, the drag signal should diverge exponentially with $T \to 0$. Above a crossover temperature T^* also setting the scale for the exponential divergence,

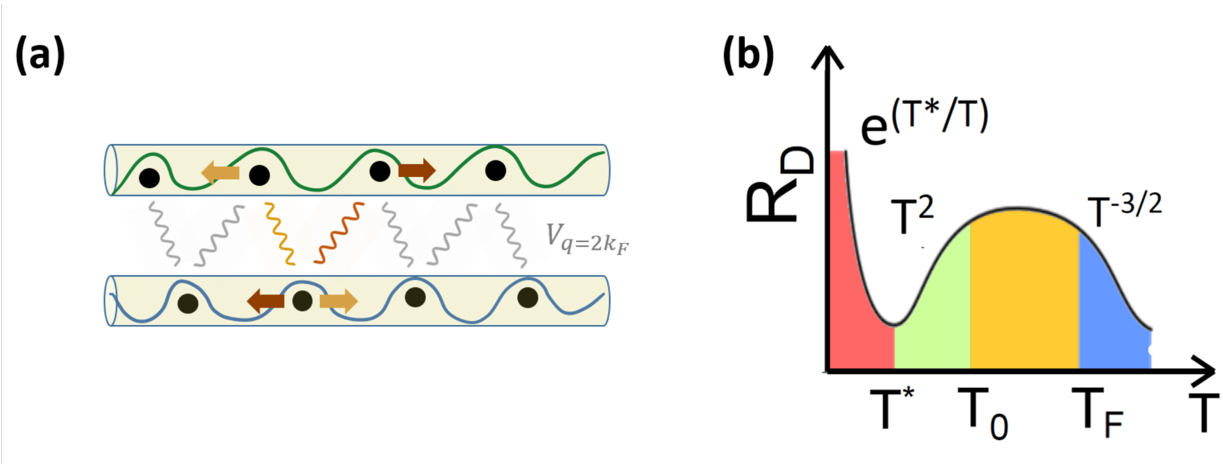

Figure 2.6: (a) Schematic representation of the low-temperature drag mechanism between Luttinger liquids. For small energies, $2k_F$ momentum transfer (backscattering) is dominant and the charge density waves of the two wires (blue, green waves) become "interlocked" in a zigzag pattern. Activated "slippage" of one density wave with respect to the other is possible, leading to an exponential dependence of the drag resistance on temperature. (b) Coulomb drag prediction between Luttinger liquids including higher temperature forward-momentum contributions. Figure from [3] using results of [46, 47].

$$T^* \sim T_F e^{-\frac{k_F d}{1-K_\rho^-}}, \tag{2.5}$$

with K_ρ^- a net antisymmetric charge interaction parameter, and d the interwire separation, the behaviour is reversed and the drag resistance is found to increase with temperature as a power law. When nonlinearities in the dispersion relation are considered[5], this last effect can be increased by the addition of forward scattering contributions [47, 52–55], leading to further non-monotonicity at higher temperatures. This is illustrated in Fig. 2.6. If the wires differ in electronic density, an exponential suppression of backscattering in the density mismatch at low temperature is expected to lead to a corresponding decrease in R_D by leaving only forward scattering [56]. Finally, spin-charge coupling effects may also modify the drag [46, 57].

For physical systems, finite-sized effects may also come into play. The calculation of [46] predicts a low temperature divergence saturating at some finite, exponentially large value in the wire length L. Should the effective wire overlap area fall below $L^* \sim \hbar v_F/T^*$, the charge density wave locking may be suppressed and the exponential increase of R_D in lowered temperature vanish. Furthermore, if the system extent is on the order of its characteristic voltage length $L_V \equiv \hbar v_F/eV$ and thermal length $L_T \equiv \hbar v_F/k_BT$, charge and energy fluctuations

[5] Subtleties concerning slower intrawire equilibration as compared to interwire momentum transfer previously need to be addressed, since three-body relaxation processes involving particles at the bottom of the band are required for inelastic scattering in 1D systems [48–51].

may become significant and play a role in the drag signal, the details of which would depend on the microscopic details of the environment [58–62]. These are predicted to lead to a breakdown of the Onsager relations, to the emergence of a negative drag signal for significant electron-hole asymmetry, and to local maxima in the drag signal as subbands are being populated.

2.3.2 Experimental studies of Coulomb drag

As for tunneling, early (2D-2D) Coulomb drag experiments between 2DEGs in GaAs/AlGaAs were consistent with Fermi liquid theory in 2D [42, 63]. The first such experiments in 1D were performed between quantum wires defined in the same 2DEG and separated by an electrostatic barrier. A 2001 experiment by Debray *et al.* reported increasing R_D with reduced T for single subband occupancy, as well as peaks in R_D as the wires' gate voltages were swept [64]. A 2006 experiment by Yamamoto *et al.* observed even further deviation from Fermi liquid behaviour with the display of a regime of *negative* R_D at low electronic density, although this was attributed to Wigner crystallization [65].

As outlined in Eq. 2.5, the proper figure-of-merit for Luttinger liquid charge density wave-locking is $k_F d$. In laterally-coupled geometries, d will necessarily be large, and at least of order of the 2DEG depth due to shadowing [66], typically $\gtrsim 80$nm. For temperatures above 100 mK, phonon drag should have a non-negligible impact on the drag if $k_F d > 5$ [67]. The Debray *et al.* experiment was reported to have been carried out with a $k_F d$ parameter ~ 3, and the Yamamoto *et al.* experiment with $6 \lesssim 2k_F d \lesssim 13$. This casted doubts on the nature of the drag effect observed in these two experiments. As will be explained in the next sections, the vertically-coupled quantum wires design of Laroche *et al.* overcame this issue and provided clear manifestations of Luttinger liquids in electronic systems.

2.3.3 Vertically-integrated quantum wires

A platform was developed by Laroche *et al.* that allows $k_F d \sim 2.2$ coupling between independently-contacted split-gate quantum wires [4]. This was achieved with the Epoxy-Bond-and-Stop-Etch (EBASE) technique [68] summarized in Fig 2.7. The device geometry is etched in a GaAs/AlGaAs double quantum well heterostructure, which is similar in spirit to Fig. 2.1, but with two GaAs regions surrounded by AlGaAs and dopants. Gates and ohmic contacts are then defined. A new substrate is bonded over the wafer, and the material is flipped. The original substrate is subsequently mechanically lapped and then etched. New gates are deposited on

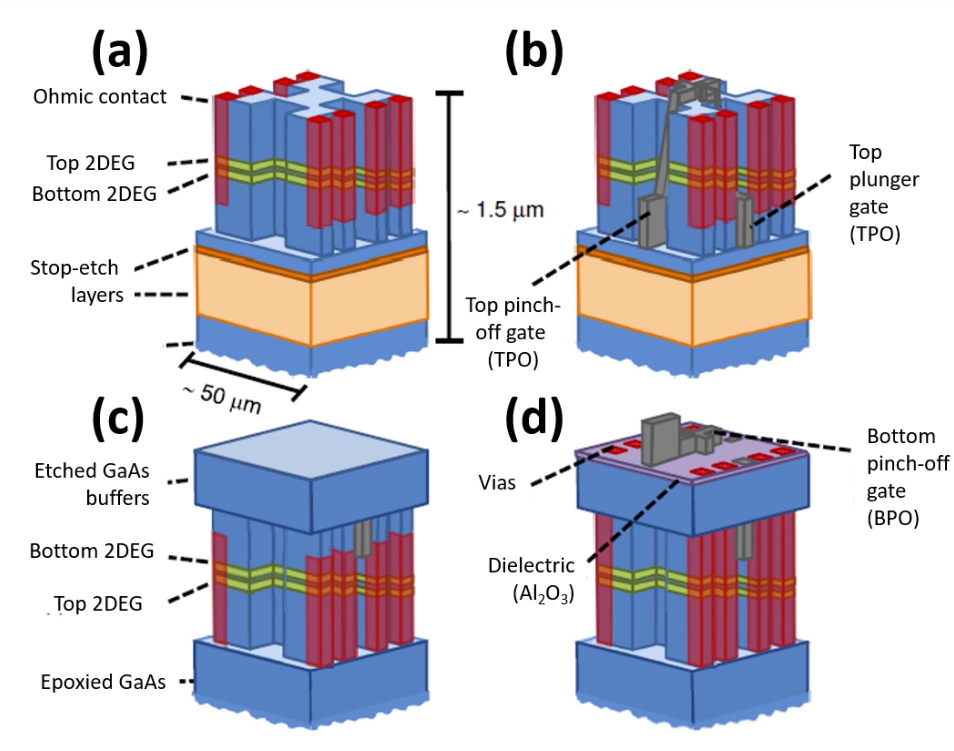

Figure 2.7: Schematics of the fabrication highlighting the EBASE process. (a-b) The surface of a double quantum well heterostructure is processed. (c) A new GaAs substrate is epoxied to the top of the original wafer, and the assembly is rotated to lap and etch the original substrate. (d) Processing is performed on the lower side of the wafer to define new gates and connect the previously-defined gates and contacts. Figure adapted from [4].

the thinned bottom of the wafer after a dielectric material deposition, and vias are then etched to electrically contact the original gates and ohmics. Complete fabrication details can be found in Ref. [3].

The resulting separation between the two wells' wavefunction peaks is then bounded between 33 nm to 41 nm when accounting for the AlGaAs barrier thickness and horizontal misalignment.The replacement of the large depletion region of the previous experiments by an atomically-defined hard barrier allows stronger coupling while also more efficiently suppressing tunneling between the two electronic layers. In these devices, the ohmic contacts diffuse to connect both the top and bottom quantum wells. Independent contacting is achieved through the geometry of the heterostructure and the split gates. Two large *pinch-off* gates, denoted TPO for the pinch-off gate of the top well and BPO for the pinch-off gate of the bottom well are set to a voltage large enough to deplete the well closest. This effectively inhibits conduction between opposite ohmic contacts when both PO gates are activated as illustrated in Fig. 2.8. Smaller *plunger* gates, denoted TPL for the plunger gate of the top wire and BPL for the plunger gate of the bottom wire, complete the split gate structure with a smaller footprint.

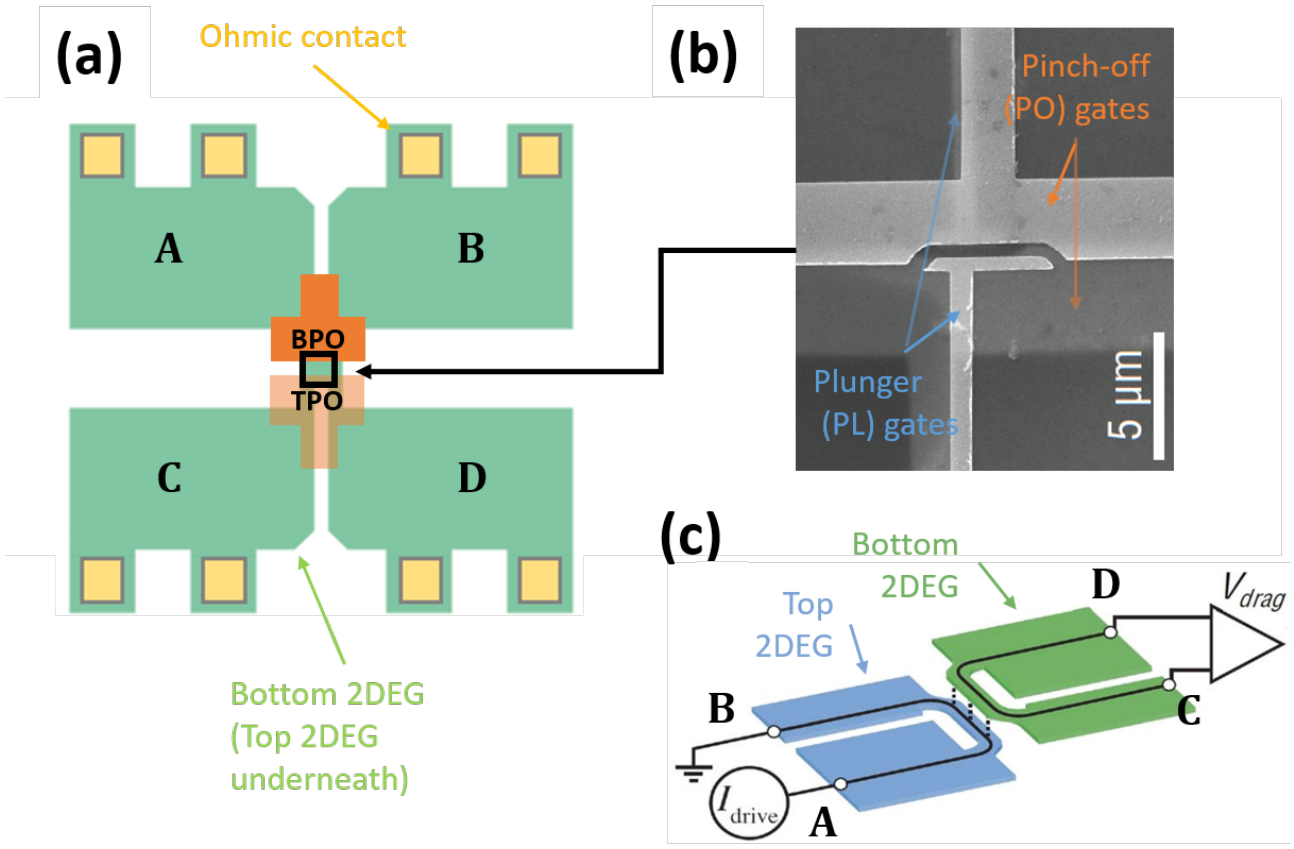

Figure 2.8: (a) Top-down schematic representation of device geometry displaying relative positions of 2DEG, ohmic contacts, pinch-off gates and gated area. From an above view of the device chip, BPO would appear at the surface, whereas TPO would appear underneath. The geometry is such that there are four distinct contacting area A, B, C, and D about the wires to be formed. (b) SEM of the gated area containing the vertically-integrated quantum wires with surface-bound bottom (solid) and underlying top (transparent) pinch-off and plunger gates apparent. (c) Schematic of the device with gates activated (not displaying disconnected 2DEG sections) and Coulomb drag geometry. Figures adapted from [5].

Coulomb drag between independent split-gate quantum wires can then be performed in this design. Fig. 2.8b shows a scanning electron microscope image of the active area of the device showing wires' alignment, and Fig. 2.8c shows a schematic of the device with gates activated together with the Coulomb drag measurement scheme.

2.3.4 Previous results

In such devices, Coulomb drag has been studied by Laroche *et al.* at different subband occupancies of the two wires by adjusting the voltage on one of the plunger gates [4]. The other wire is close enough as to have its own subband occupancy shifted as well. During this measurement, the other three gates are set as to make the wires similar in terms of subband

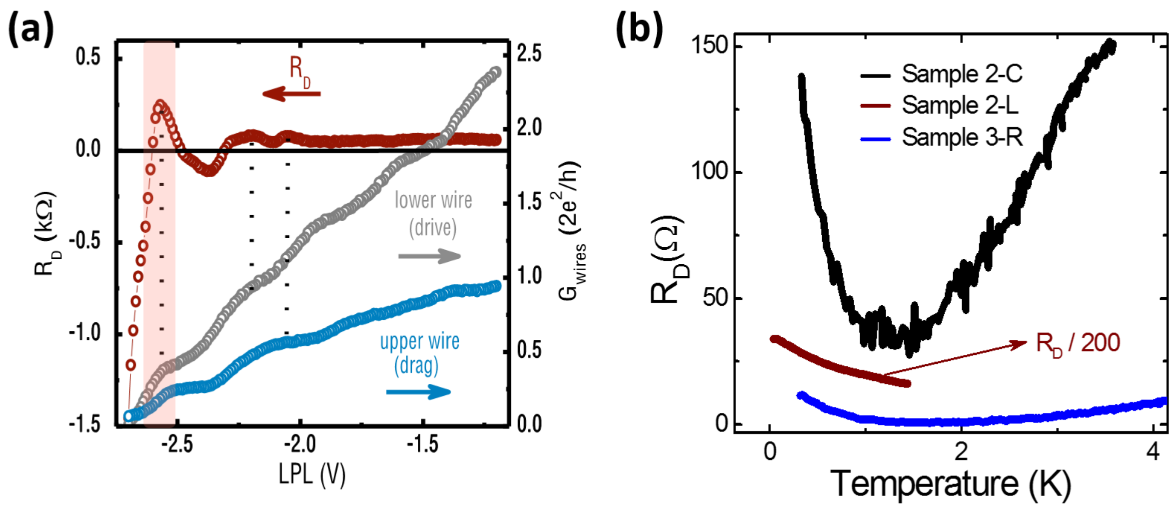

Figure 2.9: Key results of previous Coulomb drag experiments in vertically-integrated quantum wires. (a) Quantum wires with visible diffusive plateaus (blue, gray) of similar subband occupancy and associated peaks in R_D (red) concomitant with subband populating. The positive 1D-1D peak of interest for temperature dependence experiments is shaded. (b) Non-monotonic upturn in the temperature dependence of the 1D-1D R_D as a signature of the Luttinger liquid state. Figures from [5].

occupancy, as shown in Fig. 2.9a. The wires are observed to be non-ballistic but also display plateaus indicative of well-developed 1D subbands. The drag resistance displays peaks when 1D subbands are opened, and is negative at low densities near full depletion of the wires. It is also negative in a region between two peaks when the subband occupancy is greater than one.

The temperature dependence of R_D in these devices provided strong evidence for the presence of Luttinger liquid physics [5]. When a single subband is occupied in each wire, the drag resistance displays an "upturn", which as explained in Sec. 2.3.1 appears in Luttinger liquid formulations of drag but not Fermi liquids'. As presented in Fig. 2.9b, this was observed in multiple devices. This feature is not present when any subband occupancy is tuned above one. From the position of the minimum and an estimate of wires' electronic density, an estimate of $0.06 \lesssim K_\rho \lesssim 0.18$ across all samples can be obtained from Eq. 2.5, which would place the systems in a strongly-interacting regime. This motivates more extensive study of Coulomb drag between quantum wires. This is the main thrust of subsequent chapters.

Chapter 3

Methodology

Coulomb drag experiments between quantum wires were performed in the vertically-integrated configuration described in Sec. 2.3.3. In this thesis, the results from two different devices defined on two different chips, Device A and Device B, are presented. Appendix A contains previously-measured parameters of the two devices' wafers, and the differences between the two devices will be further elaborated upon in the next chapters. This chapter presents the common methodology that was used to perform experiments in both devices. The experiments are performed in a similar manner as in [3]. Various measurements are carried out to characterize the devices and measure Coulomb drag. All these manipulations, however, are performed at low temperatures to ensure that the limits described in Sec. 2.1 are reached, and the experimental conditions met.

3.1 Apparatus

3.1.1 Refrigeration

Dilution refrigerators were used to sustain the ≈ 20 mK temperatures used for these experiments. Device A was characterized over multiple cooldowns in a wet dilution refrigerator from the Microkelvin Facility with the sample bathing in liquid ^{3}He contained inside a polycarbonate cell [69]. Device B was measured in two subsequent occurrences, once in a wet dilution refrigerator and once in a dry dilution refrigerator, both at the McGill low-temperature facility. More information specific to the McGill wet fridge, its sample stage, and on the dilution process in general can be found in [70]. The newly-installed dry refrigerator shares the same operating principles, but replaces all non-circulation cooling technology with cryocoolers. Its sample stage is detailed in Appendix B.

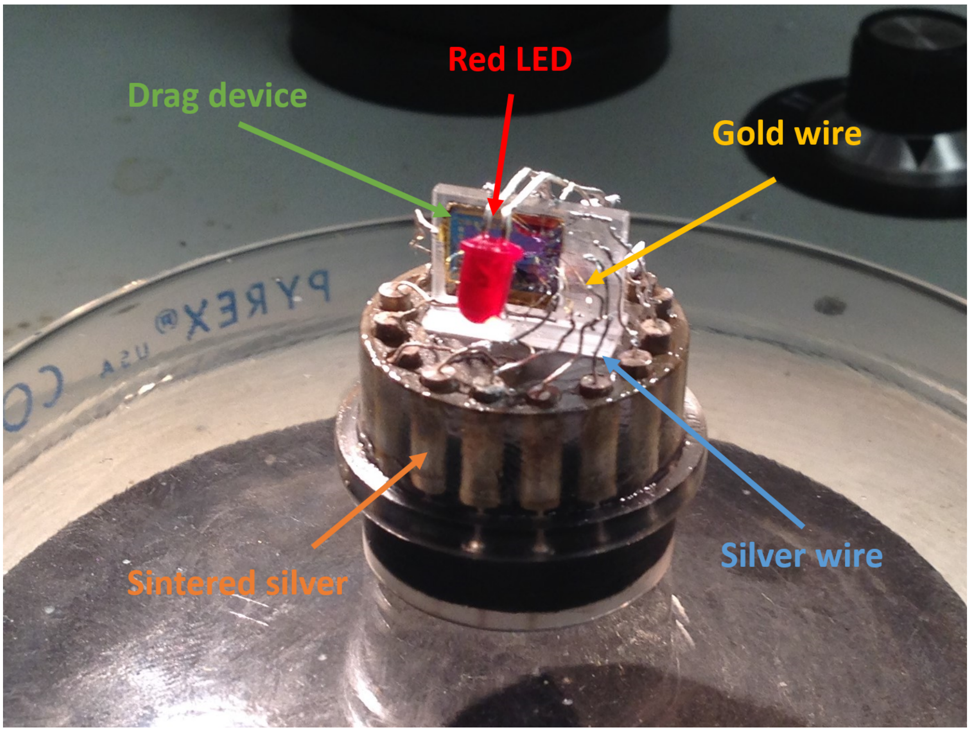

Figure 3.1: Polycarbonate cell mount used to cooldown Device A with mounted chip and red light-emitting diode. The small canisters contain silver powder; when the cell is sealed upon installation in fridge, the canisters and sample are immersed in ^{3}He thermalized to the fridge's coldest stage. Silver wires electrically connected to these canisters are indium-soldered to gold wires, who are in turn indium soldered to the gates and ohmic contacts on the sample chip.

3.1.2 Wiring

The suppression of electron-lattice scattering in ultracold high mobility 2DEGs ensures that most of the energy dissipation in the 2DEG at base temperature comes from the diffusion of thermalized electrons from the ohmic contacts where the annealed metal more efficiently couples 2DEG, substrate, and wiring. To ensure the lowest electronic temperatures are reached, then, the substrate and sample wiring must be in good thermal contact with the dilution stage (wiring from room temperature is naturally heat sunk at every cooling stage prior to reaching the dilution unit). Incoming radiative power such as electromagnetic pickup and blackbody radiation should also be minimized.

The polycarbonate cell setup of Device A achieves this by having the leads going to the sample be sintered silver immersed in ^{3}He as close as possible to the sample : the setup is presented in Fig. 3.1. For Device B, in both refrigerators the wires going to the sample are passed through silver powder in thermal contact with the mixing chamber. For both samples, RC filters are also present uphill of the sample to reduce incoming high-frequency input power. The details of the filtering for the dry fridge are presented in Appendix C. The device itself

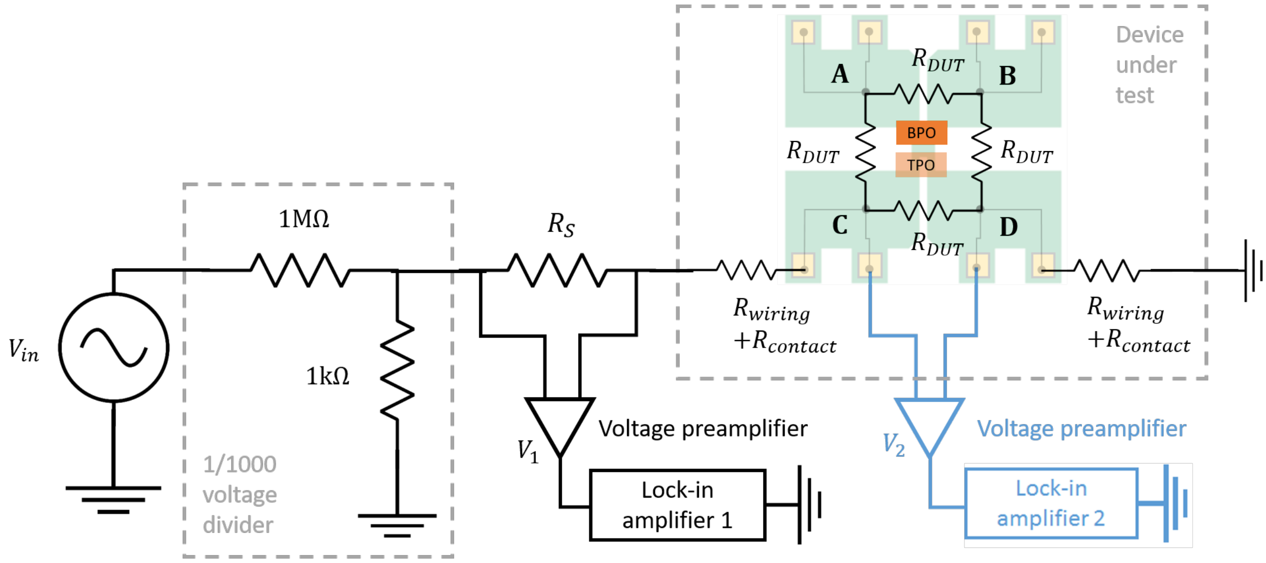

Figure 3.2: Two- (black circuit elements only) and four- (black and blue circuit elements) point conductance measurement circuits. R_{DUT} (both 2pt or 4pt) is determined by which 2DEG regions out of A, B, C or D are used and the gate voltages applied to the device (only the pinch-off gates' location with respect to the contacts is displayed). R_{2pt} is given by $R_S \cdot \left(\frac{V_{in}/1000 - V_1}{V_1}\right)$ and R_{4pt} is given by $V_2/I = R_S \cdot \frac{V_2}{V_1}$.

rests on a sample holder which fits on a header located on the sample stage. In addition, a red light-emitting diode (LED) was sometimes mounted on the sample holder alongside the device. This LED could be powered with a current source to allow illumination of the device during cooldown, permitting modification of 2DEG properties as discussed in Sec. 4.1.4. With this wiring setup, electrical contact to a drag device held at low temperature is achieved and measurements can be performed.

3.2 Measurement schemes

Three different measurements schemes are used : a two (or four) point conductance measurement to identify the quantum well depletion regions and later each quantum wire's subbands; a dI/dV measurement to measure the tunneling resistance between the two quantum wells; and the drag measurement itself. The measurements leverage typical low-frequency lock-in AC techniques to minimize noise and DC artefacts.

3.2.1 Conductance measurements

Since the power dissipated in an ohmic conductor is $P = RI^2 = V^2/R$, in the depletion situations where $R \to \infty$ constant voltage measurements are required to avoid damage by self-heating. Such a circuit is presented in Fig. 3.2. The set of resistances between the various terminals of the device under test is determined by the voltage applied on the split gates. By choosing which of the two or four terminal pads of the device under test are connected to the circuit, grounded, or left floating, it is possible to measure each layer's (or wire's) resistance or the interlayer resistance. Typical values of excitation voltages V_{in} are 50 mV, which is reduced to a lower power level by the voltage divider and measured prior to performing measurements. R_S is a "sense" resistor of independently-determined value, typically 996 Ω whose voltage drop is measured to determine the current.

In the two-point (2pt) configuration, only lock-in amplifier 1 and its (optional) preamplification chain are used to obtain the voltage V_1 about R_S. In this manner, the sum of device, wiring, and contact resistances, referred to as the 2pt resistance, can be expressed as $R_{2pt} = R_S \cdot \left(\frac{V_{in}/1000 - V_1}{V_1}\right)$. This depends on the 1/1000 voltage divider action, which is expected to hold as long as all other series resistances are well below 1 MΩ. Using the four-point (4pt) configuration avoids including the fridge wiring and contact series resistances, although in practice four working contacts are not always available to perform this measurement. In the 4pt configuration, lock-in amplifier 1 monitors the current across the entire circuit via $I = V_1/R_S$, and lock-in amplifier 2 (locked to the same frequency as the source and lock-in 1) directly measures the voltage V_2 about the semiconductor where resistance is to be measured. R_{4pt} therefore directly yields R_{DUT} as $V_2/I = R_S \cdot \frac{V_2}{V_1}$. Since both I and V are measured, this does not depend on exact voltage divider action, although it is still used to limit the power. Finally, the conductance G is more customary when discussing depletion situations where $G \to 0$ or quantized conductance, so the 2- or 4pt resistance in Ohms $R_{i\mathrm{pt}}$ is converted to conductance in natural units of $2e^2/h$ via $G_{i\mathrm{pt}} = \left(\frac{R_{i\mathrm{pt}}}{h/2e^2}\right)^{-1} \approx \left(\frac{R_{i\mathrm{pt}}}{12906}\right)^{-1}$.

3.2.2 Tunneling measurements

To ensure independent layers, the voltage on the pinch-off gates is optimized to attain a 2D-2D tunneling resistance larger than 10 MΩ (lower than 0.1 μS) about zero bias (typically, up to ± 1 mV) prior to performing drag. This corresponds to a resistance at least 10 times larger than the wires' where they are considered.

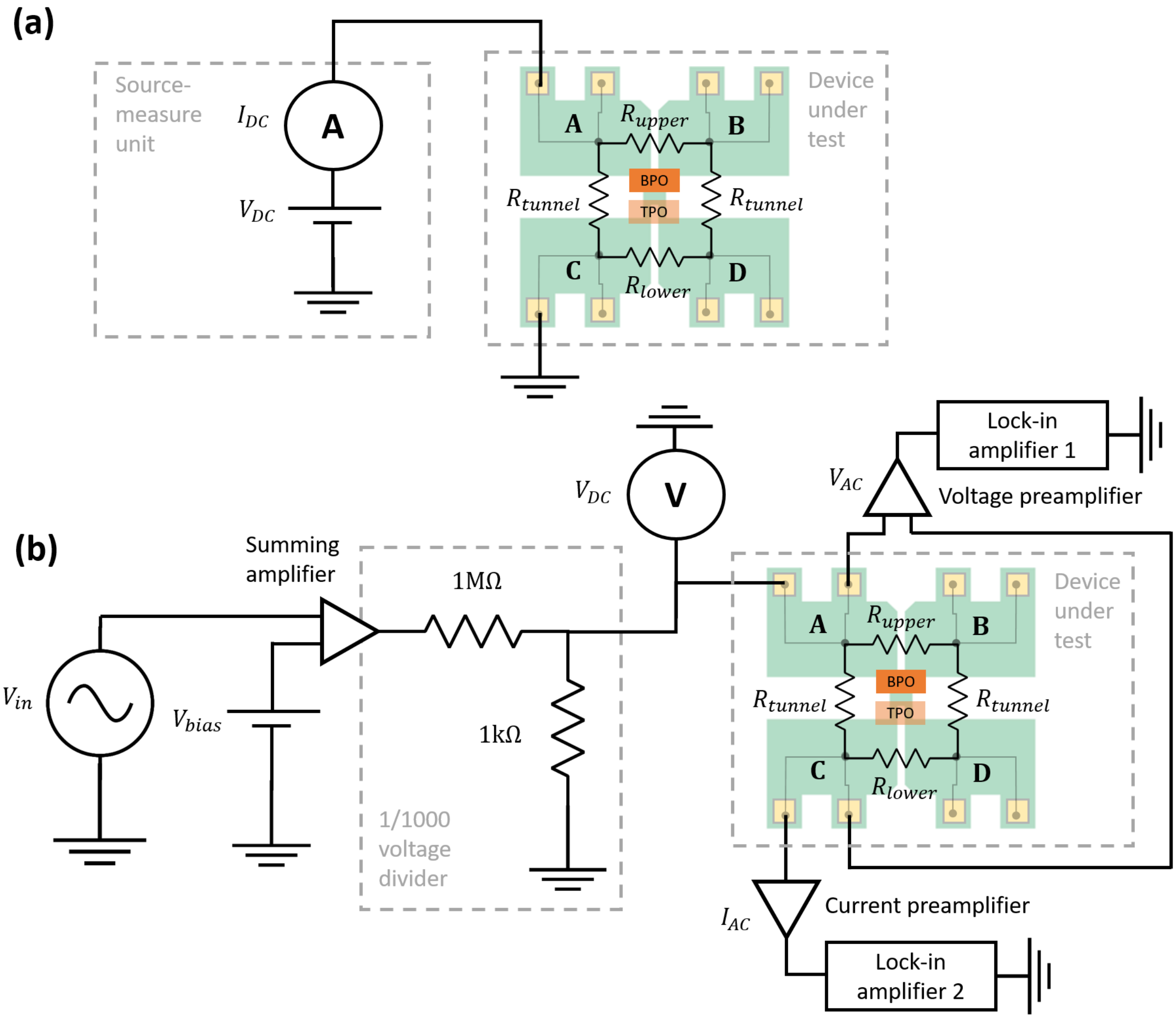

Figure 3.3: Tunneling measurement circuit between two opposite ohmic contacts on the device, where opposite means across the top pinch-off gate (TPO, closer to the deeper well after EBASE) and bottom pinch-off gate (BPO, closer to the wafer surface after EBASE). (a) A source-measure unit inputs a voltage V_{DC} directly into the device and measures the resulting current I_{DC}. The dI/dV characteristics can then be inferred from numerical differentiation of the $I_{DC}(V_{DC})$ signal, yielding $G_{tunnel} \equiv 1/R_{tunnel}$. (b) 4-pt small-signal analysis circuit. A DC bias V_{bias} superposed with an small AC signal V_{in} is input in the device. The DC tunneling bias V_{DC} is monitored at the input with a digital voltmeter. The resulting AC voltages V_{AC} and AC currents I_{AC} are used to calculate the tunneling resistance $G_{tunnel} = I_{AC}/V_{AC}$.

Two different schemes were utilized to achieve this and they are displayed in Fig 3.3. Circuit (a) was used to characterize Device A and circuit (b) to characterize Device B. This choice was only made due to availability of equipment at the time, since previous studies of these devices did not report a significant difference between the two schemes [3]. In circuit (a), the IV curve between two opposite contacts is directly measured using only a source-measure unit. The tunneling dI/dV curve is then obtained from the numerical differentiation of $V_{DC}(I_{DC})$. In

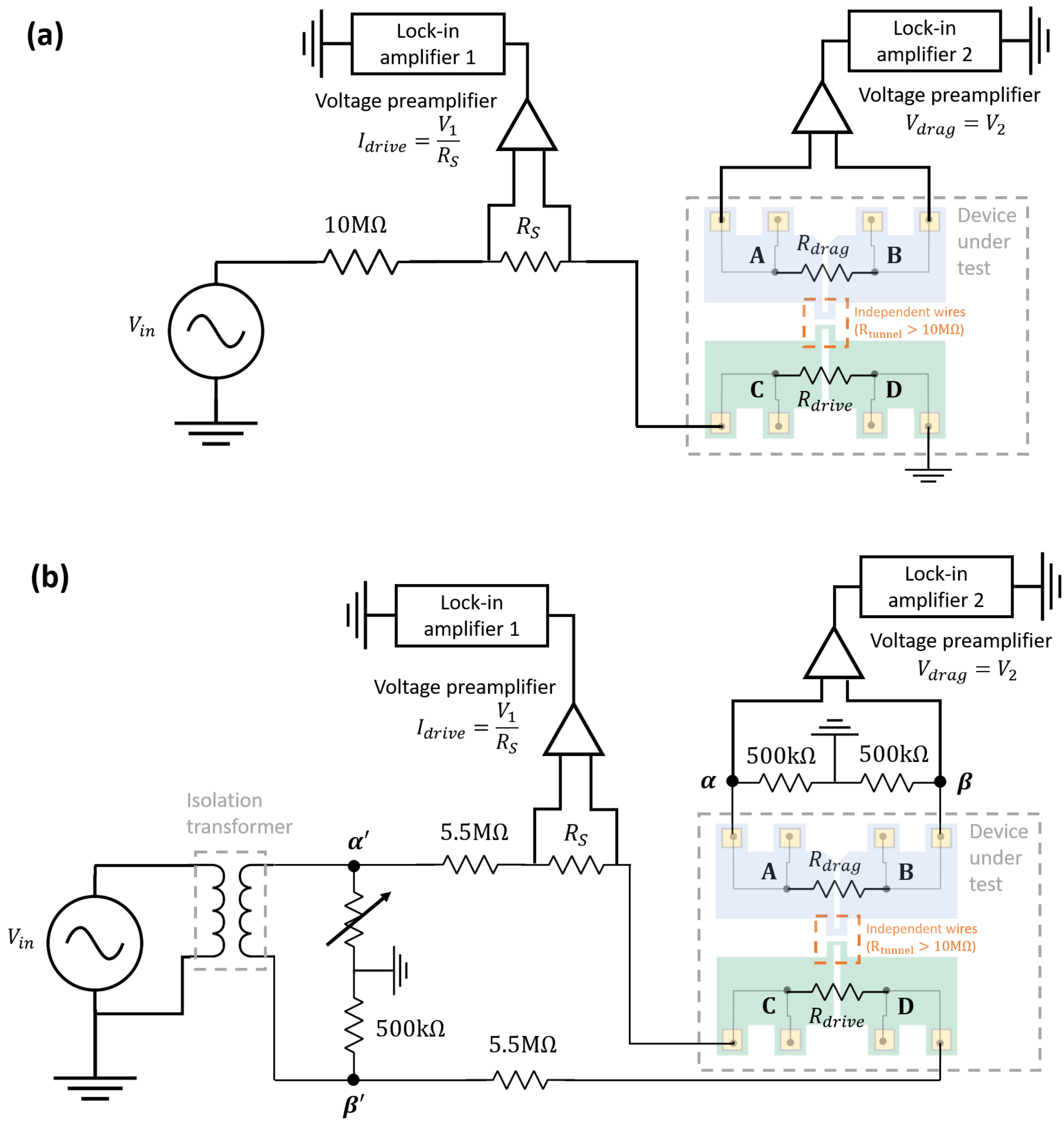

Figure 3.4: Circuits used to measure drag resistance. In both cases, the drag resistance R_D is given by $-V_{drag}/I_{drive} = -R_S \cdot \frac{V_2}{V_1}$. (a) Simple circuit used for Device A. (b) Symmetrically-grounded drag circuit used for Device B. The variable resistor in the drive branch is set so that the resistance between α and β exactly matches the resistance between α' and β' (prior to connecting to the rest of the circuit).

.

circuit (b), a small-signal analysis of the DC biased tunneling resistance is directly performed, typically using $V_{in} = 50\ \mu$V and -10 mV$< V_{DC} < 10$ mV after the voltage divider.

3.2.3 Drag measurements

Two different drag circuits were used to acquire the data presented in this thesis. These circuits were again observed to yield the same drag resistances (up to an offset of a hundreths of volts) in past experiments [3]. They are presented in Fig. 3.4.

For Device A, the simple circuit in Fig. 3.4a was used. A large resistance (10 MΩ) in series with the voltage source imposes a current $I \approx V_{in} \times 10^{-7}$ A across the drive wire, which is monitored by lock-in amplifier 1 and a sense resistor $R_S = 996\ \Omega$ as in the conductance measurement of Sec. 3.2.1. The drag voltage V_{drag} is monitored by lock-in amplifier 2. V_{in} is chosen for the drag experiment to lie in the linear regime as explained in Sec. 4.2.1.

Another circuit presented in Fig. 3.4b was also used to limit the development of biases in the floating wire by mirroring the grounding of the two layers. The data related to Device B presented in this thesis use this circuit. An isolation transformer (whose gain is characterized prior to operation) is inserted between a voltage source with similar V_{in} and two 5.5 MΩ resistors symmetrically-positioned around the drive wire. This also imposes a current $I \approx V_{in} \times 10^{-7}$ A across the drive wire, which is monitored in the same way. The drag voltage V_{drag} is measured by lock-in amplifier 2. Symmetric grounding is achieved by connecting each of the branches of the circuit to a ground via 500 kΩ resistances, with the variable one in the drive branch tuned to match the resistance of the circuit in the drag branch for best mirroring.

3.3 Experimental workflow

In this thesis, the Coulomb drag resistance is only studied as a function of similar wires' subband occupancies when a single plunger gate is swept in voltage. To reach a regime where this can be done, the devices are manipulated in sensibly the same manner. Prior to performing drag, the electron bilayer and individual wires are characterized with conductance and tunneling measurements at different gate voltages. The objective is to obtain two independent wires that can be contacted individually and wires with similar pinch-off voltages as a function of one of the plunger gates. The drag resistance is then measured as a function of this plunger gate. When possible, various checks are also performed on the resistance derived from drag measurement to ensure that what is measured is indeed Coulomb drag. These checks include linearity of the drag voltage with current, independence of the drag resistance on probe orientation, independence of the drag resistance on drive and drag wire reversal, and frequency independence of the drag resistance. Subsequently, the drag resistance may be analyzed.

The procedure is best detailed with supporting data. In the next chapter, it will be applied to Device A with more thorough explanations along the way. The subsequent chapter will repeat the process for Device B with fewer explanations. Each of these chapters will also contain the relevant details and analysis of the device considered.

Chapter 4

Device A : high-mobility heterostructure

Device A was fabricated in a semiconductor wafer provided by the Princeton collaboration (Pfeiffer and West) with wires of lithographic length 4.2 μm. The novelty of Device A is that it is defined in a heterostructure whose unpatterned mobility is a factor of 5 larger than the typically-used heterostructures as reported by Laroche *et al.* (see Appendix A).

A characteristic inherent to Device A is an exponentially increasing leakage current with TPL voltage (up to 100 nA for $V_{TPL} = -2$ V), as displayed in Fig. 4.1. This current was mirrored in TPO, hinting a leak that was developing between the gates and not a gate and the 2DEG. Nonetheless, this leakage was limited to 100 nA for precaution, which constrained the available range of gate voltages. This, combined with the greatly different layer conductances in the device as-is, meant that optimizing cooldown conditions became necessary to have the lowest-lying subbands of each wires accessible simultaneously. Another specificity of the drag measured in Device A is the temporal and electrostatic environment dependence of the signal. Drift was present, meaning that a Coulomb drag sweep taken at some time could differ quantitatively, or even qualitatively, from the sweep performed at the same gate voltages a few hours later or after the device had been grounded even without connecting or disconnecting wires. To alleviate this issue, mappings of the wire conductance and drag as a function of multiple TPL voltages were performed regularly so that, when such a drift occured, the “effective” wire configuration from the observed drag could be retrofitted.

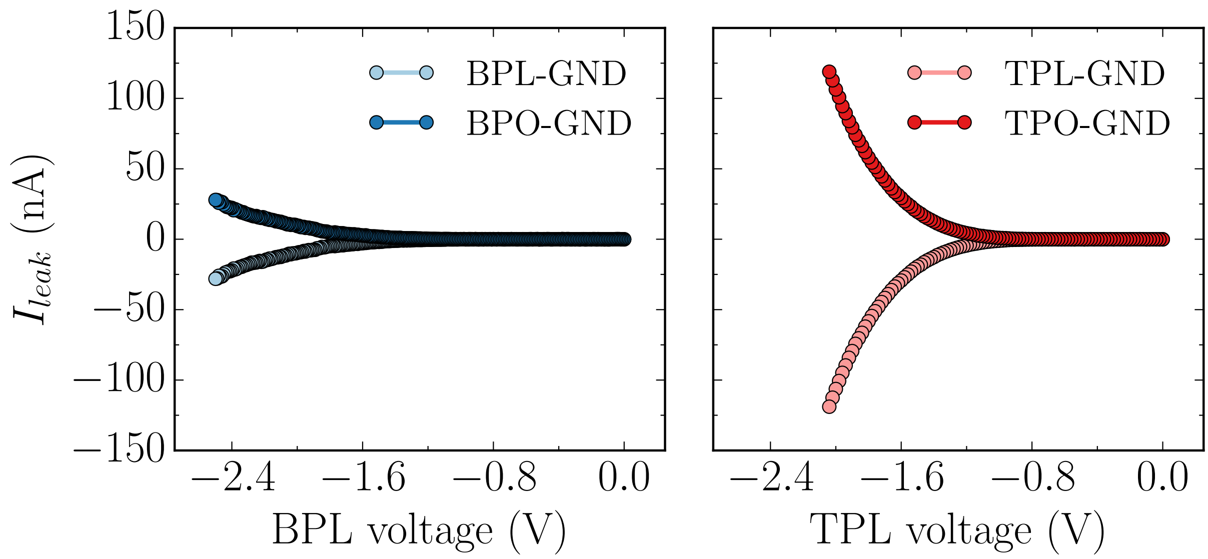

Figure 4.1: Leakage current between gates and ground as one plunger gate is swept while the other plunger remains grounded, and for POs held at their highest tunneling-suppressing value. The complementary behaviour of the gate pairs indicates that leakage occurs principally between the gate pairs and not to the 2DEG. Note that the top gates have a more pronounced leakage than the bottom gates.

.

4.1 Preliminary device characterization

4.1.1 Pinch-off gate sweeps

After establishing that enough ohmic contacts can be used and that all gates are contacted to the device, the first test performed on a new device is a conductance measurement with a set of working ohmic contacts between which there is a pinch-off gate. For each of the two pinch-off gates, two geometries are available : from top to bottom (for instance, A-D) or left to right (A-B or C-D); refer to Figs. 3.2 for relative positions of swept gates and contacts. A conductance measurement is setup between the two contacts, and a gate (either BPO or TPO) is ramped down in voltage, typically at a rate of about −0.005 V/s. All sweeps begin on a plateau corresponding to the conductance in parallel of the two quantum wells. As voltage is ramped down below a critical voltage, the layer nearest the swept gate gets depleted and the conductance falls to a lower plateau corresponding to the conductance of only the furthest layer. This is maintained until this second layer also becomes depleted and the conductance falls to zero. The measurement is then performed with the gate voltage swept in the reverse direction to check for hysteresis of the gate.

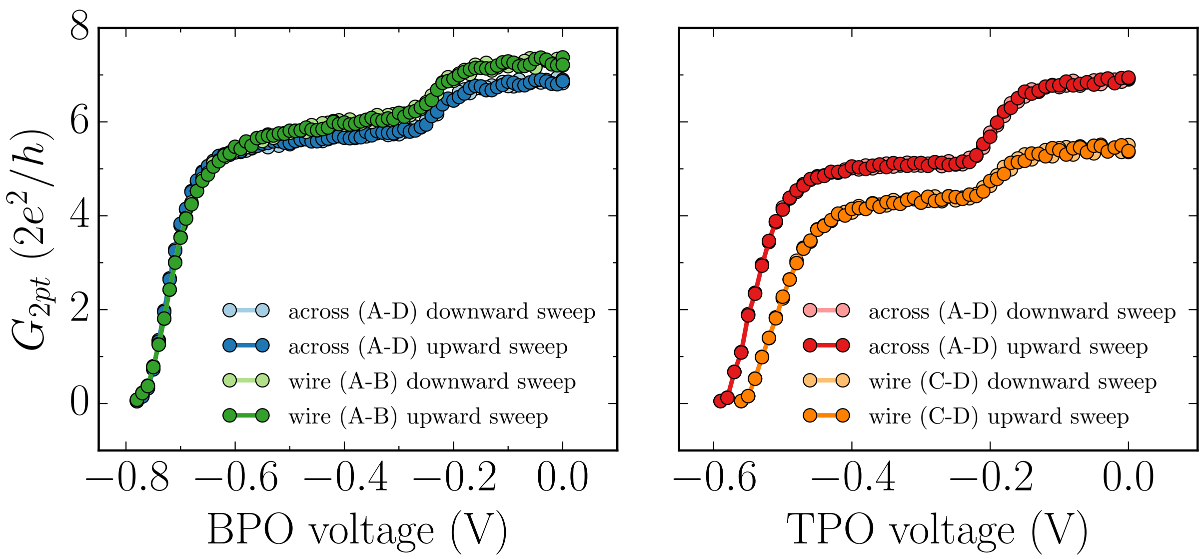

Figure 4.2: Pinch-off curves for Device A with biased plunger gates, but no illumination, during cooldown. Left : BPO gating for configurations where it should cut conduction. Right : TPO gating for configurations where it should cut conduction. The existence of the two quantum wells can be inferred from the presence of two plateaus in each sweep.

Such measurements are presented in Fig. 4.2 for Device A. The upward and downward curves are the same for the selected sweep rate, meaning that the pinch-off gates are not significantly hysteretic. Two plateaus are also clearly observed in all configurations, meaning that two electron layers are present and hence it is possible to set the gate voltages so that no conduction occurs between opposite contacts. To firmly establish this, the gate voltages are optimized using tunneling measurements.

4.1.2 Pinch-off gate optimization

As discussed in Sec. 2.2.2, when a bias exists between two closely-spaced systems, electron tunnelling between the two is enhanced. This could contribute to the measured drag voltage, and as such cast doubt on its measurement. Therefore, the optimal voltage for the pinch-off gates must be determined by way of tunneling measurements, as explained in Sec. 3.2.2.

Fig. 4.3 presents the tunneling data for Device A. The tunneling experiment is repeated for various TPO and BPO voltages until a suitable $\gtrsim 10$ MΩ tunneling resistance at a $V_{DC} = \pm 1$ mV bias is obtained. These pinch-off gate voltages, or more tunnel-suppressing ones, are then maintained for the rest of the measurements during a single cooldown experiment. For Device

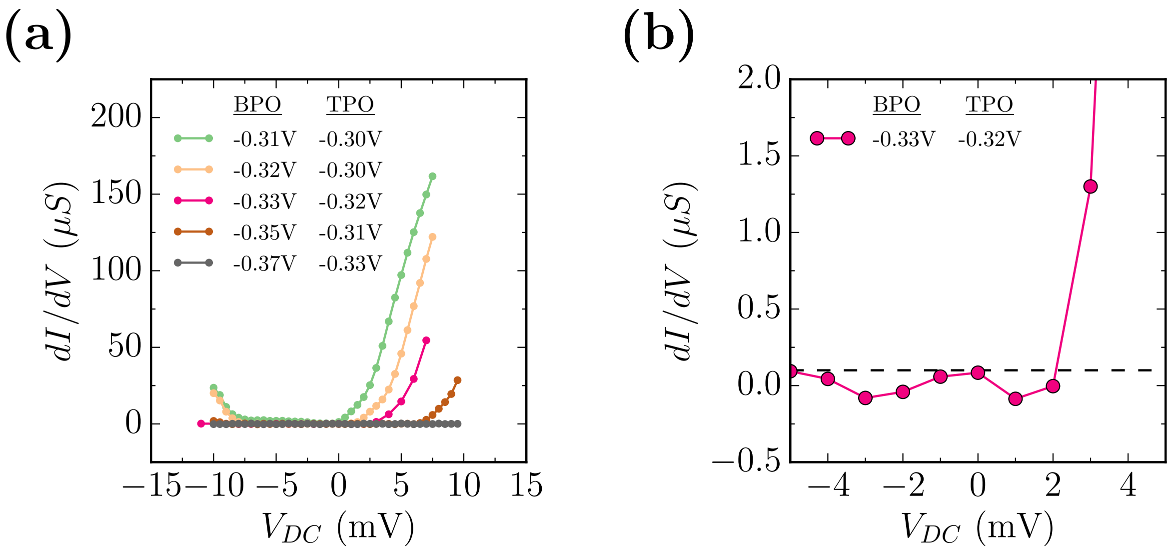

Figure 4.3: Tunneling characterization of Device A using circuit from Fig. 3.3a and numerical differentiation. (a) Complete sweep range. (b) Zoom on the < 0.1 μS (or > 10 MΩ) region where a suitable configuration (displayed) can be identified.

.

A under these specific cooldown conditions, BPO was kept below -0.33 V and TPO was kept below -0.32 V.

4.1.3 Plunger gate scans

After the procedure described in the ealier section, the plunger gates are activated to form quantum wires by completing the split gate geometry. The conductances of the two wires are measured as a function of the various gate voltages so as to find a regime where the lowest lying subbands can be aligned for the measurements. Owing to the close proximity of the quantum wells, modifying the voltage of a single plunger gate invariably affects the conductance of the two wires. This can then be exploited to measure Coulomb drag across a range of subband configurations in the two wires by sweeping only one plunger gate while leaving all other gates fixed.

4.1.4 Effects of cooldown conditions on bilayer

Prior to successfully studying drag in Device A, its properties had to be adjusted to make the wires more similar in terms of conductance and pinch-off voltage. These properties are known to be sensitive to cooldown conditions, especially in the new heterostructure used.

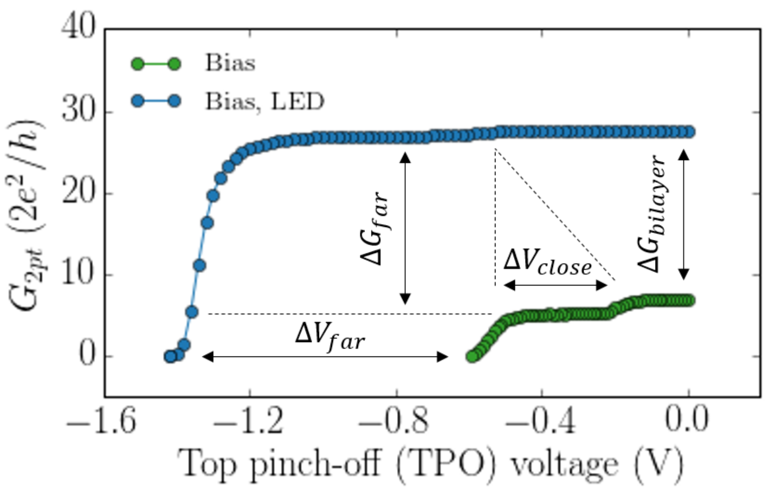

Figure 4.4: PO sweep with the same gate from cooldowns with and without LED illumination. Graphically represented are the absolute differences Δ between the quantities of interest. These are the shift in bilayer conductance ($\Delta G_{bilayer}$), shift in opposite well conductance ΔV_{far} (here, TPO being is swept, the bottom layer), shift in closer layer pinch-off voltage ΔV_{close} (top layer), and shift in opposite layer pinch-off voltage ΔV_{far} (bottom layer).

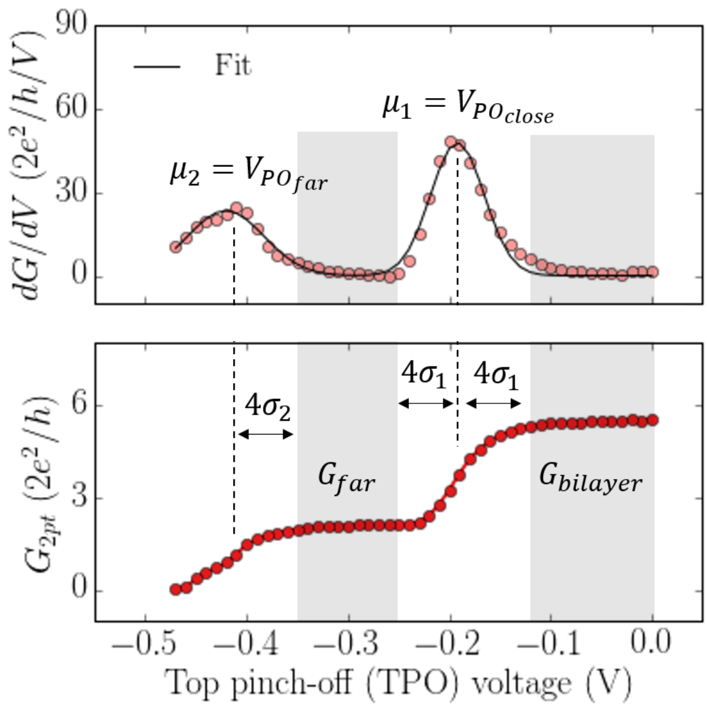

Figure 4.5: Extraction of the quantities required to calculate the shifts. The pinch-off sweep (bottom) is differentiated (top). Depletion regions become peaks whose positions and width can be fitted with a function $A_1 \cdot e^{-\frac{(x-\mu_1)^2}{2\sigma_1^2}} + A_2 \cdot e^{-\frac{(x-\mu_2)^2}{2\sigma_2^2}}$. The plateau regions of constant conductance in the sweep (shaded) are then identified as the regions away from the peaks.

		$G_{bilayer}$			G_{far}			V_{close}			V_{far}		
BPO	Δ ($2e^2/h$ or V)	1.12	$\pm$	0.06	0.7	$\pm$	0.2	-0.04	$\pm$	0.08	-0.02	$\pm$	0.08
A$\rightarrow$B	X_2/X_1 (unitless)	1.182	$\pm$	0.008	1.15	$\pm$	0.03	1.2	$\pm$	0.3	1.03	$\pm$	0.06
BPO	Δ ($2e^2/h$ or V)	1.37	$\pm$	0.07	0.8	$\pm$	0.2	-0.02	$\pm$	0.07	-0.01	$\pm$	0.06
A$\rightarrow$D	X_2/X_1 (unitless)	1.249	$\pm$	0.008	1.16	$\pm$	0.03	1.1	$\pm$	0.3	1.01	$\pm$	0.09
TPO	Δ ($2e^2/h$ or V)	1.39	$\pm$	0.08	2.98	$\pm$	0.04	0.01	$\pm$	0.06	-0.12	$\pm$	0.08
A$\rightarrow$D	X_2/X_1 (unitless)	1.255	$\pm$	0.009	2.427	$\pm$	0.008	1.0	$\pm$	0.2	1.3	$\pm$	0.1
TPO	Δ ($2e^2/h$ or V)	2.04	$\pm$	0.08	2.59	$\pm$	0.06	0.01	$\pm$	0.05	-0.11	$\pm$	0.09
C$\rightarrow$D	X_2/X_1 (unitless)	1.60	$\pm$	0.01	2.50	$\pm$	0.02	1.0	$\pm$	0.2	1.3	$\pm$	0.1

Table 4.1: Shifts of Fig. 4.4 between initial (1) and biased (2) cooldowns.

Indeed, the very highest mobilities are only achieved under proper light-emitting diode illumination [71]; while the exact causes are not fully understood, the release of electrons trapped in deep donor centers is thought to be involved, thereby increasing electron density and reducing charged impurity scattering. The overall stability of gated nanostructures can also be improved by imposing a positive bias during cooldown [72]. Interestingly, such a procedure has also been reported to reduce the absolute value of the pinch-off voltage by the applied bias.

Device A was therefore cooled under three different sets of conditions : (1) with all gates grounded and without LED illumination; (2) with TPL held at +0.26 V, BPL held at +0.35 V, and without LED illumination; and (3) with TPL held at +0.26 V, BPL held at +0.35 V, and with 40 μA being run through a red LED nearby the sample. When biased, the gates were grounded at 4 K. When illumination was performed, the LED was slowly switched off beginning at 8 K. The original positive voltages chosen for the biased cooldowns were meant to "shift" the two wires by the requisite amount to bring them together at the PO voltages most studied on the first cooldown; furthermore, only the biasing of plunger gates was considered due to their less global effect. In practice, however, the selected voltages were limited by leakage current arbitrarily restrained to 1 μA at room temperature. This leakage had become negligible by the time 4 K was attained. Nonetheless, as will be discussed in the next section, these voltages allowed the wires to be made similar enough for practical purposes in configuration (2).

The pinch-off curves displayed in Fig. 4.2 differed upon the cooldown conditions. Fig 4.4 shows these curves for the (more significant) difference between conditions (2) and (3) with shifts of interest being indicated for one of the four measurement geometries. Reporting these shifts might prove useful for future studies of the drag devices, or of 2DEGs in GaAs/AlGaAs heterostructures in general.

Fig. 4.4 (bottom) displays the condition (1) setup along with the analysis method se-

		$G_{bilayer}$			G_{far}			V_{close}			V_{far}		
BPO	Δ ($2e^2/h$ or V)	20.4	±	0.1	17.0	±	0.7	-1.07	±	0.08	-1.49	±	0.07
A→B	X_2/X_1 (unitless)	3.806	±	0.008	3.89	±	0.03	6.1	±	0.2	3.16	±	0.06
BPO	Δ ($2e^2/h$ or V)	20.6	±	0.2	17.6	±	0.7	-1.10	±	0.09	-1.51	±	0.06
A→D	X_2/X_1 (unitless)	4.005	±	0.008	4.14	±	0.03	6.5	±	0.2	3.19	±	0.05
TPO	Δ ($2e^2/h$ or V)	20.74	±	0.06	21.4	±	0.5	-0.4	±	0.09	-0.79	±	0.08
A→D	X_2/X_1 (unitless)	4.025	±	0.007	5.23	±	0.02	3.1	±	0.2	2.44	±	0.08
TPO	Δ ($2e^2/h$ or V)	22.29	±	0.08	22.0	±	0.4	-0.39	±	0.09	-0.80	±	0.09
C→D	X_2/X_1 (unitless)	5.12	±	0.01	6.10	±	0.02	3.1	±	0.2	2.5	±	0.1

Table 4.2: Shifts of Fig. 4.4 between biased (2) and biased and illuminated (3) cooldowns.

lected to standardize shift extraction (top). To standardize the extracted values, the numerical derivative of the PO sweep is computed, yielding two peaks associated with well depletion; a Savitzky–Golay filter [73] was applied to remove high-frequency noise that would obscure the depletion peaks. The peaks labeled $i = 1, 2$ are then fitted with Gaussians[1], yielding standardized gate voltages for depletion in the mean μ_i of the distribution, with associated error in peak standard deviation σ_i. It also delineates the non-depletion regions with constant conductance, allowing a conductance to be unambiguously averaged (and an associated error obtained from the spread via the standard deviation). Note that when the Python fitting software was not able to fit a Gaussian to the peak, the peak could still be graphically identified and its maximum value was used to infer the depletion voltage and its full width at half max (FWHM) to obtain its standard deviation via $\text{FWHM}_i = 2\sqrt{2\ln 2} \cdot \sigma_i$ following Gaussian statistics.

The shifts (both the difference in values $\Delta \equiv X_2 - X_1$ and ratios X_2/X_1, where X is either $G_{bilayer}$, $G_{furthest}$, $V_{PO_{close}}$ or $V_{PO_{far}}$ and 1 and 2 denote the two cooldown conditions being compared) are tabulated in Tables 4.1 and 4.2. From Table 4.1, it is seen that cooling the device with the plunger gates biased improves the conductance of the structure. This could be due to the reduction of ionized donors underneath the plunger gates which improves the electron mobility in the region of the 2DEG underneath the plunger gates. This is a region contributing, but not exclusively so, to the total conductance measured. The pinch-off voltages of the pinch-off gates do not change significantly, likely due to the fact that the plunger gates affect the 2DEG in a different area than the one gated by the pinch-off gates. From Table 4.2, we see that cooling the device under LED illumination significantly increases the conductances of

[1] The subthreshold region where depletion occurs in a field-effect transistor formally corresponds to the transition between exponential (source/drain thermionic emission-dominated behaviour) and algebraic (saturation behaviour) dependence of the current (or conductance) as a function of gate voltage. Hence, on physical grounds, a symmetrically-exponential Gaussian should not adequately fit the exponential-to-algebraic features. In practice, however, it provides a suitable way to identify the depletion regions.

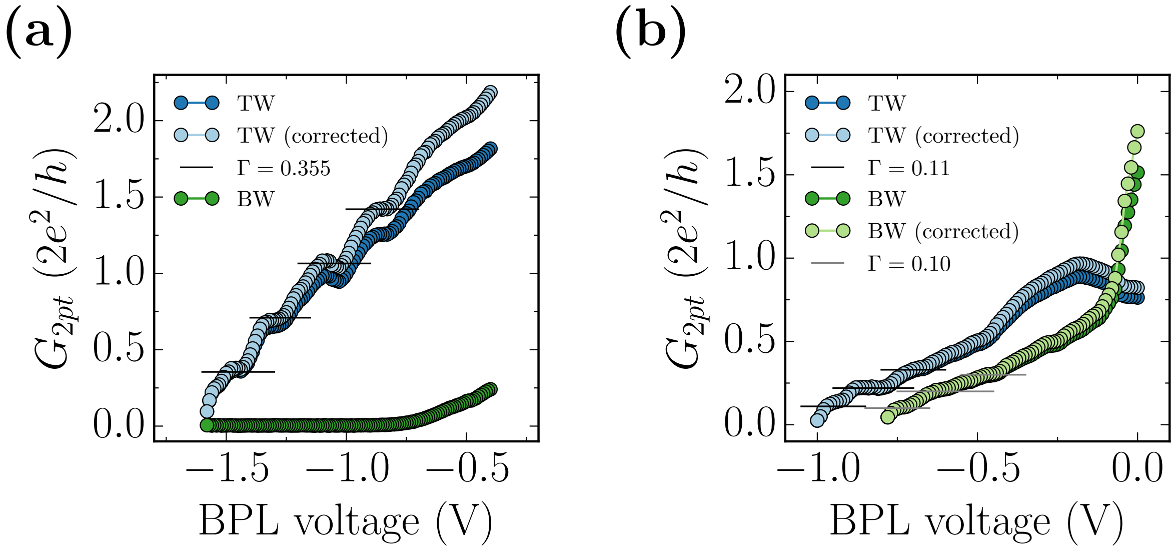

Figure 4.6: Device A's wires in the initial unbiased and nonilluminated cooldown. The corrected conductances refer to the measured conductances from which a 1.2 kΩ was substracted, and tentative even $\Gamma \times 2e^2/h$ conductance spacings are overlaid. (a) Less gated configuration with BPO set to -0.37 V, TPO set to -0.235 V, and TPL set to -1.49 V. (b) After reducing the conductances with BPO set to -0.55 V, TPO set to -0.235 V, and TPL set to -1.92 V.

.

the device and displaces the pinch-off voltages to more negative values. These two observations could be explained by electrons being released from impurity centers by the LED photons, increasing the 2DEG densities and hence conductivities and voltages required for full gating. Under illumination, phenomena occuring in the ohmic contacts could also be at play. In any case, a quantitative analysis of the systematic dependence of device performance on cooldown conditions is outside the scope of this thesis. These shifts are reported here to guide future cooldowns, since for Device A these varying cooldown conditions allowed drag experiments to be performed in similar subband occupancy regimes. This is discussed in the next section.

4.1.5 Wires in different regimes

In a minimally-gated configuration, *i.e.* at the early stages of plunger gate optimization, the wires of Device A when cooled down without bias or illumination greatly differed in conductance and pinch-off voltage, as shown in Fig. 4.6a. While the top wire displayed plateau-like features, the bottom wire was in the diffusive regime. The top wire's plateaus appear to be evenly-spaced by $\approx 0.355 \times 2e^2/h$ when a 1.2 kΩ series resistance was removed from the 2pt

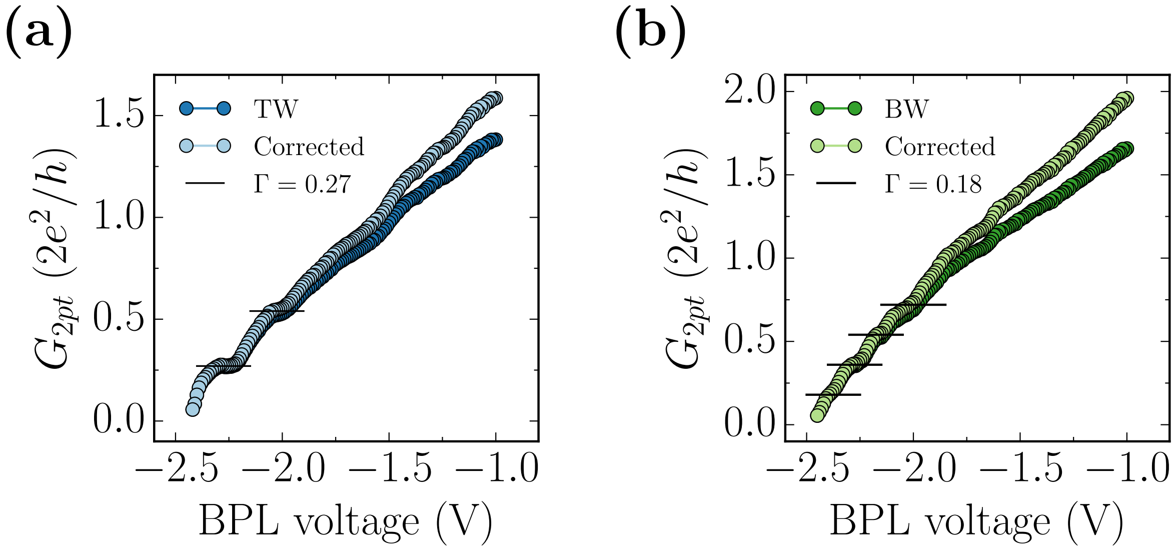

Figure 4.7: Device A's wire after the biased, but nonilluminated, cooldown. The corrected conductances refer to the measured conductances from which a 1.2 kΩ was substrated, and tentative even spacings are overlaid. Less gated configuration with BPO set to -0.35 V, TPO set to -0.30 V, and TPL set to -1.30 V. (a) Top wire. (b) Bottom wire.

.

conductance[2].

A gating voltages configuration of the initial, unbiased cooldown with more similar wires is presented in Fig. 4.6b. To achieve this, the top wire had to be made more resistive than its most conducting value by lowering the BPO voltage (which, when the bottom well is already depleted, affects the top wire more than the bottom wire due to more pronounced shadowing) down from a relatively high tunneling-suppressing value of -0.37 V to -0.55 V. TPL was set to -1.92 V, which is a lower value than even the lowest BPL considered during sweeps. Further lowering BPO or TPL did not improve the wires' similarity or caused too much leakage current as previously discussed. In this configuration, the lowest-order conductance plateaus are approximately evenly-spaced as $\approx 0.11 \times 2e^2/h$ for TW and $\approx 0.10 \times 2e^2/h$ for BW. A 1.2 kΩ series resistance was substracted in both cases. The wires are however sufficiently resistive that such 1 kΩ ($\sim 3 \times 2e^2/h$) in series do not significantly affect the spacing. In this configuration, the bottom wire had its lowest subband populated while the top wire had two (or three) subbands occupied.

The biased cooldown of configuration (2) improved the situation. The minimal tunneling-

[2]This approximate value is chosen because it yields evenly-spaced values and is of the same magnitude as what had been independently-determined in previous studies [3–5]

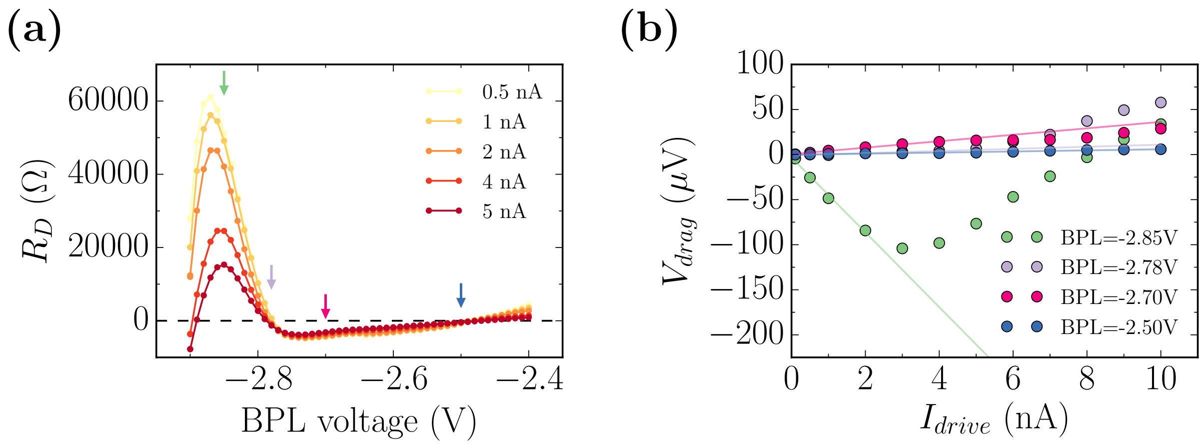

Figure 4.8: Linearity of the drag in Device A. (a) Repeated Coulomb drag sweep at different drive currents in Device A. (b) Drag voltage as a function of drive current at fixed plunger gate voltage (indicated by arrows in the left plot). A linear fit is performed in the low current region.

.

suppressing gate voltages conductances under these cooldown conditions are displayed in Fig. 4.7. Sweeping only BPL yielded two wires displaying well-defined subbands, and spaced by $\approx 0.27\ \times 2e^2/h$ for the top wire and $\approx 0.18\ \times 2e^2/h$ for the bottom wire. More importantly, the pinch-off voltages of the two wires were nearly identical, enabling a regime where the two wires' lowest-lying subbands could be aligned for drag experiments when tuning TPL and the various POs.

4.2 Drag tests

Drag measurements were then performed for the optimized wire configuration according to the scheme of Fig. 3.4a. Various checks are performed on the drag resistance to ensure that it is indeed originating from Coulomb drag. Note that due to difficulties in aligning the subbands for device A, the drag tests were not systematically performed for all gating configurations. The tests presented below may thus not have been performed in the regime presented in Sec. 4.2.5, although they may still give indications as to the quality of the drag.

4.2.1 Linearity of drag voltage with drag current

The drag experiment is repeated with various input voltages to ascertain that it is in a linear regime, as displayed in Fig. 4.8a. For instance, the 1D-1D drag signal is strongly temperature-dependent as detailed in Sec. 2.3.1. To complicate matters, the reduced-dimensionality of the conductors at ultralow temperatures make them prone to self-heating as discussed previously. To rule out such contributions, only experiments performed in the low-current region where drive current and drag voltage are linearly related are considered.

The region of linearity is most easily observed at fixed gate voltage. Fig. 4.8b shows such cuts. For Device A, the drag voltage at a given gate voltage is extracted for each curve and plotted as a function of the drive current. The drag voltage is nonlinear in drive current with an inflection current that becomes smaller with more negative plunger gate voltage. This would intuitively be expected, as the conductance of the wires increases with decreased gate voltage, leading to more Joule dissipation : at BPL set to -2.85 V, this is calculated to be as high as the ~ 10 pW (as compared to ~ 500 fW at the next displayed BPL gate voltage of -2.77 V). Beyond purely resistive effects, we cautiously note that the region of most significant nonlinearity occurs in the tentative 1D-1D regime. Without a proper conversion method between dissipated power and electron temperature, it is difficult to convert the $R_D(I_{drive})$ data to $R_D(T)$ to establish if this is indeed related to the stronger 1D-1D R_D temperature dependence discussed in Sec. 2.3.1.

4.2.2 Probe symmetry

The drag measurement is then studied upon reversal of the current and voltage probe orientations. A priori, the signal is not expected to change, unless mesoscopic effects are non-negligible, for instance through direction-dependent Landauer-Büttiker transmissions. Previously, the drag resistance was found to quantitatively satisfy probe symmetry when positive, but to differ in magnitude when negative [3]. Fig 4.9 displays this test for given configurations of the wires in Devices A. For this device, in the configuration for which it was tested, probe symmetry does not seem to be quantitatively satisfied since the curves seem vertically offset. This could be explained by the aforementionned temporal drift of the drag signal or sensitivity to changes in the electrostatic environment. An undiagnosed grounding issue could also be at play. Further measurements would be required to elucidate this effect.

4.2.3 Layer reversal symmetry (Onsager relations)

The drag measurement is then studied with the drive and drag wires reversed. According to the Onsager relations for identical wires, the signal should not change, although mesoscopic

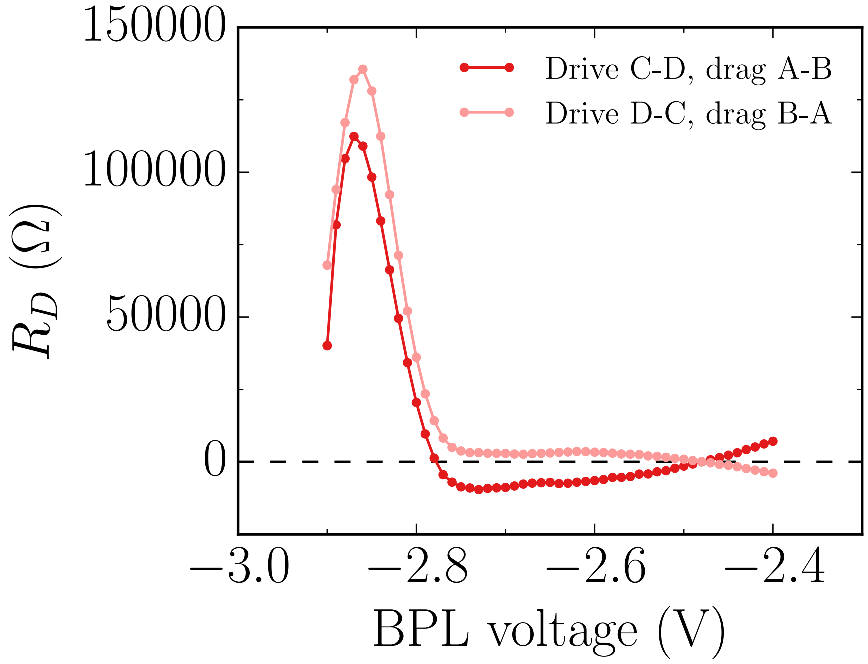

Figure 4.9: Probe symmetry of drag resistance in Device A .
.

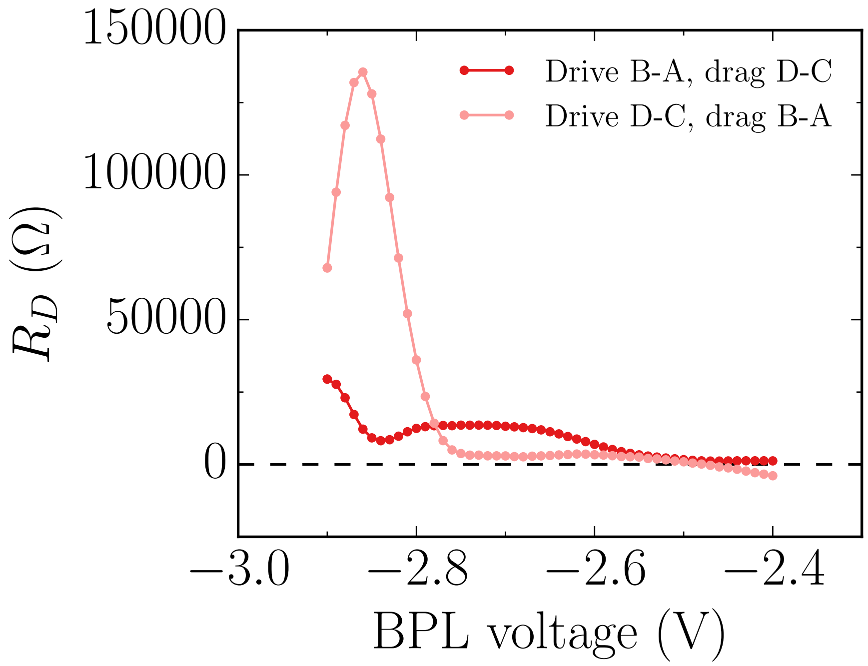

Figure 4.10: Layer reversal symmetry of drag resistance in Device A.
.

effects could make them violated [59–61]. Previously, in the 4.2 μm-long wires in a similar heterostructure as for Device B, the Onsager relations were found to not be completely satisfied. Both configurations, however, displayed positive and negative drag regimes, although not in the same voltage regions [3]. In Device A, this does not seem to be satisfied, as presented in Fig. 4.10. The same mechanisms affecting probe symmetry could be at cause.

4.2.4 Frequency independence

The drag measurement is then typically repeated at different frequencies to ensure that it is frequency-independent. While the drag itself should not depend on frequency, the refrigerators are wired with low-pass filters and the wiring itself has finite resistance and capacitance, as discussed in Sec. 3.1.2, so the measurements are performed at frequencies < 30 Hz to avoid building up an excessive out-of-phase signal. Previous experiments had reported slight quantitative differences in the signal, although all measurements shared the same features [3]. Unfortunately, this measurement was not performed in Device A, since its cooldown was cut short unexpectedly and the device was not subsequently successfully cooled for drag to be measured. Should the device be characterized again, testing if higher harmonics of the drag signal are generated would also be worthwhile.

4.2.5 Observation of re-entrant negative drag

While some drag tests were found to not be satisfactory, an attempt is made to analyze the Coulomb drag results in the light of the previous Coulomb drag experiments. In the future, more exhaustive experiments should be performed to confirm or infirm the findings. Coulomb drag for one of the gating configurations is presented in Fig. 4.11 with the wires overlaid. When the wires are more closely matched as in previous experiments, the same features previously-observed in the lower-mobility material are apparent. The drag resistance R_D displays regions of positive and negative value at higher densities than in the 1D localization regime previously reported in [65]. The local maxima also appear concomitant with subband openings. These features also appear at different, nearby TPL voltages. The magnitude of the drag is also consistent with that of previous experiments.

Finally, we note that although the bare wafer mobility is measured to be 5 times higher than in the previously-used heterostructures, the wire quality as reflected by the resolution of the plateaus and their spacing is less than in the best lower-mobility material first reported

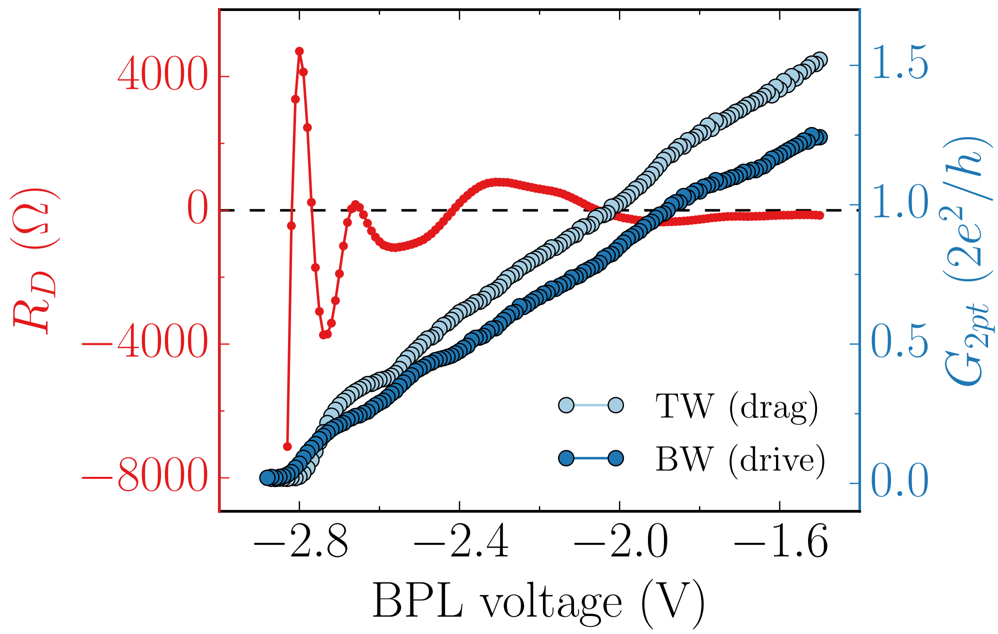

Figure 4.11: Re-entrant negative drag in Device A. This specific curve was obtained for BPO set to -0.35 V, TPO set to -0.31 V, and TPL set to -1.05 V under cooldown configuration (2).
.

in [4]. This could be due to wafer quality degradation during processing (the mobility post-patterning was not measured) or more likely unoptimized conditions : typically, the highest mobilities are obtained when cooling under LED illumination. Unfortunately Coulomb drag experiments were not performed in this regime due to the difficulty of gating the wires under these conditions and in successfully cooling down the device when this was attempted.

Chapter 5

Device B : short wires

Device B was fabricated in material provided from the Sandia collaboration (a copy of the previously-used heterostructures) and with wires with a lithographic length of 1 μm. This proved to be the first working device with wires of different length than the typical 4.2 μm. For this heterostructure type, the thermal length is estimated to be $L_T = \hbar v_F / k_B T \sim 2.5$ μm and the voltage length[1] is estimated to be $L_V = \hbar v_F / eV \sim 1.5$ μm [3]. Hence, this device could allow the study of Coulomb drag in a new regime where mesoscopic effects are expected to be magnified.

A characteristic inherent to Device B was the noticeable hysteresis of its TPL. As such, whenever possible, TPL was fixed and BPL swept. Another characteristic of the drag presented for Device B is the unoptimized cooldown conditions of the dry refrigerator when the first (and only) drag measurements were performed. Significant spurious noise was present : for instance, in a conductance measurement[2] the measured noise in TW at the gating voltages yielding the positive drag peak was $\sim$ 600 nV/$\sqrt{\text{Hz}}$. However, the equipment used should also have at best input noise of $\sim$ 50 nV/$\sqrt{\text{Hz}}$ [3]. Possible issues include potential grounding loops not having been eliminated, and the low-temperature RC filters being defective (see Appendix C for discussion). In this preliminary experiment, however, more averaging was employed in order to obtain the first drag data. Sweep rates of $\sim$ 0.05 V/min were used alongside lock-in time constants of multiple seconds, which has an effect of limiting the range and amount of measurements. Drag sweeps were nonetheless found to be quantitatively reproducible when swept up and down successively and also found to be qualitatively similar upon longer timescales.

Furthermore, jumps in conductance could be traced to be telegraph noise effects in the

[1] These are Fermi liquid quantities. They are used as estimates with a 1D Fermi velocity for the single subband regimes where Luttinger liquid theory should apply.

[2] The shot noise contribution associated with such a measurement scheme is calculated to be $\sim$ 1 nV/$\sqrt{\text{Hz}}$, and is hence neglected.

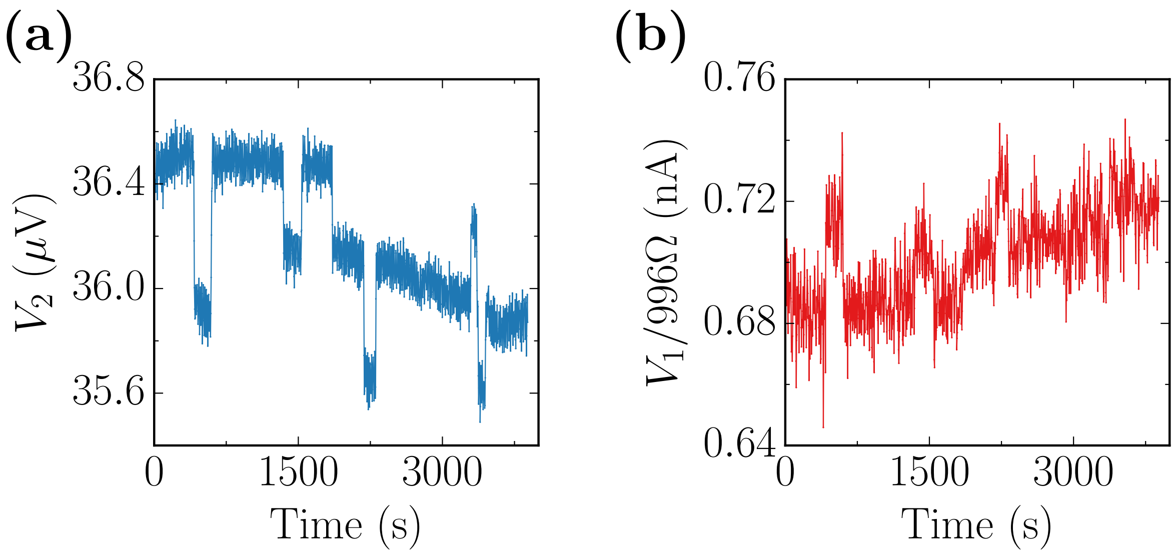

Figure 5.1: Time trace of conductance of the top wire of Device B for TPO set to −0.30 V, BPO set to −0.61 V, TPL set to −1.83 V, and BPL set to −1.60 V. (a) 4pt voltage ($V2$ in Fig. 3.2). (b) 4pt current ($V1$ in Fig. 3.2, divided by sense resistor value of 996 Ω). Jumps in the conductance might be attributed to switching noise, and temporal drift can be observed.

top wire. As displayed in Fig. 5.1, these jumps and temporal drift in the top wire conductance were preeminent, while the bottom wire conductance remained stable during the same sweep. The conductance jump varied between $0.01 \times 2e^2/h$ and $0.02 \times 2e^2/h$, which is consistent with previous investigations of switching noise in GaAs 2DEGs [72]. The period of the switching events turns out to be slightly larger than the typical drag sweep timescale. Imposing a positive voltage on the gates during cooldown could potentially alleviate or completely eliminate this issue as was reported in [72].

5.1 Wire characterization

The pinch-off gate sweeps, pinch-off gate optimization, and plunger gate scans of Device B are performed identically to Device A. Refer to Appendix D for the data and comments. The device did not have to be cooled under bias or illumination to obtain the wires of similar pinch-off voltage presented in this thesis. Furthermore, in the McGill dry refrigerator, four-point measurements were made possible due to all fridge wiring and device contacts being functional at the time of cooldown. In this geometry, the evenly-spaced plateaus should therefore be directly identifiable from the conductance sweep.

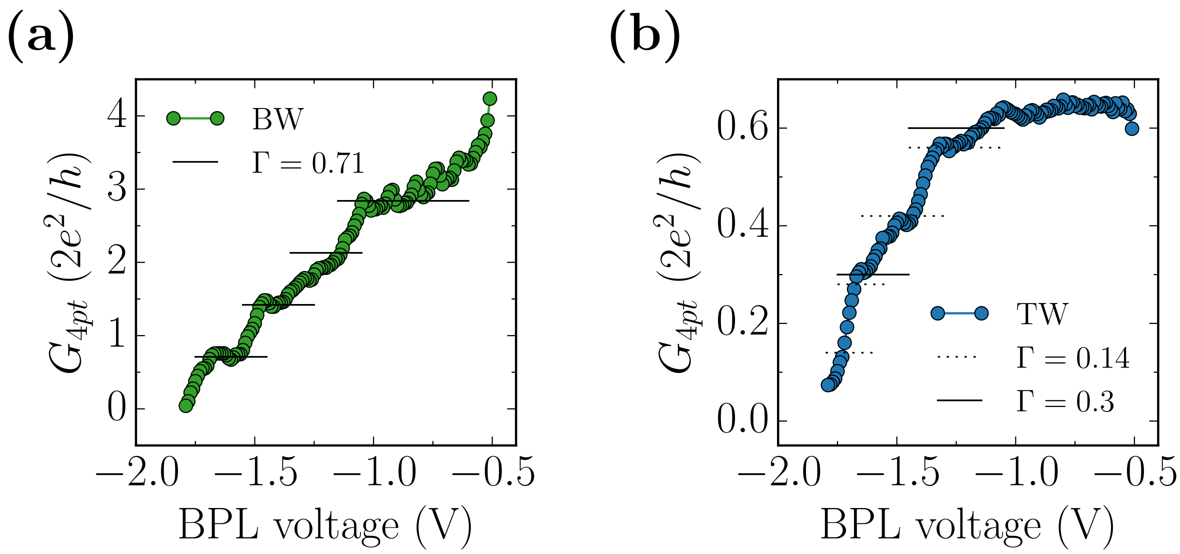

Figure 5.2: Four-point conductance of (a) bottom wire and (b) top wire of Device B in the most studied configuration with TPO set to −0.31 V, BPO set to −0.60 V, and TPL set to −1.62 V. Even conductance spacings $\Gamma \times 2e^2/h$ likely corresponding to conductance quantization plateaus are also plotted. The data are unsmoothed and taken in the McGill dry refrigerator.

Fig. 5.2 shows the four-point conductance of the wires in the gating configuration that was most studied. The bottom wire seems to display plateaus evenly-spaced by $0.71 \times 2e^2/h$, putting it in the non-ballistic regime but supporting the existence of well-defined 1D subbands. These wires were more conducting than any of the 5 μm wires previously-reported, as would be expected from a reduced wire length under similar lattice scattering conditions. It is however more difficult to identify plateau-like features in the top wire : even spacings of $0.14 \times 2e^2/h$ or $0.3 \times 2e^2/h$ could only tentatively be ascribed. Repeating the measurements in a more optimized setup could improve the overall wire quality. Nonetheless, drag experiments were carried with these wires.

5.2 Coulomb drag

The same drag tests were performed as for Device A. In Device B, drag was always measured using the symmetric circuit from Fig. 3.4b. Linearity of the drag and probe symmetry were found to be satisfied : again refer to Appendix D for the data and comments. The remaining tests were found less satisfactory and are therefore discussed below. Nonetheless, some of the previously-observed features of the drag were reproduced as will be discussed

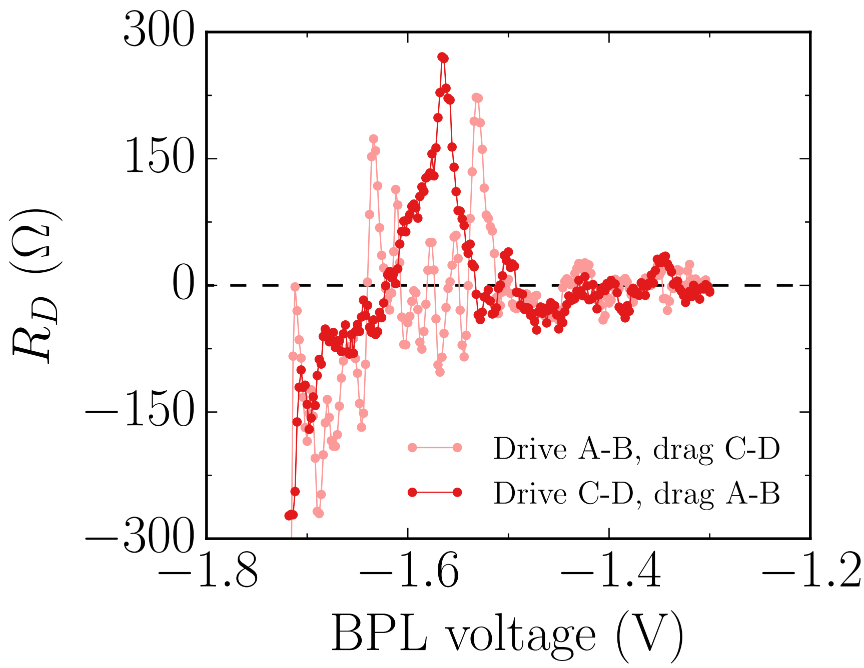

Figure 5.3: Layer reversal symmetry of drag signal in Device B (unsmoothed data taken in the McGill dry refrigerator).

.

subsequently.

5.2.1 Layer reversal symmetry (Onsager relations)

In Device B, it is not clear if the Onsager relations are satisfied. As reported in Fig. 5.3, the low and high gating regions seem to be identical. Interestingly, the more pronounced discrepancies appear in the middling region where the wires each have one or two subbands occupied. New measurements in an optimized measurement setup and with an increased gating range could settle this issue.

5.2.2 Frequency independence

In Device B, the Coulomb drag resistance was found to be quantitatively dependent on the frequency of the experiment as presented in Fig. 5.4. From the low-pass filter transfer characteristics compiled in Appendix C, we can estimate that in this range of frequencies the filter could cause a change in the real part of the signal up to 7%. Hence, the frequency dependence of the wiring does not seem to explain the larger frequency dependence observed. Similarly,

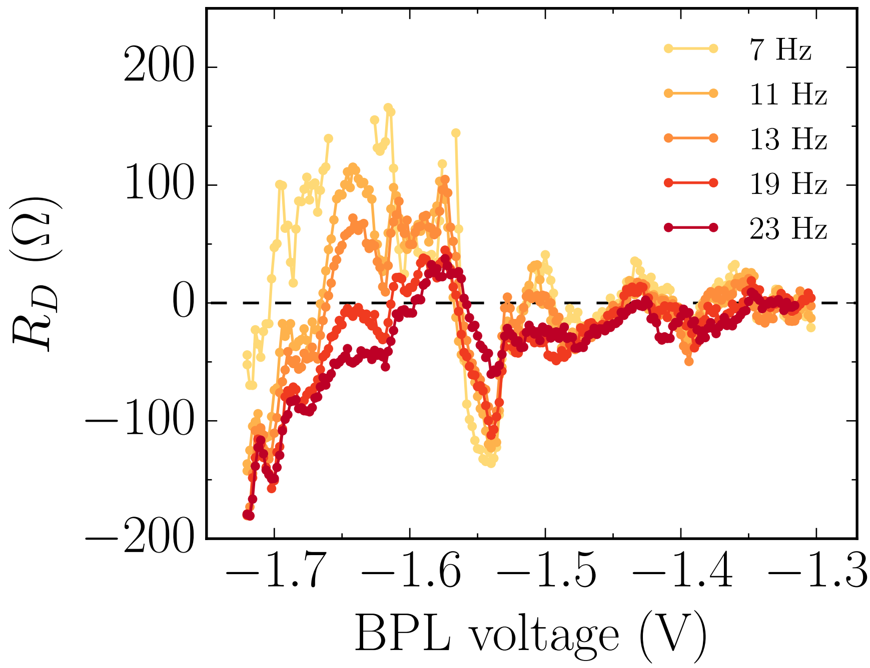

Figure 5.4: Frequency dependence of the drag signal in Device B (unsmoothed data taken in the McGill dry refrigerator).

the conductance of the wires was measured at these different frequencies, but no change in the $G(V_{BPL})$ behaviour that could explain modified features was observed. We however note that the most important deviations are observed in the voltage range corresponding to single subband occupation of the wires.

5.2.3 Discussion of re-entrant and weak Coulomb drag

Measuring drag in Device B requires amplification of the drag voltage. Typically, a gain of 100 was used, although the signal was also measured with different gain to ensure that no artefact was formed during the amplification chain. A typical sweep for relatively matched wires is presented in Fig. 5.5. Again, in the small range of gate voltages considered, the signal possesses the typical features of high-density negative drag with maxima concomitant with (possible) subband opening. Studying the drag on a larger range of swept gate voltages (BPL) so as to reach a regime where more than two subbands are occupied would be the logical next step. Equally important would be exploring drag under a wider range of the fixed gate voltages (TPL and POs) so as to align the wires with different subbands.

A reduction of the drag magnitude compared to previous experiments at the temper-

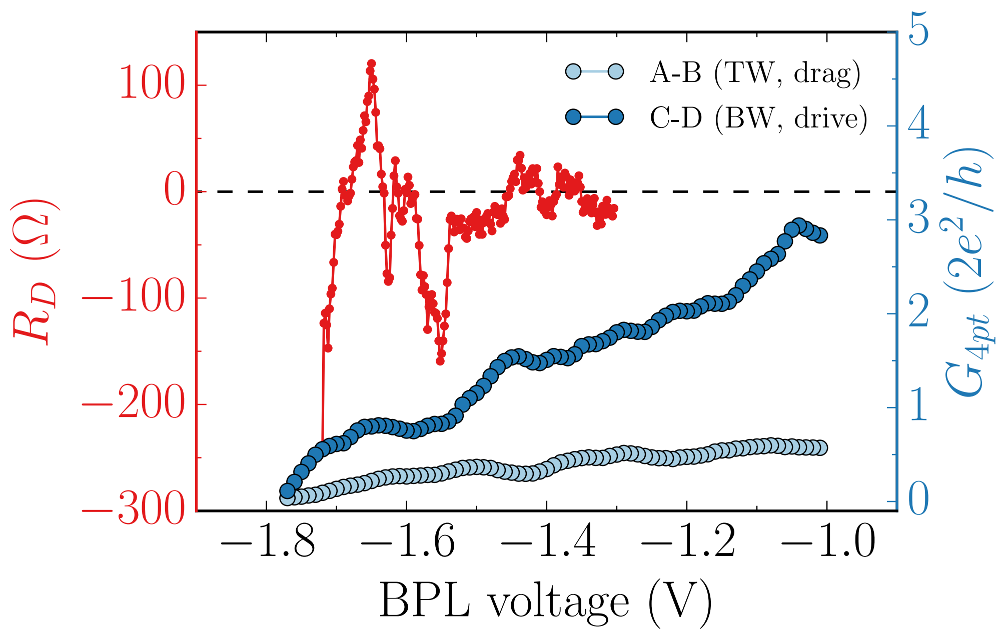

Figure 5.5: Reentrant negative drag in Device B. This specific curve was obtained for TPO set to -0.31 V, BPO set to -0.60 V, and TPL set to -1.62 V using a 13 Hz excitation frequency. Unsmoothed data taken in the McGill dry refrigerator.

.

atures considered may be expected from the backscattering theory of [46], since there is less overlap of the two wires for the drag mechanism to occur. Here, magnitude of the drag resistance indeed seems to be smaller than for the longer wires, both those of Device A and those from previous experiments in Sandia material [3–5]. Caution must be exerted, however, since many different mechanisms affect the magnitude of the drag resistance. One of them, the interwire distance between the wires, is not completely well-controlled across devices due to possible horizontal misalignment of the wires. Similarly, differences in density mismatch is also possible across devices. Also, studying the temperature dependence of the drag would be required to establish if heightened electron temperature effects are at play : saturation at a higher electron temperature could also lead to perceived lower drag magnitude. In addition, the upturn in temperature should be suppressed for a wire overlap less than $L^* \sim 0.5$ μm in these wires. Such a temperature dependence could establish if this effect is present. This measurement should therefore be of high priority when this device is recharacterized.

Chapter 6

Conclusions

In this thesis, Coulomb drag experiments in vertically-integrated quantum wires were presented. Chapters 2 and 3 focused on reviewing the requisite background and past experimental methods related to these experiments, with additions where warranted. Chapters 4 and 5 presented the newest results of this study : Coulomb drag measurements in quantum wires in two new devices.

6.1 Summary of results

One of the new devices was defined in a heterostructure grown in a molecular beam epitaxy chamber reputed to yield the highest quality GaAs/AlGaAs systems ever reported. The previously-measured unpatterned mobility of the specific wafer was 6.0×10^6 cm^2/Vs (compared to 1.2×10^6 cm^2/Vs in the previously-used heterostructures). While the wires themselves did not seem to be improved, this is possibly due to fabrication-induced damage or unoptimized cooldown conditions. In this device, the Coulomb drag signal was found to be similar than in previous experiments using a wafer with a lower bare mobility. This comes with the caveat that some of the drag tests were not found to be completely satisfactory. The two electron layers of the heterostructures were also found to be different in terms of conductance, however different cooldown conditions such as biasing of the gates and illumination sucessfully modified these characteristics, with the results reported to assist future experiments.

The other device was defined in a copy of the previously-used heterostructures, but with wires with a lithographic length 1 μm rather than 4.2 μm. While drag experiments were only performed once and under unoptimized noise conditions, the drag signal observed as a function of plunger gate voltage was nonetheless found to be similar than in previous experiments. To pursue drag experiments in this device, including studying the dependence of the 1D-1D drag on temperature or addressing the impact of mesoscopic models of drag on the signal, questions related to the non-reciprocity of the drag upon layer reversal and the dependence of the drag signal frequency should first be clarified.

6.2 Outlook

We have barely scratched the surface of what is possible to study using the strongly-coupled quantum wires presented in this thesis. The most straighforward modifications include further varying the device parameters – wire lengths, barrier size between the 2DEGs, etc. Similarly, systematically studying $R_D(T)$ for different subband alignments is possible using the existing devices and would be of interest. Beyond, a large amount of new and interesting physics is at hand if the current device design is modified or new measurements techniques introduced.

A hallmark of Luttinger liquid physics is the separation of spin and charge degrees of freedom. As such, studying R_D under magnetic fields parallel or perpendicular to the wires is of great interest. A magnetic field would also increase correlations, leading to further deviations from noninteracting expectations as in previous Coulomb drag experiments [65]. Once this is achieved, further scrambling the nuclear spin ordering with a RF coil in a resistively-detected nuclear magnetic resonance scheme may yield further information [74]. Another possibility offered by a strong magnetic field is the possibility to perform DC bias spectroscopy to elucidate whether the oscillations in R_D as subbands are accessed extend to the spin-resolved regime [75].

Through the expected decoupling of heat and charge flows, coupled nanoscale systems and Luttinger liquids are both expected to yield strikingly different thermoelectric behaviour than in non-interacting electronic systems. A subset of the numerous possibilities offered in our 1D-1D drag platform is explored in-depth in Appendix E.

Adding more electrostatic gates to the devices would further expand the experimental space. One might envision controlling the electronic densities of the two wires through large flatgates. In its simplest iteration, it could simply be performed using a doped GaAs substrate in the EBASE procedure alongside a flip-chip topgate, or incorporating new gates in the existing e-beam writing of the wires. This would allow the exponential dependence of R_D on the density mismatch of the wires to be explored [56]. Also of interest would be the addition of a local split-gate across the wires, or a quantum point contact, in an attempt to study the "pinned" charge-density waves of the Luttinger liquid for which much has been discussed theoretically [22]. A quick calculation indicates that a stripe gate should be located a at maximum distance of 230 nm from the existing device topography so that the full-width at half maximum of the potential equates the characteristic lengthscale for pinning, that is the thermal wavelength of the electron liquid in GaAs (≈ 910 nm at 100 mK).

Of interest as well may be the study of the 2nd moment of R_D, that is the noise of the drag voltage. For instance, symmetries in the coupled Luttinger liquid Hamiltonian predicts the locking of the noise power in both wires [76]. Shot noise of the drag, possibly in conjunction with the local impurity described above, may also reveal effects of charge fractionalization in zero-field Luttinger liquids analogously to what was done for Luttinger liquids constituting fractional quantum Hall edge states [77, 78].

Although high-mobility AlGaAs/GaAs quantum well systems are now decades old, they still remain one of the, if not the, cleanest systems in which to observe the effect of electron-electron interactions. As such, the vertically-integrated quantum wire platform presented in this thesis constitutes a unique playground to study “quantum matter on-a-chip”.

Appendix A

Device parameters and estimates

Table A.1 presents the previously-characterized device parameters with relevant estimates as reported by Laroche *et al.* (private communications).

	Device A	**Device B**
Internal identification	Loren D-L	1Ddrag26-EA975-C
Wafer growers	L. N. Pfeiffer K. W. West	J. L. Reno M. P. Lilly
Affiliation	Princeton University	Sandia National Labs
Interwire separation (d)	~ 40 nm	~ 40 nm
Lithographic length (L)	4.2 μm	1 μm
2D combined mobility, pre-process (μ)	6.0×10^6 cm^2/Vs	1.2×10^6 cm^2/Vs
2D combined mobility, post-process (μ)	–	4.0×10^6 cm^2/Vs
Top 2DEG density (n_{2D}^T)	2.9×10^{11} cm^{-2}	1.1×10^{11} cm^{-2}
Bottom 2DEG density (n_{2D}^B)	2.4×10^{11} cm^{-2}	1.4×10^{11} cm^{-2}
1D density top wire ($n_{1D}^T = \sqrt{n_{2D}^T}$)	5.38×10^7 m^{-1}	3.50×10^7 m^{-1}
1D density bottom wire ($n_{1D}^B = \sqrt{n_{2D}^B}$)	4.90×10^7 m^{-1}	3.98×10^7 m^{-1}
Density mismatch ($\Delta n_{1D} = \lvert n_{1D}^T - n_{1D}^B \rvert$)	4.8×10^6 m^{-1}	4.8×10^6 m^{-1}
Average 1D Fermi wavevector (k_F)	8.1×10^7 m^{-1}	5.5×10^7 m^{-1}
1D Fermi temperature (T_F)	43.2 K	19.8 K
Fermi length (L_F)	12.4 nm	18.2 nm
$k_F d$	~ 3.2	~ 2.2

Table A.1: Device parameters obtained from previous characterization and associated estimates.

Appendix B

Dry refrigerator tail designs

The experimental tail in the new dry refrigerator was designed to hold 16-pin sample holders at the maximum of magnetic field. It was engineered to keep eddy current heating below the rated cooling power at 20 mK when the field is swept from 0 to 9 T in 90 minutes[1] [79]. It was also planned to have sub-minute thermalization time constants at base temperature. Fig. B.1 displays a diagram of the tail. Figs. B.2-5 display the associated schematics.

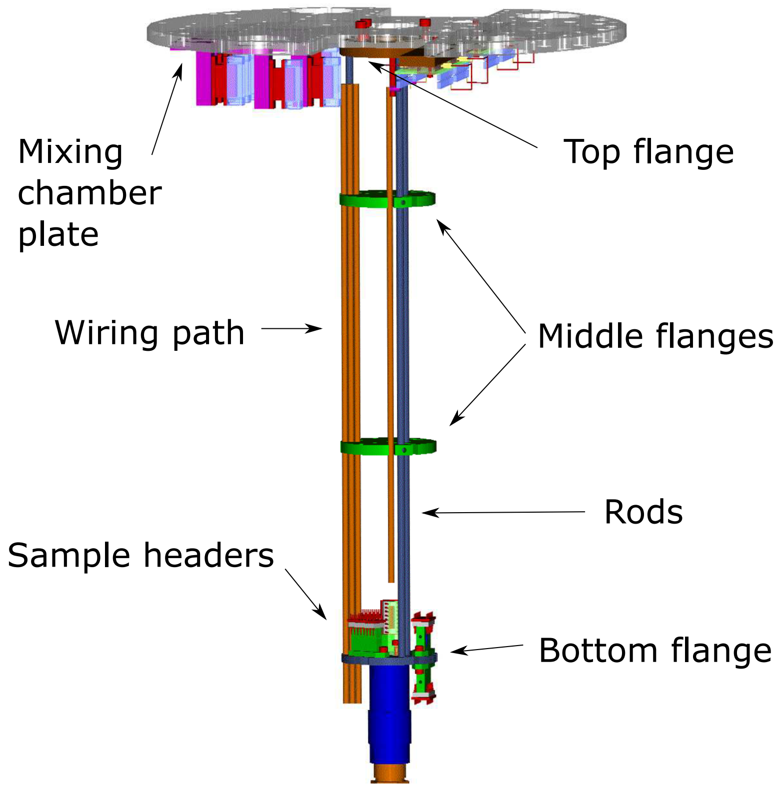

Figure B.1: Experimental tail. The top flange is designed to be fixed to the mixing chamber plate. The middle flanges ensure structural stability for the three rods as well as anchoring for the wiring. The bottom flange holds the sample headers at the maximum of magnetic field. CAD drawing courtesy of R. Talbot.

[1] For a sample plate made of 99% pure silver.

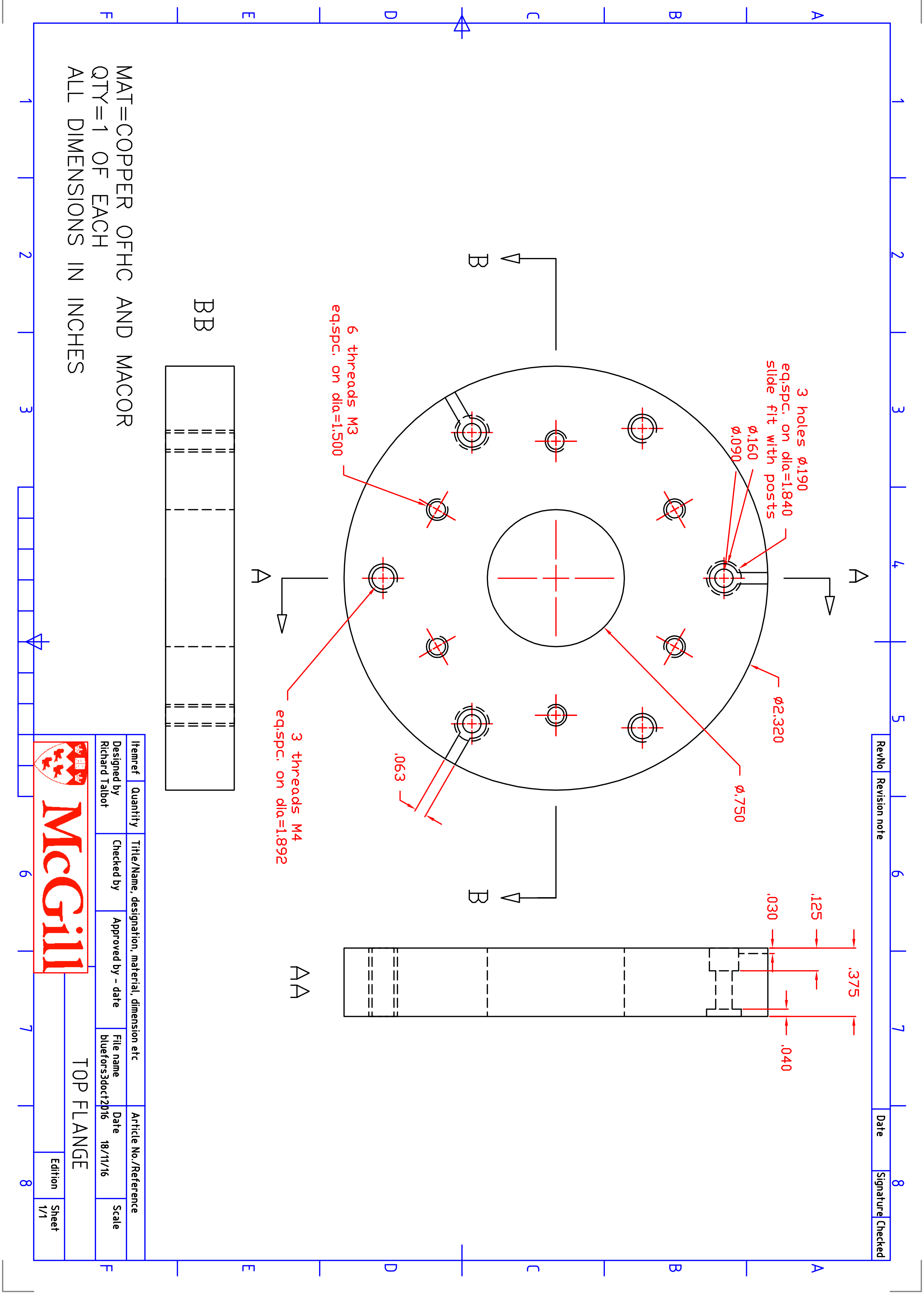

Figure B.2: Top flange schematic. CAD drawing courtesy of R. Talbot.

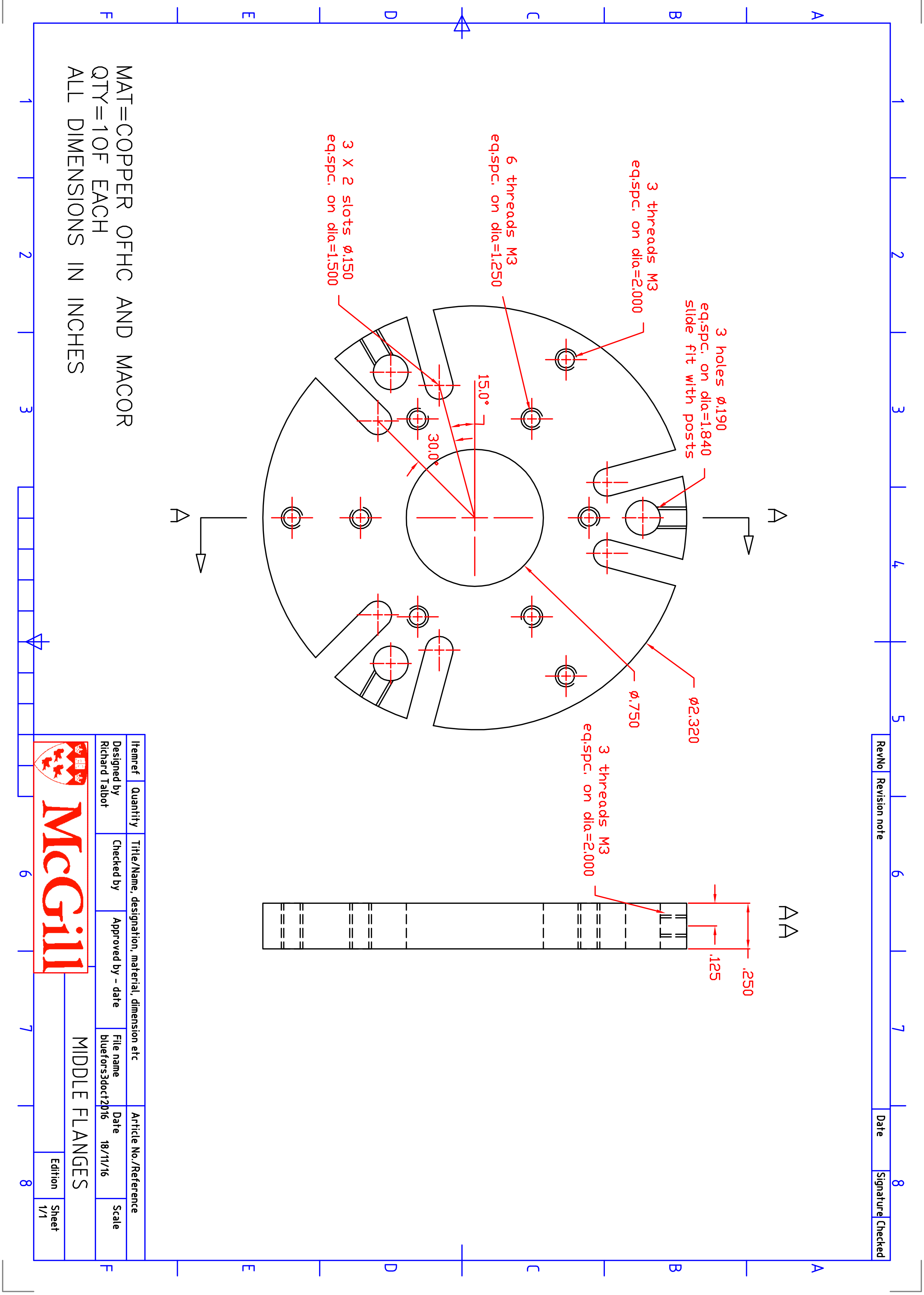

Figure B.3: Middle flanges schematic. CAD drawing courtesy of R. Talbot.

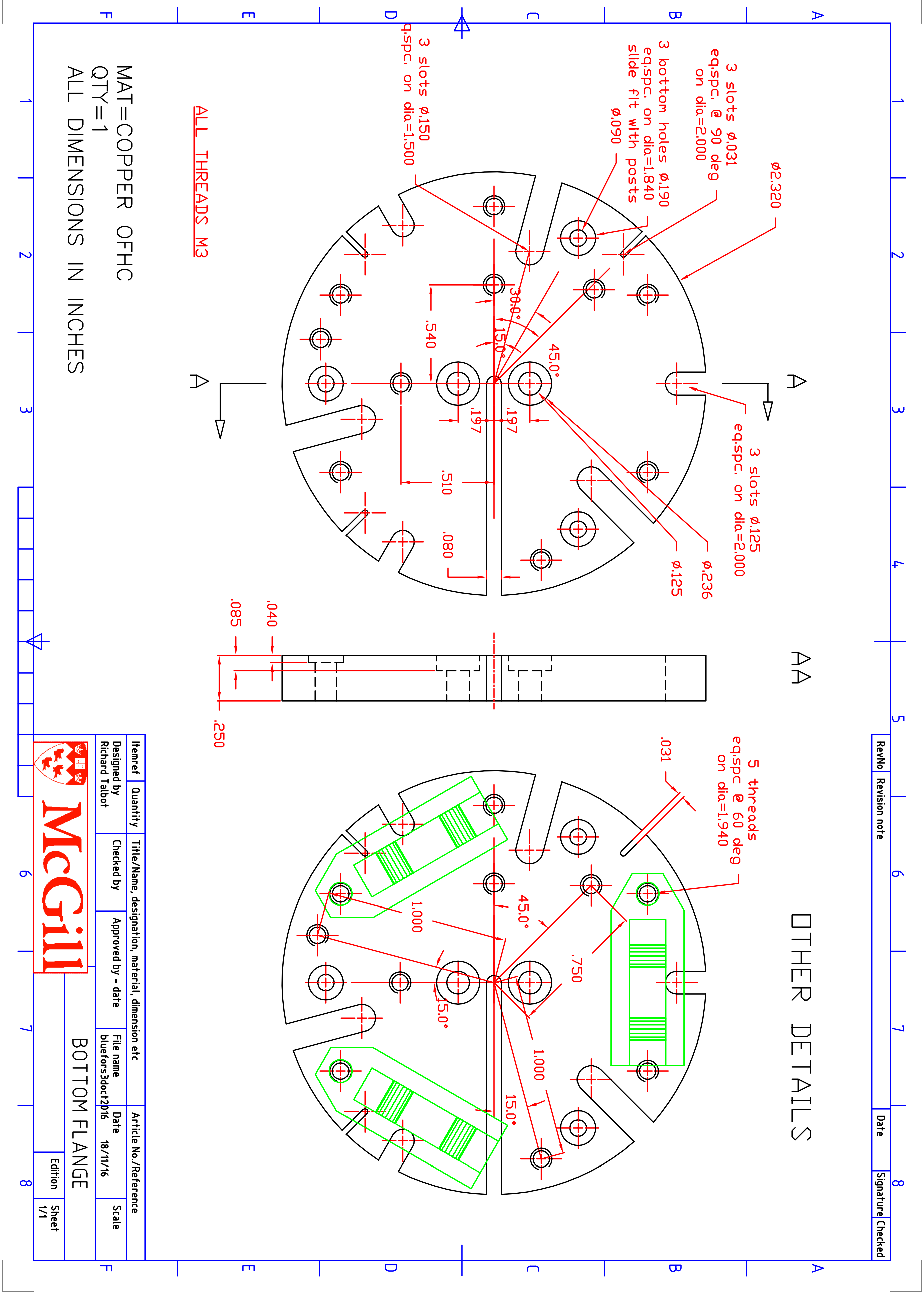

Figure B.4: Bottom flange schematic. CAD drawing courtesy of R. Talbot.

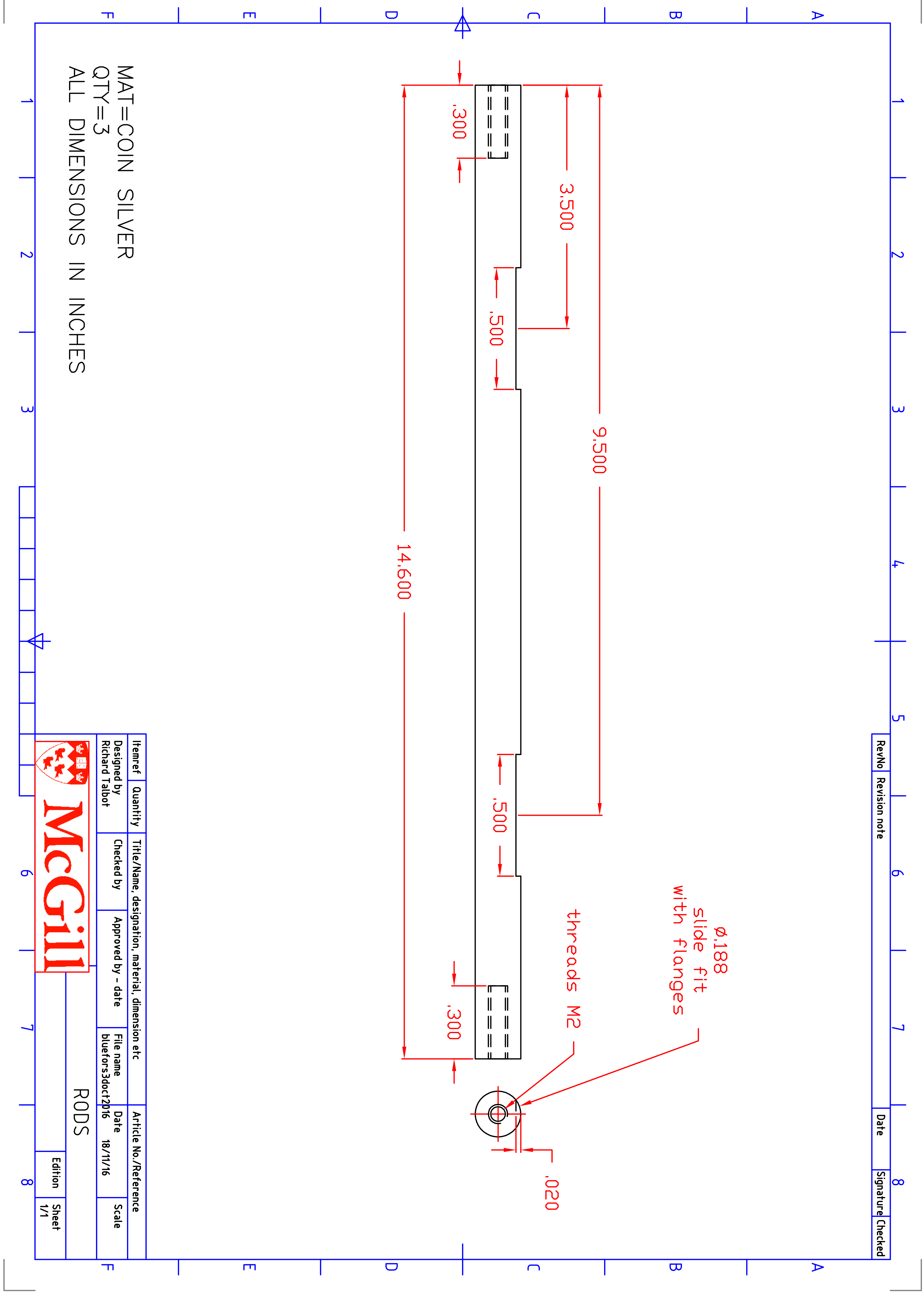

Figure B.5: Rods schematic. CAD drawing courtesy of R. Talbot.

Appendix C

Dry refrigerator wiring designs

In addition to the thermal anchoring included at the mixing chamber for the twisted pair wiring provided by Bluefors cryogenics, the experimental wiring is further filtered on the way to the sample stage, first through a modulable passive component filter and then a silver powder filter.

C.1 Wiring

The wiring configuration installed on the dry refrigerator tail is displayed in Fig. C.1. Eight twisted pairs of 0.004" heavy HML-coated 99.99% silver wires are soldered to the mixing chamber CINCH connector at one end and to a female connector on the other. A modular printed circuit board (PCB) accepts the connector. At the output of the PCB is another connector that mates to 0.0253' heavy HML 99.99% silver wires twisted pairs. This thicker wiring is then run through the silver powder filter for thermalization before leaving the mixing chamber level and snaking down the tail to the 16-pin header on the sample stage. The final connection between the thicker Ag wires and the header pins is performed in a hybrid fashion, with silver epoxy for thermal contact and tin/lead solder for mechanical stability and electrical conductivity since soft solder superconducts at operating temperatures.

C.1.1 Possible improvements

- The connections above the silver powder filter (from mixing chamber CINCH connector to small gauge wiring, from small gauge wiring to PCB mating connector, and from PCB mating connector to thick gauge wiring) could also be done in the hybrid silver/solder manner to improve electronic heat conductivity from the mixing chamber thermalization stage.

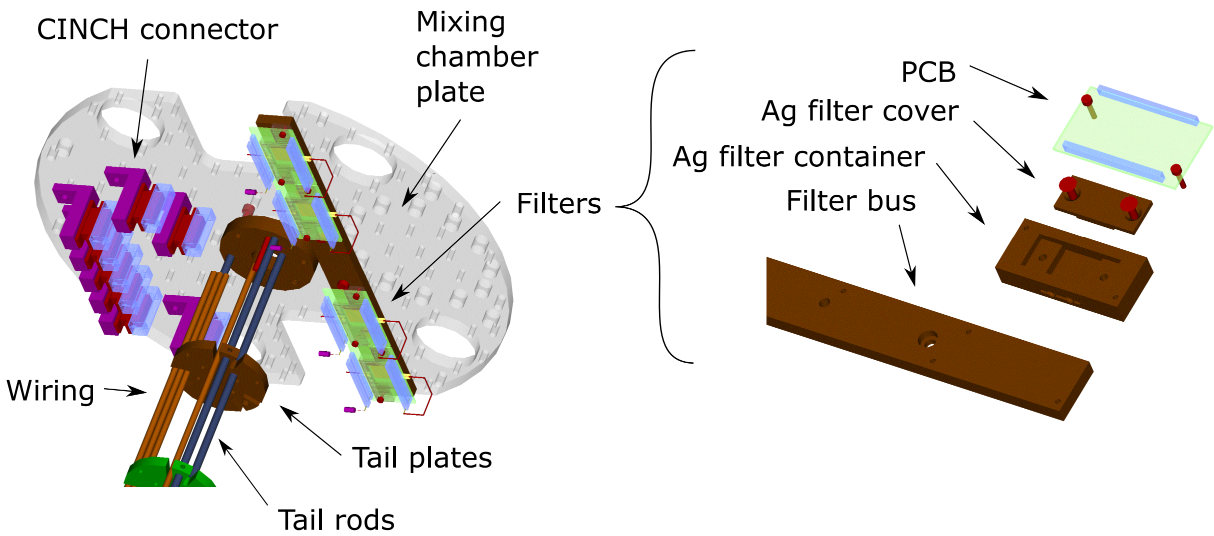

Figure C.1: Wiring configuration at the dry refrigerator tail. The compact filter layout is further detailed on the right side of the image. Every component is vertically overlaid on the next and fixed to an OFHC copper bus. The bus itself is fixed to the mixing chamber plate. CAD drawing courtesy of R. Talbot.

C.2 Circuit board filter

The PCB mount was designed to be modular so that a variety of filters can easily be inserted at base temperature between the sample and wiring. As displayed in Fig. C.2, in its current form as a low-pass RC filter, every track includes a surface-mounted series chip resistor and chip capacitor in parallel with the fridge itself (which is grounded). The models were chosen due to their (supposed) stability in temperature [80] and dimensions appropriate for the board. The values were chosen to reach a cutoff frequency $1/RC \sim 2$ kHz. The transfer characteristics at base temperature of a pair of wires shorted at the sample header are displayed in Fig. C.3.

The resistor is of value 2.2 kΩ and of manufacturing number CRES-2201-1206-1/4W. At base temperature, however, the resistance of a pair of wires shorted at the sample header was found to be ≈ 18 kΩ, *i.e.* with $\sim 400\%$ increase compared to room temperature value.

The capacitor's manufacturing number is C4532NP01H224J320KA and has 220 nF capacitance at room temperature. From the 130 Hz -3 dB rolloff frequency of Fig. C.3, we can estimate from $f \approx 1/RC$ with $R \approx 18$ kΩ that the capacitance at base temperature of the pair of capacitors in parallel is 430 nF. This suggests that the capacitance of individual capacitors remains quite stable between room and base temperature.

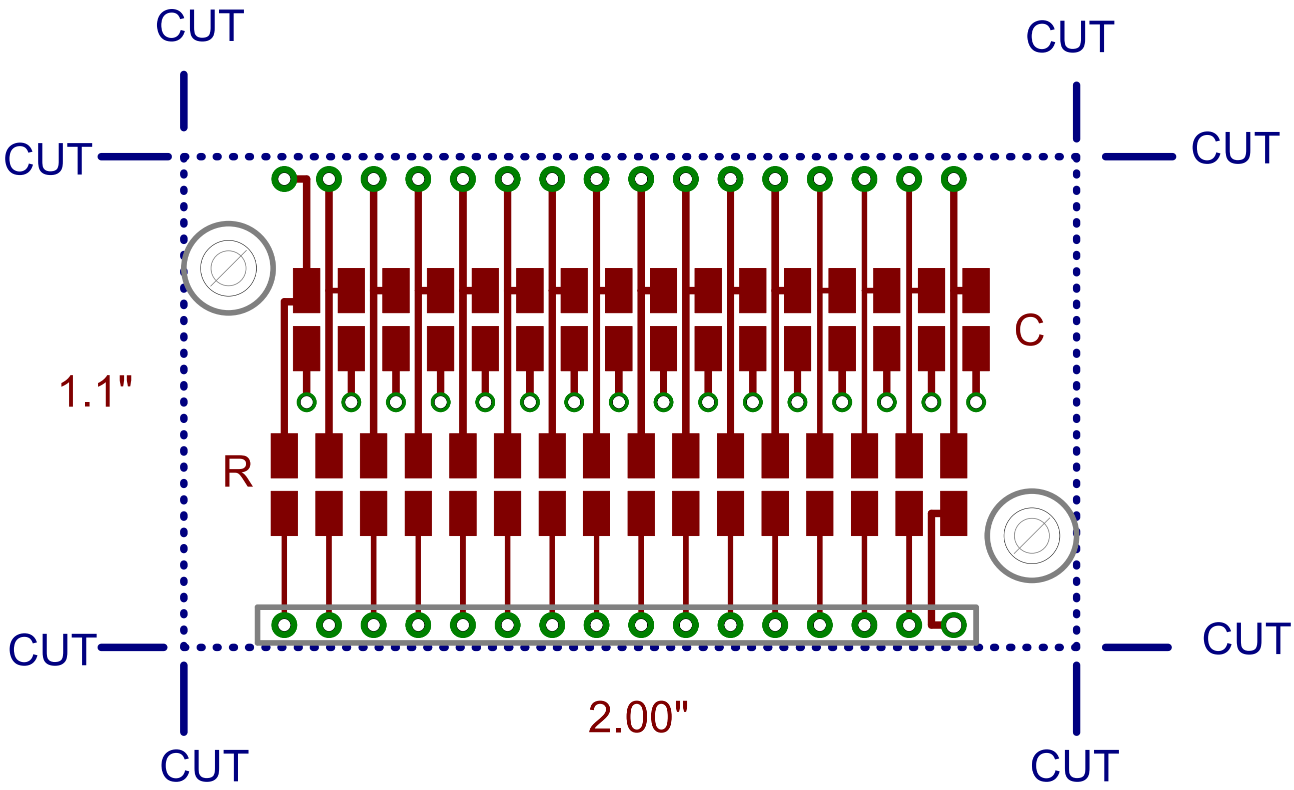

Figure C.2: Current low-pass RC printed circuit board design. The 2”x1.1” board has male DIP connectors fixed to the top and bottom rows of holes to contact the conducting tracks. Contact pads host chip resistors in series with the tracks (R) or chip capacitors in parallel with the tracks (C). Grounding is provided by vias contacting the backside of the board (center row of holes). The board can be screwed onto the silver powder filter with M2 screws (side holes). EAGLE schematic courtesy of R. Talbot.

C.2.1 Possible improvements

1. The commercial “prototype” G10 PCB should be replaced with a handcrafted one optimized for ultralow temperature operation, as was done for instance in [81].

   (a) The substrate should be made thinner and replaced by a better low temperature heat conductor, for instance sapphire or a pure metal with a thin dielectric layer.

   (b) The lead/tin conducting tracks should be replaced by pure metal such as gold-plated copper.

   (c) The components should be surface-mounted with silver paste or epoxy.

2. Chip resistances with less temperature dependence should be used.

3. In addition, finding non-pretinned components or sanding away the solder prior to mounting would improve component thermalization.

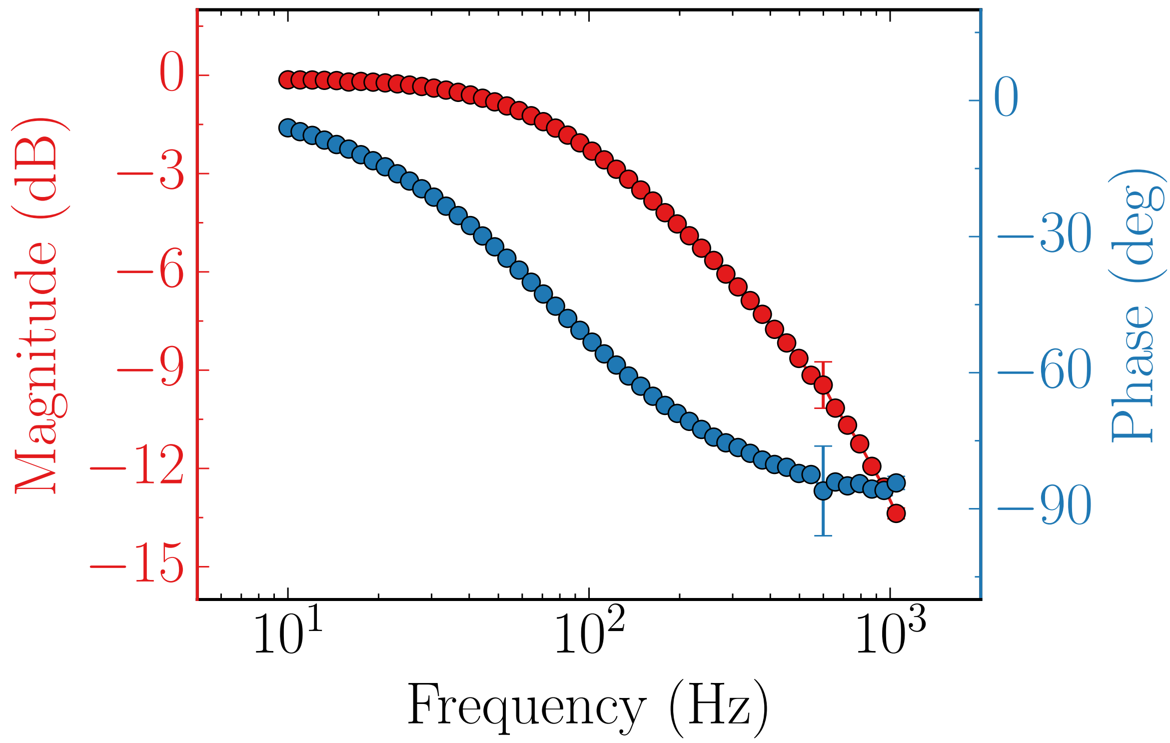

Figure C.3: Transfer characteristics of two shorted pins at the sample stage. Red is the amplitude and blue the phase. The error bars are from the statistical error on repeated measurements. The increased error at ≈ 600 Hz is likely due to this frequency being a harmonic of the mains. The standard cutoff, defined as the frequency with 3 dB attenuation, corresponds to ≈ 130 Hz.

C.3 Silver powder filters

A final round of thermalization is performed just before the wires are sent to the sample. This is achieved by running the 0.0253" enamel-coated silver wires through silver powder encased in a OFHC copper container. The container's base is first lined with silver powder. The wires are then twisted pairwise and run across the side slots through the container. More silver powder is poured over the wires until they are well encased; the powder is pressed down with a manual press to ensure proper coating, with care being put not to damage the dielectric casing of the wires. A cap then is screwed to seal the wires and powder inside the container. Finally, the side slots are epoxied from the outside to prevent powder from leaking out. Figs. C.4-5 display the relevant schematics.

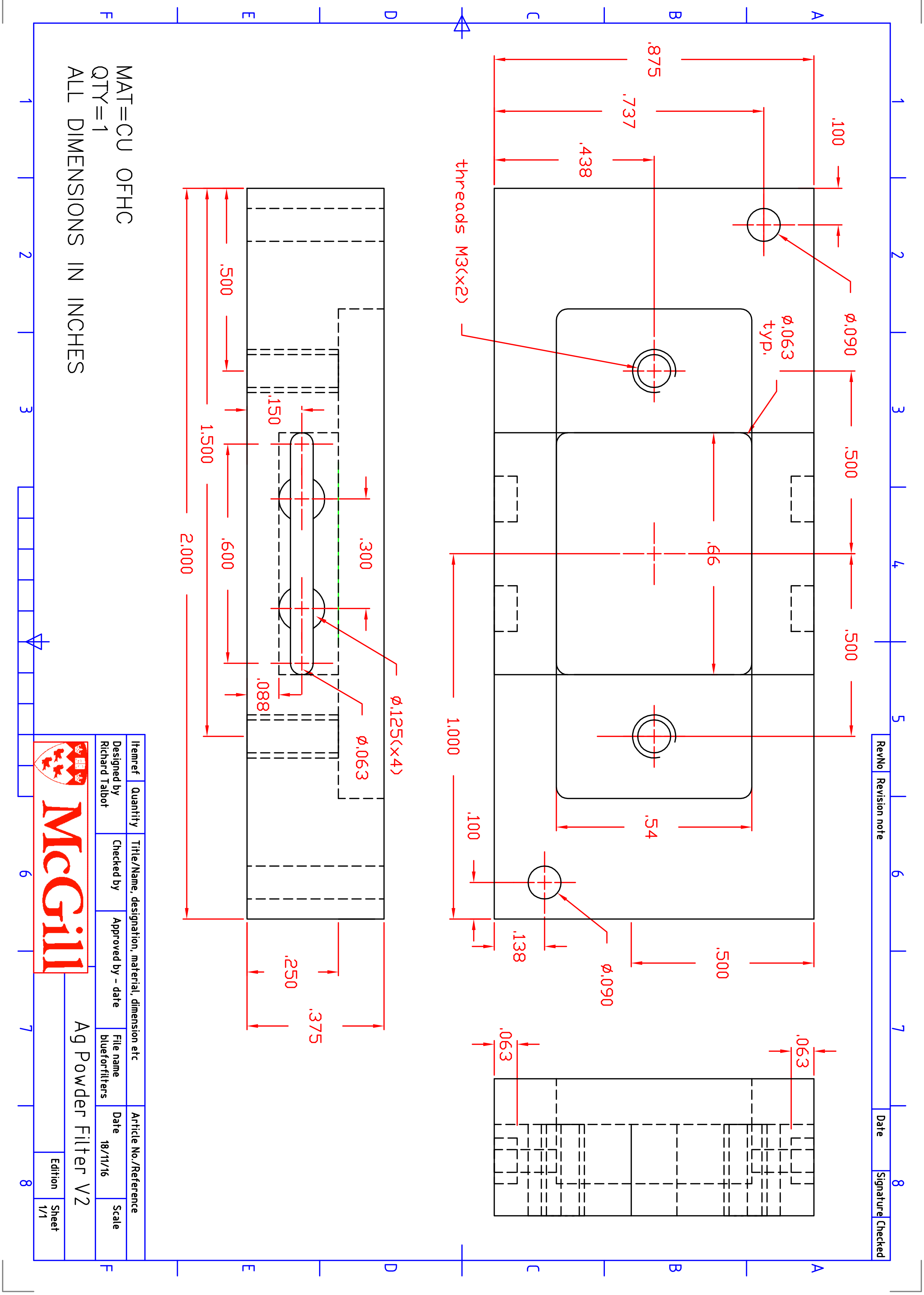

Figure C.4: Silver powder filter container schematic. CAD drawing courtesy of R. Talbot.

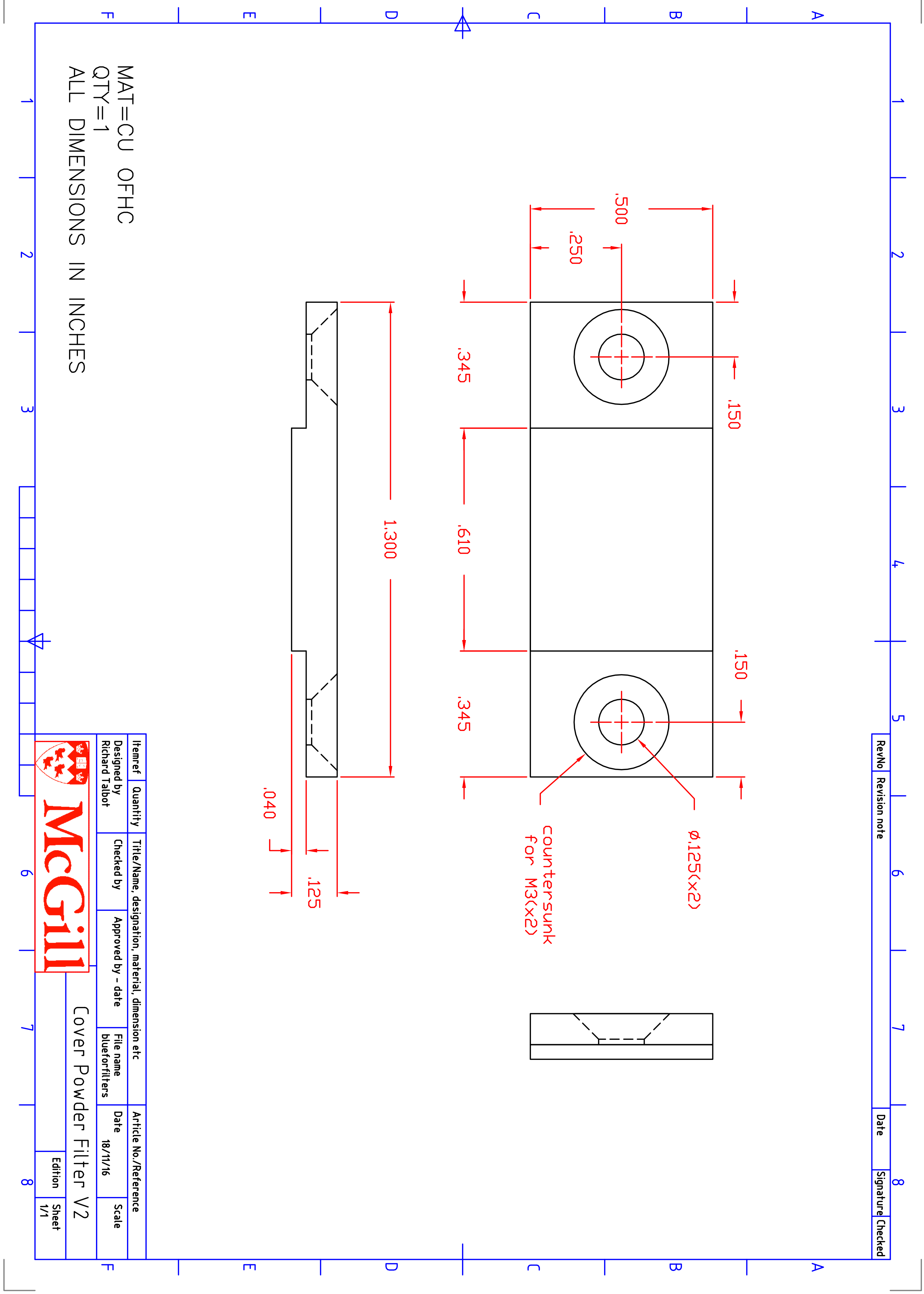

Figure C.5: Silver powder cover schematic. CAD drawing courtesy of R. Talbot.

Appendix D

Redundant Device B characterization

Device B's preliminary characterization and successful drag tests, performed similarly as for Device A as reported in Secs. 4.1 and 4.2, are displayed in this section.

D.1 Preliminary characterization

D.1.1 Pinch-off gate sweeps

As for Device A, the pinch-off gates are not hysteretic and two electron layers seem present, as displayed in Fig. D.1.

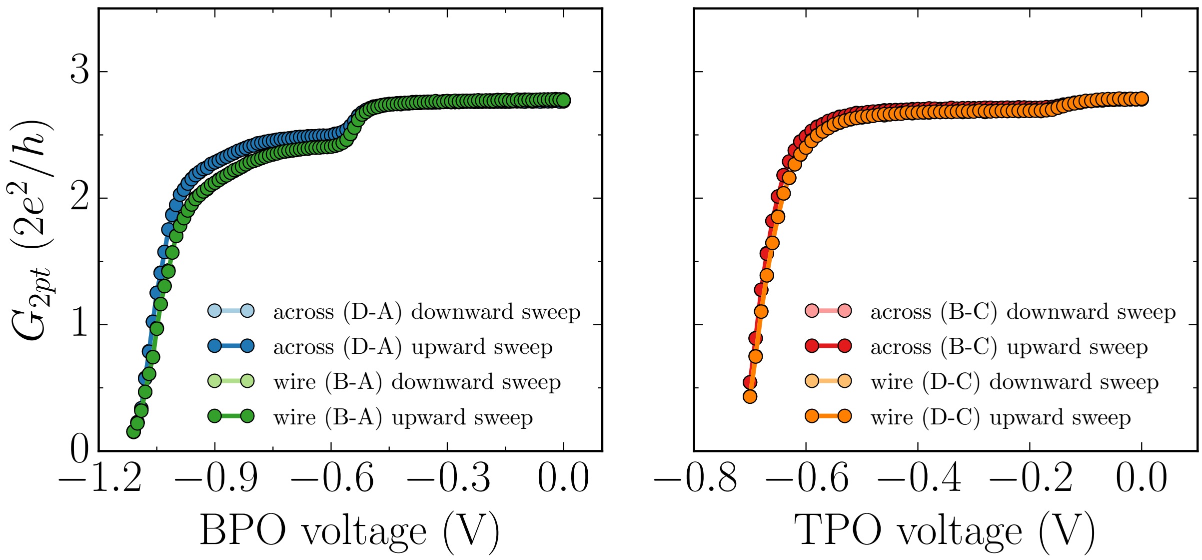

Figure D.1: Pinch-off curves for Device B with no bias on the gates or illumination during cooldown. Data taken in the McGill wet refrigerator.

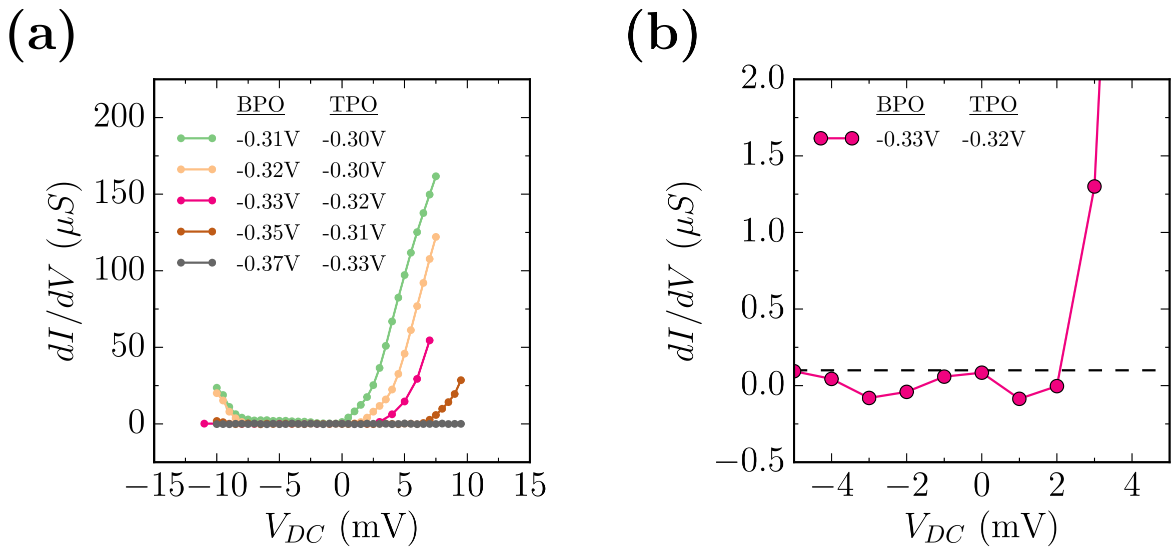

Figure D.2: Tunneling characterization of Device B using circuit from Fig 3.3b. Data taken in the McGill wet refrigerator. (a) Full range of the sweep. (b) Zoom on the $< 0.1\mu$S (or > 10MΩ) region where a suitable configurations can be identified.

.

D.1.2 Pinch-off gate optimization

For Device B, the circuit of Fig. 3.3b was used to directly obtain the tunneling conductance. The data are presented in Fig. D.2. For BPO set below -0.61 V and TPO set below -0.30 V, a tunneling resistance larger than 10 MΩ is obtained for $\pm$ 1 mV bias.

D.2 Drag tests

D.2.1 Linearity of drag voltage with drag current

Repeated sweeps at different drive currents, as well as voltage/current relationships at fixed BPL gate voltages, are presented in Fig. D.3 for Device B. Here, due to more significant noise, the drag voltages at given gate voltage configurations were not extracted from the sweeps. The wires were instead set to a specific configuration and data a single $V_{drag}(I_{drive})$ point was obtained with longer averaging. The current was then increased to obtain the next point. The drag appears to be linear up to the maximal current input explored of 4 nA. Since the cooling scheme was not optimized, it is likely that the electron temperature was saturated at some higher temperature than the fridge base temperature, rendering the system less sensitive to

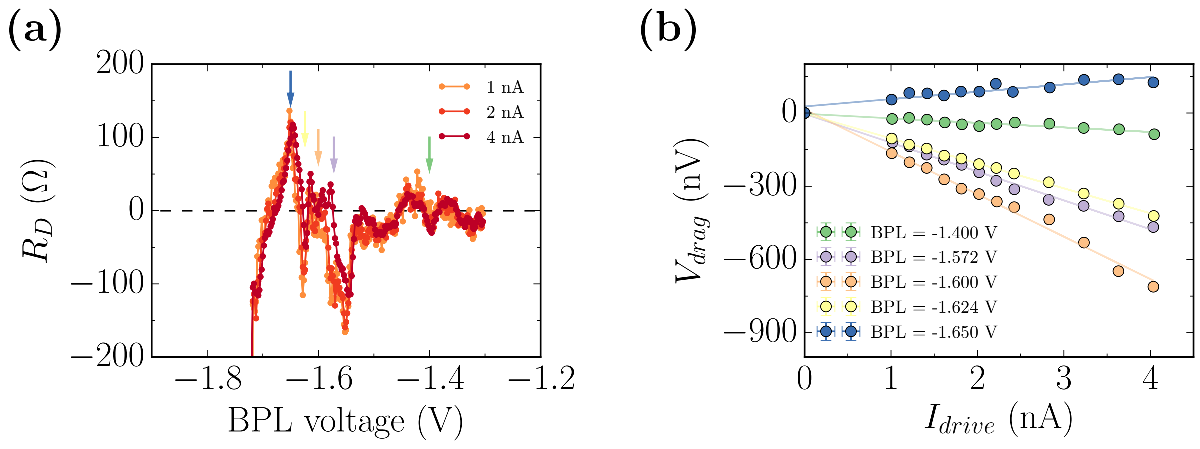

Figure D.3: Drag linearity of Device B. (a) repeated Coulomb drag sweep at different drive currents in Device B. Unsmoothed data taken in the McGill dry refrigerator with a 13 Hz excitation frequency. (b) Linearity of drag signal in Device B at fixed gate voltages. These specfic $V(I)$ data were acquired with a 7 Hz excitation frequency and at a different time as the sweeps displayed, which explains discrepancies with the left plot. However, similar linear behaviour is observed at all explored frequencies.

.

Joule dissipation. Going to higher drive currents or studying the temperature dependence of the drag signal could allow this to be studied more systematically.

D.2.2 Probe symmetry

For Device B, the features appear to be quantitatively reproduced in all regimes as presented in Fig. D.4. Furthermore, this was the case whichever sets of contacts were chosen during the experiment (two were available for each of positions A, B ,C, and D), and also for reversal of only the voltage probes while accounting for the change in sign of drag resistance in that case. One important caveat is that the measurement only reaches up to two subbands occupied. Investigating the full range would provide stronger evidence of this symmetry being satisfied.

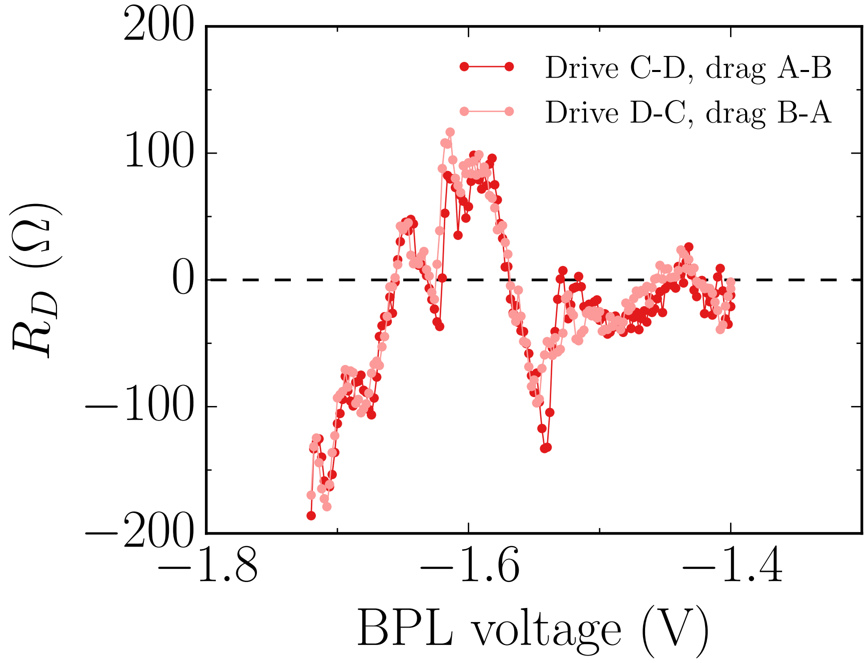

Figure D.4: Probe symmetry of drag signals in Device B. Unsmoothed data taken in the McGill dry refrigerator.

.

Appendix E

1D-1D Thermoelectricity Platform

Recently, the thermoelectric properties of multi-terminal Coulomb-coupled conductors have become of interest. This is due to the fact that in these systems, in opposition to typical single conductors, heat and charge flows can be decoupled. This could circumvent one of the pervasive issues in the development of materials with high thermoelectric figures-of-merit. The vertically-integrated quantum wires presented in this thesis exhibit voltage couplings up to 25%, and so these effects are most certainly non negligible.

For similar heat-charge decoupling reasons, Luttinger liquids themselves have long been thought to exhibit interesting thermoelectric properties. The coupled wires we present seem to display an effective interaction parameter $0.06 < K_\rho^- < 0.18$. This means they should lie in the strongly-interacting regime where these effects are expected to be apparent.

Two situations can be envisioned for thermoelectric experiments in our coupled systems. In close analogy to Coulomb drag, a charge or heat flow imposed in one system could lead to charge or heat motion in the other if the reservoirs about the systems are allowed to develop distinct local temperatures *i.e.* accounting for the presence of "parallel" thermal gradients. Alternatively, one of the two subsystems could be at a different temperature than the other. Such a "perpendicular" thermal gradient could give rise to nonlinear or ratchet effects.

E.1 Parallel thermal gradients : thermoelectric drag

As explored in the main chapters of this thesis, 1D-1D Coulomb drag offers the opportunity to perform transport experiments involving Luttinger liquids with minimal influence from Fermi liquid leads. Transport, however, is not limited to charge. If the local temperatures of the equilibrium distributions of the leads about a conductor are allowed to differ, leading to a temperature difference ΔT in the steady-state, then a heat current I_Q can appear in the conductor. This gives rise to new linear response coefficients. A phenomenological formulation of this situation is given by the thermoelectric matrix,

$$\begin{pmatrix} \Delta V \\ I_Q \end{pmatrix} = \begin{pmatrix} R & S \\ \Pi & K \end{pmatrix} \begin{pmatrix} I \\ \Delta T \end{pmatrix}, \tag{E.1}$$

where R is the electrical resistance[1], but it is now accompanied by the extensive Seebeck coefficient (or thermopower) S[2], the Peltier coefficient Π[3], and the thermal conductance K[4]. Note that here, we are only considering heat flows, temperature gradients, and thermoelectric coefficients for the electron system. Including electron-phonon coupling and its associated energy transfer will complicate the problem, although not impossibly so in the temperature regimes considered as will be discussed below.

Coulomb drag between identical systems can also be cast in a matrix form,

$$\begin{pmatrix} \Delta V_1 \\ \Delta V_2 \end{pmatrix} = \begin{pmatrix} R_1 & R_D \\ R_D & R_2 \end{pmatrix} \begin{pmatrix} I_1 \\ I_2 \end{pmatrix}, \tag{E.2}$$

where 1 and 2 are indices for the two systems and R_D is the interwire "drag" resistance. Note that here and everywhere else, factors of -1 due to geometry have been absorbed in the coefficients for ease of reading.

While energy-related effects have been invoked to explain some interlayer transport features *e.g.* in [82–84], the scientific community has barely acknowledged formally the quasi-equilibrium problem of combining equations E.1 and E.2. This is characterized by

$$\begin{pmatrix} \Delta V_1 \\ I_{Q1} \\ \Delta V_2 \\ I_{Q2} \end{pmatrix} = \begin{pmatrix} R_1 & S_1 & R_D & S_D \\ \Pi_1 & K_1 & \Pi_D & K_D \\ R_D & S_D & R_2 & S_2 \\ \Pi_D & K_D & \Pi_2 & K_2 \end{pmatrix} \begin{pmatrix} I_1 \\ \Delta T_1 \\ I_2 \\ \Delta T_2 \end{pmatrix}, \tag{E.3}$$

where R_i, S_i, Π_i, and K_i ($i = 1, 2$) are the single wire thermoelectric coefficients and R_D, S_D, Π_D, and K_D are their interwire counterparts that allow for the development of heat flows or gradients in one system due to transport processes occuring in the other. Indeed, the

[1] Which we recall is related by a geometric factor to an intensive resistivity ρ or conductivity $\sigma \equiv 1/\rho$ with the full conductance $G \equiv R^{-1}$.

[2] Whose related intensive quantity α is also referred to as Seebeck coefficient or thermopower.

[3] Whose intensive analogue is typically also expressed as a function of α.

[4] Characterized by the intensive thermal conductivity κ.

only mention of this possibility is a Boltzmann transport equation-based calculation of the interlayer Seebeck coefficient α_D between two 2D electron gases by a group from Clemson University [85, 86]. This lack of interest may be due to the weakness of both low-temperature drag and low-temperature thermal conductivity in 2D systems, the typical platform for drag. For strongly-coupled Luttinger liquids with important repulsive interactions, as our vertically-coupled quantum wires are believed to be with interwire voltage couplings up to 25% and a net interlayer interaction parameter $0.06 < K_\rho^- < 0.18$, the consequences could be drastically different and worth investigating, both theoretically and experimentally.

E.1.1 Thermoelectric transport theory

A suitable summary of conventional thermoelectric transport can be found in [87]. Upon assumption of independent particles carrying both charge and heat and for excitations close to the Fermi level (as in Fermi liquid theory for typical degenerate metals[5]), robust systematic relationships between charge and heat flows are found. These are captured by the following relations (where e is electron charge, T the absolute average temperature of the conductor, and $L_0 \equiv \frac{\pi^2}{3}\left(\frac{k_B}{e}\right)^2 \approx 2.44 \times 10^{-8}$ WΩK^{-2} is the noninteracting Lorenz number) :

- The Mott relation relates S and G (or α and σ) as

$$S = eL_0T\left(\frac{d\ln G(\epsilon)}{d\epsilon}\right)_{\epsilon=\mu}. \tag{E.4}$$

- In the presence of time-reversal symmetry, the Onsager relations impose proportionality in the cross-coefficients,

$$\Pi = TS. \tag{E.5}$$

- The Wiedemann-Franz Law relates K and G (or κ and σ) and is given by

$$\frac{K}{G} = L_0T. \tag{E.6}$$

Once the assumption of independent carriers is relaxed, it becomes possible for heat and charge to propagate independently. This is what is expected to occur in strongly-correlated 1D

[5] More general relationships exist to find different expressions if the carriers are noninteracting but away from the Fermi level *e.g.* in nondegenerate semiconductors.

repulsive systems such as infinite electronic Luttinger liquids. Even spinless repulsive Luttinger liquids are expected to exhibit this characteristic; this can be semiclassically pictured by considering that, in a charge density wave-dominated regime, transporting a unit of charge from one terminal of the electron chain to the other requires sliding the entire chain, whereas energy can be transported across the chain by propagation of arbitrarily small density wavepackets with no net chain displacement. When independent density waves of spin are added, this effect is exacerbated, since these can exclusively carry energy [88]. Also, beyond Luttinger liquid behaviour, purely mesoscopic effects may come into play that will affect the coefficients [89]. This should have as a consequence the breakdown of many of the relations enunciated above.

Indeed, various quantitative calculations of the single-system coefficients in infinite or contacted Luttinger liquids with and without impurities have been performed, *e.g.* in [50, 90–93]. These calculations do report some Luttinger liquid interaction parameter-dependent deviations from Fermi liquid expectations for infinite Luttinger liquids, and a more complicated situation for contacted 1D wires. Experimentally, however, the thermoelectric coefficients of 1D systems have always been found to obey the Fermi liquid reciprocity relations[6], see for instance [95–97] for quantum point contacts or quantum wires in GaAs 2DEGs. This is possibly for the same reason that interaction-induced electrical conductance renormalization is usually not observed in single wires.

When considering *coupled* Luttinger liquids employing the mechanisms described in Sec. 2.3.1, it is currently unclear what form the various interwire coefficients S_D, Π_D, or K_D would take. Until this is formally explored as was done in [85, 86] for 2D-2D systems, the null hypothesis could start with the calculated or measured effective currents or voltages imposed (developed) in the drive (drag) wire as a result of the action of I_{drive} and R_D, which are known. These could be combined with the purely intrawire thermoelectric coefficients S_i, Π_i, and K_i, either in the Fermi-liquid or Luttinger liquid pictures, to yield the expected ΔT's and I_Q's that would appear about each wire, completing the matrix of Eq. E.3. Measured deviations from the Fermi-liquid expectations could be ascribed to strongly-correlated electronic behaviour. Before all this however, it would be wise to evaluate if temperature gradients and/or heat currents could be generated or measured in GaAs/AlGaAs 2DEGs, or if the thermoelectric coefficients could directly be inferred from other measurements. If any of these prove applicable, knowing under what constraints or limitations would then be vital.

[6] Some experiments in "striped" materials report deviations [94], but evidences in well-controlled 1D systems such as GaAs/AlGaAs split-gate quantum wires are still lacking.

E.1.2 Thermoelectric experiments in nanoscale systems

Thermoelectric characterization in “bulk” nanoscale systems

The thermoelectric properties of mesoscale or nanoscale systems in general have been of interest for the last few decades, again mostly for heat-charge decoupling reasons *e.g.* see [98–101]. A complete overview is however outside the scope of this preliminary review. Rather, we shall focus on some characterization methods that were designed for somewhat related systems such as field-effect transistors, carbon nanotubes, and semiconductor nanowires[7].

The orthodox approach to thermoelectric characterization is to use bulk heaters and thermometers in contact with the sample to establish and measure temperature gradients. These measurements are then subsequently linked to the desired coefficients *via* Eq. E.1. Note that a heat equation model usually needs to be posited to relate steady-state heat-transport induced temperature rises to I_Q. When these approaches have not directly been used[8], all-electrical techniques have also been employed. These include “noise thermometry [103], gate electrode electrical resistance thermometry [104, 105], pulsed voltage measurements [106, 107], or an AC conductance method [108–111]” as outlined in [99]. The thermal conductance of nanotubes has similarly been all-electrically characterized using self-heating combined with modeling [112] or “breakdown thermometry” [113, 114].

To the author’s knowledge, while some of these specific all-electrical methods have been applied to gate-defined nanostructures in GaAs/AlGaAs 2DEGs at low temperatures, they have not been used to determine thermoelectric properties as above. Performing further research on these more industry-standard methods and evaluating what could be brought to our systems may still be worthwhile. For the rest of this review, our focus is set on existing methods in the literature combining thermoelectric coefficient extraction and 2DEGs in semiconductor quantum wells. Two principal approaches have been identified in the literature to infer thermoelectric coefficients in 2DEGs : heat balance and local thermometry.

Thermoelectric characterization in 2DEGs

Heat balance methods typically dissipate power in a section of the 2DEG; in the steady-state, this is related to the outgoing heat flows, for instance I_Q of the structure to be probed.

[7]For instance, the low temperature mesoscopic thermoelectric effects explored in [101] are less geared towards the goal of characterizing structures and more towards new chip designs in their own right.

[8]For a single example out of many, [102] applied the technique to single suspended silicon nanowires; [98, 99] cite many similar studies.

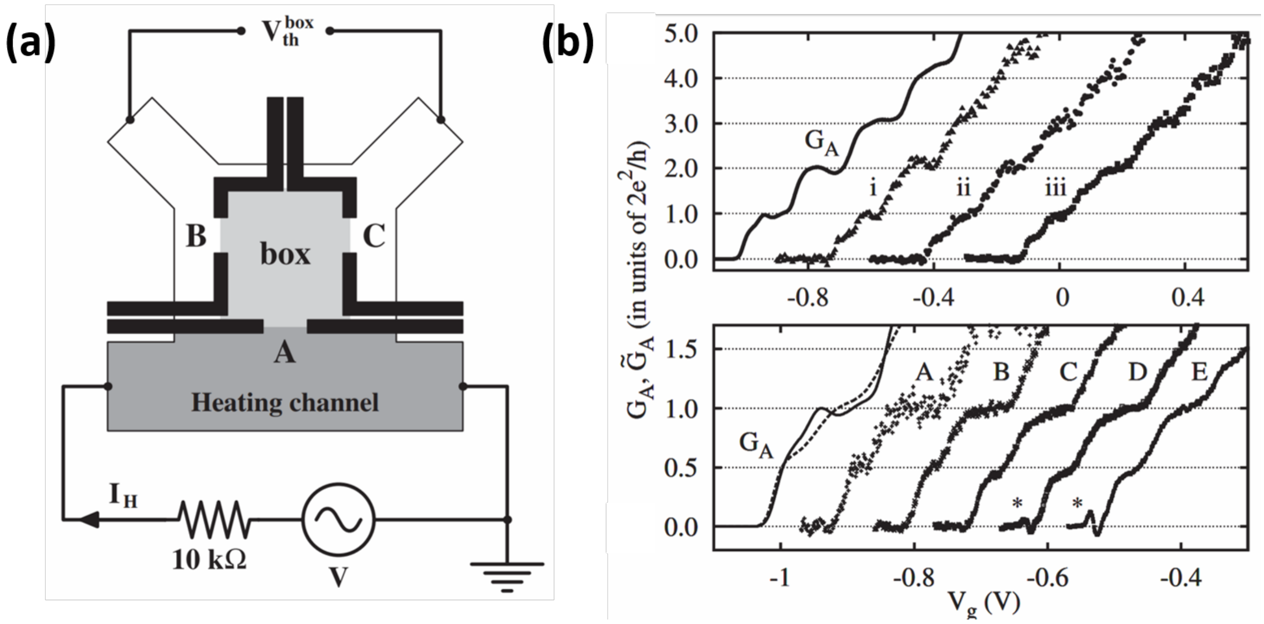

Figure E.1: Example of heat balance approach to the extraction of the thermal conductance of a ballistic quantum wire from Chiatti *et al.* [97]. (a) Experimental design. The thermal conductance of the ballistic quantum wire defined by constriction A is sought. Electrons in the heating channel thermalize to a temperature T_H due to a heating current I_H. They subsequently move into the box through constriction A, yielding an increased local temperature $T_{box} > T_0$ that is inferred through the differential thermopower between the ohmic contacts located beyond constrictions B and C as their conductance (and therefore thermopower via Eq. E.4) is varied. (b) Comparison between the directly-measured electrical conductance of constriction A G_A and its thermally-determined electrical conductance $\tilde{G}_A$. The latter is given by $(G_B + G_C)\frac{V_{th}^{box}}{V_{th}^{H} - V_{th}^{box}}$ as determined by the heat balance argument. V_{th} are the various measured thermovoltages incurred due to I_H. The different curves correspond to different heating currents I_H. Note that the entire chip design is geared towards the extraction of K of constriction A.

The heat flows can usually be manipulated, allowing quantitative extraction of the structure properties. However, the device geometry required for such heat balance schemes must usually be tailor-made to the measurement to be performed. An example applied to a ballistic quantum wire from [97] is shown in Fig. E.1. Methods similar in spirit were used to establish the quantized conductance of fermionic, bosonic, and anyonic heat flow [115, 116]. Possible "thermal bridge" methods could also be categorized so [117]. While these techniques could be leveraged to obtain the desired data precisely, they may require significant redesign of the coupled parts of the current drag devices which are already the fruit of years of development and optimization. As such, they will be set aside at this point in time.

Local thermometry methods, on the other hand, are commensurate to the conceptually simple heater and thermometer techniques. In 2DEGs, these are carried out with "heaters" and "thermometers" that couple directly to the electron gas or, better, a well-characterized

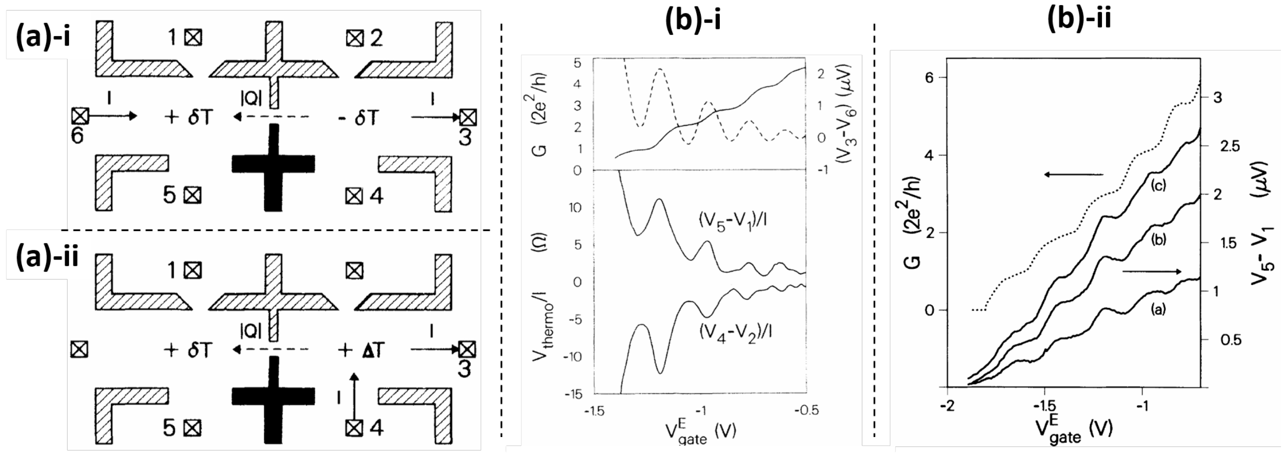

Figure E.2: Example of local thermometry approach to extracting the Peltier coefficient Π and thermal conductance K of a QPC from Molenkamp *et al.* [96]. (a) Experimental design. A structure to be probed (here, a QPC) is defined in the center of the chip and surrounded by electron thermometers (here, perpendicular quantum point contacts). (b) The various thermoelectric coefficients can then be roughly extracted by monitoring the local temperature increase or decrease δT about each terminal of the stucture probed under different constraints (here, via the thermovoltages $V_5 - V_1$ or $V_4 - V_2$ developed across the side QPCs). For this experiment, these constraints would be an electrical current run through the center device to extract Π for (i) or one terminal being Joule heated by a local current to $\Delta T >> \delta T$ for K in (ii). While the approach is less precise than heat balance, it is agnostic to the details of the structure probed : the middling QPC whose properties are desired could in principle be replaced by any other element. The method is also flexible, allowing extraction of S, Π and K with the same platform.

nanostructure embedded therein. One may think of the secondary thermometry method exploiting the differential thermopower of asymmetrically-biased gate-defined QPCs [96], etched constriction QPCs [118], or bar gates [119, 120]; as well as local noise thermometry [121, 122]. Noise thermometry across a QPC (instead of the bare 2DEG) has also been used as a primary thermometer with heightened sensitivity [115, 116, 123]. Another primary local thermometry method that has been used in 2DEGs is the energy-filtering property of single gate-defined quantum dot [124]. While this has not been directly used to infer thermoelectric coefficients in the suggested local thermometry scheme, it has been successfully employed as an electron spectrometer to measure nonequilibrium distributions in quantum hall edge states as a probe of heat transport *e.g.* see [125, 126]. Most of these methods can also be calibrated under an applied magnetic field, which would be requisite to explore spin-charge separation effects on thermal transport. If this local thermometry route with minimal adjustments to the current 1D-1D coupled area is to be taken, we now need to assess if the heat flows generated at the quantum wire terminals can be detected further away in the contacting areas.

E.1.3 Suggested modifications to existing device design

To estimate the possibilitys of carrying out parallel thermal drag experiments, a finite-element ultralow-temperature heat equation solver was developed by Thulstrup *et al.* [127] based on open-source technology [128]. The software solution leverages various tools to define adaptative 2D meshes of arbitrary shape and numerically solve on them any partial differential equations. If well-calibrated, this software could also be used as the heat equation model to relate measured temperature increases in the contacting areas to I_Q in the wire area.

In the ultralow temperature charge-density wave locking regime where the Luttinger liquid should be most manifest in the drag, the Fermi liquid electron system characterizing the 2DEG away from the quantum wires is weakly-coupled, but not completely isolated, from the phonon bath assumed to be uniformly held at the fridge base temperature [129, 130]. In addition, considering locally elevated electron temperatures in the 2DEG requires accounting for local Joule dissipation which can be leveraged to generate temperature gradients. This leads to a steady-state 2D heat equation for electrons in the 2DEG including the contributions of electron diffusion, Joule dissipation and, equilibration to the phonon bath,

$$-\frac{L_0}{2\rho}\nabla^2 T(x,y)^2 = \frac{(\nabla V(x,y))^2}{\rho} - \alpha\left(T(x,y)^p - T_0^p\right). \tag{E.7}$$

The parameters α and p depend on the type of electron-phonon interaction.

As a proof-of-concept and for the sake of numerical viability, these parameters were first calibrated against data taken from a heat propagation experiment in a similar high mobility GaAs/AlGaAs 2DEG as used for the Coulomb drag devices [131]. This is presented in Fig. E.3. The experiment in question was carried out at a higher base temperature than desired for possible drag experiments : as such, it offers at the very least a “lower bound” for estimates of heat propagation. Using this calibrated version of Eq. E.7 on a mesh corresponding to our devices’ contact area geometry can then guide design decisions.

Important insights confirming expectations were gained, see [127]. Temperature imbalances with respect to the base temperature decay over a distance of $\sim 200\mu$m, even for unrealistically high heat sourcing. Therefore, local heating currents and thermometers should be placed as close as possible to the wire terminals, leading to “L” shaped contact area with the ohmic contacts located at the ends of the “L”. The arms of the “L” should be long enough for the temperature imbalance generated to be maximal, meaning completely dominated by

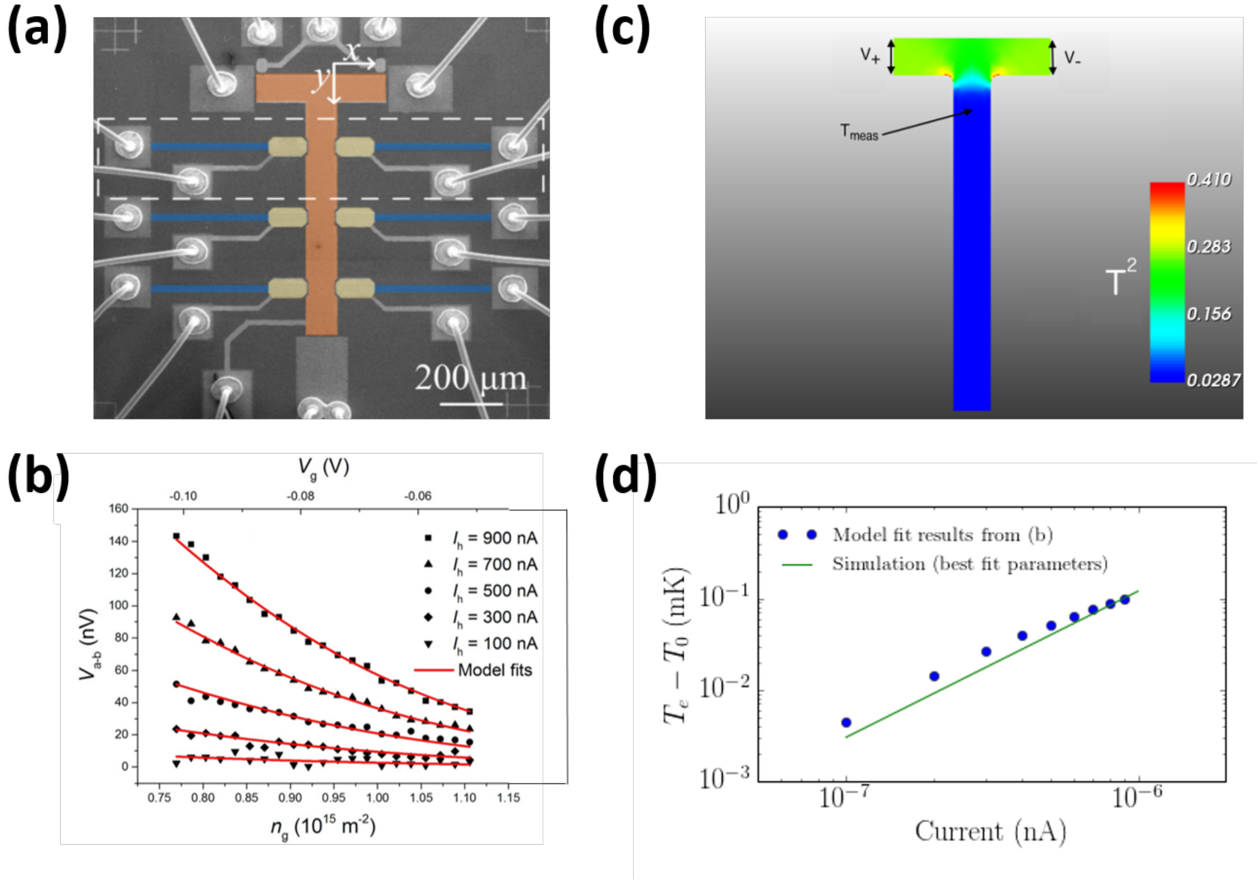

Figure E.3: Calibration of the numerical solver to heat propagation data in a high-mobility 2DEG as reported in Billiald *et al.* [131]. (a) Micrograph of the experiment. A current I_h is run between the two top contacts of the "T", dissipating heat in the 2DEG. The bottom contact is thermally anchored to the mixing chamber, leading to electronic heat diffusion from the top to the bottom of the "T". The local temperature increase along the "T" can be measured at different locations through the differential thermopower about asymmetrically-biased bar gates (middling structures). Figure from [131]. (b) Bar gating-dependent thermovoltage about the first bar gate thermometer for different I_h. The only variable in the model is the electron temperature in the middle "T" part of the device between the bar gates some distance from the heating element, allowing the fit to retrieve it. Figure from [131]. (c) Example of numerical simulation of the experiment of (a). A current $I_h = \Delta V / R_h$ (with R_h as reported in [131]) is imposed at the boundaries of the top part of the "T", and the simulator computes the local temperature along the entire mesh using Eq. E.7 and T_0 (again from reported in [131]) temperature boundary conditions wherever an ohmic contact is present in the device. Figure from [127]. (d) The increase of electronic temperature where the bar gate thermometer would measure it in (a) is plotted against the I_h. The green line shows the simulated temperature increase for the best fit parameters and the blue dots the measured temperature increase as reported in (b). The simulator seems able to capture electronic heat propagation in this regime.

relaxation to the lattice without contribution from diffusion to the contacts. For the simulations performed, the transition between the two regimes occurs approximately at 400 μm of arm length.

In spite of the open questions remaining in the quantitative prediction of the temperature imbalances to be measured, we note that moving to such a "L"-shaped contact geometry would *immediately* allow experiments to measure S_D, since the latter only requires imposition of a temperature gradient and not detection of the temperature imbalances. The temperature gradient could be varied by changing the current flow between the two ohmic contacts in the same contacting area, with the "L" shape ensuring that energy dissipation occurs close enough to the quantum wire and locally heat one drive wire terminal above lattice temperature. The drag voltage can then be measured at the second harmonic of the heating voltage in the drag layer. The second harmonic (or DC) is required since $\Delta T \propto P \propto I^2$,with $I(t)^2 = I_0^2 \cos^2 \omega t = \frac{I_0}{2} + \frac{I_0}{2} \cos 2\omega t$ for an AC current. More importantly, this geometry should not jeopardize the ability to perform the regular drag experiments, limiting risk. Furthermore, a thermometer, say a quantum dot with appropriate extra ohmic contacts and counter "pinch-off" gates, could be introduced in the "L" of the drag layer during the same fabrication processes already used for the coupled quantum wires, adding no complexity to the fabrication. It might then be able to detect heat currents, but even if it does not, regular drag experiments could be performed in the device.

E.2 Perpendicular thermal gradients : heat-to-charge rectification

A large body of literature have discussed recently multi-terminal energy harvesters, see [132] for a review. While the specific implementation of these various proposals differ in details, the overarching idea remains the same : a "hot" subsystem with local temperature T_H is addressed by at least a single lead and coupled to a distinct "cold" subsystem with a local temperature T_C that is asymetrically contacted to at least two leads. The two subsystems and couplings can take many forms, but the general operating idea is that quanta in the cold subsystem gain excess energy provided from the hot subsystem via the coupling, and eventually exit the cold subsystem. For significant energy-dependent exit rates, there is a preferred exit direction after the energy absorption and therefore rectification of the hot cavity's thermal fluctuations is achieved.

The proposal and implementation of most interest to us is when phase-incoherent electron transmission is rectified via the Coulomb interaction, as displayed in Fig. E.4. This has been observed in experiments with μm^2-sized 2DEG strips coupled by a capacitor [134], with laterally-coupled single-electron quantum dots [135], as well as with nearby chaotic quantum dots where the "heating" is provided by the controlled introduction of noise on the quantum dot gate [136]. Such rectification may occur in the drag devices. In the existing devices, however, the left-right transmission asymmetry in the cold wire is not directly controllable as opposed to the above experiments. Even without such control, however, other supplementary effects may come into play. Thermal gating [137] may affect the signal by affecting the conductance of the cold wire as a function of hot wire excess temperature. Other nonlinearities characterized by a DC or higher harmonic response may also appear. These could be due, for instance, to the strong temperature dependence of the drag signal if *both* electronic systems somehow reach a higher effective temperature instead of only a single wire as is supposed in these studies.

In any case, such physics may be immediately accessible in the existing devices through the adding of gate noise as in [136], or even by directly injecting noise in the wires (see Sec. 6.2 for a short discussion on drag noise). An all-electrical thermodynamic measurement scheme could also be leveraged. Such a scheme was used by Schmidt *et al.*, for instance, to infer the thermal conductance and specific heat in exotic fractional quantum Hall states [138]. The nonequilibrium techniques of Sec. E.1.2 could also be reevaluated for this purpose. Since the transmission asymmetry into or out of our quantum wires is not controllable, but always expected, the experiment should be repeated by inversing source and drain to highlight or rule out such effects, leaving only the abovementionned supplementary effects. In a later iteration of the experiment, extra gates about each wire or in the contact areas could be added to allow a controllable modification of left/right transmission.

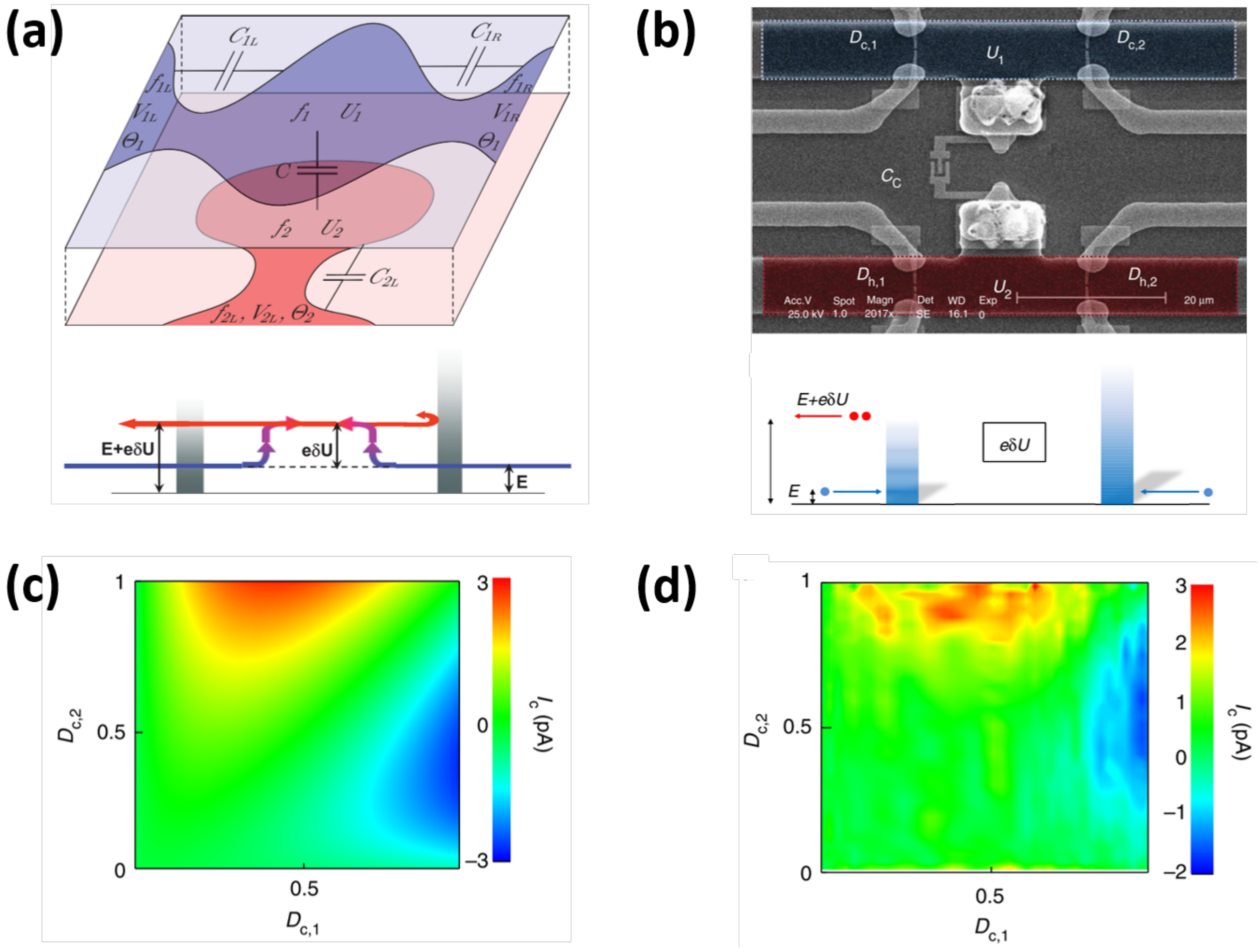

Figure E.4: Most relevant example of nanoscale multi-terminal energy harvester. (a) Top : schematic of the proposal. A "hot" cavity (red) is Coulomb-coupled to a "cold" cavity (blue). Each cavity is addressed by leads characterized by electron distributions. Bottom : schematic of the process. Electrons enter the cold cavity with energy E and move to a higher energy $E + e\delta U$ thanks to the higher fluctuating potential of the hot cavity mediated by the coupling. If left/right transmission is not symmetric, this can lead to a preferential exist direction for hot electrons in the cold cavity. Figure from [133]. (b) Experimental realization. Two 2DEG striplines (red and blue regions) are each addressed by two quantum point contacts ($D_{i,j}$) and coupled by a middling capacitor. Power is dissipated in the hot line, driving it to a temperature $T_{hot} > T_{cold}$. As the transmission of the cold line's two quantum point contacts $D_{C,j}$ is asymmetrically varied, a DC current should appear in the cold line. Figure from [134]. (c) Predicted rectification from the model in (a) applied to the realization in (b). Figure from [134]. (d) Data from (b). In this instance, the effective capacitance between the two lines is ~ 0.4 pF and $\Delta T \equiv T_{hot} - T_{cold} \approx 800$ mK. Figure from [134].

References

[1] P. W. Anderson, "More is different," *Science*, vol. 177, no. 4047, pp. 393–396, 1972.

[2] B. Narozhny and A. Levchenko, "Coulomb drag," *Reviews of Modern Physics*, vol. 88, p. 25003, May 2016.

[3] D. Laroche, *Coulomb Drag in Vertically-Integrated One-Dimensional Quantum Wires.* PhD thesis, McGill University, December 2013.

[4] D. Laroche, G. Gervais, L. P., and R. L., "Positive and negative Coulomb drag in vertically integrated one-dimensional quantum wires," *Nat Nano*, vol. 6, pp. 793–797, December 2011.

[5] D. Laroche, G. Gervais, M. P. Lilly, and J. L. Reno, "1D-1D Coulomb Drag Signature of a Luttinger Liquid," *Science*, vol. 343, pp. 631–634, December 2013.

[6] M. Born and R. Oppenheimer, "Zur quantentheorie der molekeln," *Annalen der Physik*, vol. 389, no. 20, pp. 457–484, 1927.

[7] L. Landau, "The theory of a fermi liquid," *Sov. Phys. JETP*, vol. 3, no. 6, pp. 920–925, 1957.

[8] J. M. Krans, J. M. van Ruitenbeek, V. V. Fisun, I. K. Yanson, and L. J. de Jongh, "The signature of conductance quantization in metallic point contacts," *Nature*, vol. 375, p. 767, June 1995.

[9] H. Kroemer, "Nobel lecture: Quasi-electric fields and band offsets: Teaching electrons new tricks." December 2000.

[10] T. Szkopek, "Lecture notes for ecse 535 : Nanoelectronic devices." January 2015.

[11] I. Tan, G. L. Snider, L. D. Chang, and E. L. Hu, "A self-consistent solution of schrödinger–poisson equations using a nonuniform mesh," *Journal of Applied Physics*, vol. 68, no. 8, pp. 4071–4076, 1990.

[12] D. G. Schlom and L. N. Pfeiffer, "Upward mobility rocks!," *Nature Materials*, vol. 9, p. 881, October 2010.

[13] H. Störmer, "Electron mobilities in modulation-doped gaas-(alga)as heterostructures," *Surface Science*, vol. 132, no. 1, pp. 519 – 526, 1983.

[14] B. J. van Wees, H. van Houten, C. W. J. Beenakker, J. G. Williamson, L. P. Kouwenhoven, D. van der Marel, and C. T. Foxon, "Quantized conductance of point contacts in a two-dimensional electron gas," *Phys. Rev. Lett.*, vol. 60, pp. 848–850, February 1988.

[15] D. A. Wharam, T. J. Thornton, R. Newbury, M. Pepper, H. Ahmed, J. E. F. Frost, D. G. Hasko, D. C. Peacock, D. A. Ritchie, and G. A. C. Jones, "One-dimensional transport and the quantisation of the ballistic resistance," *Journal of Physics C: Solid State Physics*, vol. 21, no. 8, p. L209, 1988.

[16] S. Datta, *Electronic Transport in Mesoscopic Systems.* Cambridge Studies in Semiconductor Physics, Cambridge University Press, 1997.

[17] T. Giamarchi, *Quantum Physics in One Dimension.* International Series of Monographs on Physics, Clarendon Press, 2003.

[18] S.-i. Tomonaga, "Remarks on bloch's method of sound waves applied to many-fermion problems," *Progress of Theoretical Physics*, vol. 5, no. 4, pp. 544–569, 1950.

[19] J. M. Luttinger, "An exactly soluble model of a many-fermion system," *Journal of Mathematical Physics*, vol. 4, no. 9, pp. 1154–1162, 1963.

[20] D. C. Mattis and E. H. Lieb, "Exact solution of a many-fermion system and its associated boson field," *Journal of Mathematical Physics*, vol. 6, no. 2, pp. 304–312, 1965.

[21] F. D. M. Haldane, "'luttinger liquid theory' of one-dimensional quantum fluids. i. properties of the luttinger model and their extension to the general 1d interacting spinless fermi gas," *Journal of Physics C: Solid State Physics*, vol. 14, no. 19, p. 2585, 1981.

[22] M. P. A. Fisher and L. I. Glazman, *Transport in a One-Dimensional Luttinger Liquid*, pp. 331–373. Dordrecht: Springer Netherlands, 1997.

[23] S. Tarucha, T. Honda, and T. Saku, “Reduction of quantized conductance at low temperatures observed in 2 to 10 m-long quantum wires,” *Solid State Communications*, vol. 94, no. 6, pp. 413 – 418, 1995.

[24] M. S. Purewal, B. H. Hong, A. Ravi, B. Chandra, J. Hone, and P. Kim, “Scaling of resistance and electron mean free path of single-walled carbon nanotubes,” *Phys. Rev. Lett.*, vol. 98, p. 186808, May 2007.

[25] D. L. Maslov and M. Stone, “Landauer conductance of Luttinger liquids with leads,” *Physical Review B*, vol. 52, pp. R5539–R5542, August 1995.

[26] I. Safi and H. J. Schulz, “Transport in an inhomogeneous interacting one-dimensional system,” *Physical Review B*, vol. 52, pp. R17040–R17043, December 1995.

[27] W. Apel and T. M. Rice, “Combined effect of disorder and interaction on the conductance of a one-dimensional fermion system,” *Phys. Rev. B*, vol. 26, pp. 7063–7065, December 1982.

[28] C. L. Kane and M. P. A. Fisher, “Transmission through barriers and resonant tunneling in an interacting one-dimensional electron gas,” *Phys. Rev. B*, vol. 46, pp. 15233–15262, December 1992.

[29] Y. Oreg and A. M. Finkel’stein, “Dc Transport in Quantum Wires,” *Physical Review B*, vol. 54, no. 20, pp. R14265–R14268, 1996.

[30] H. Ishii, H. Kataura, H. Shiozawa, H. Yoshioka, H. Otsubo, Y. Takayama, T. Miyahara, S. Suzuki, Y. Achiba, M. Nakatake, T. Narimura, M. Higashiguchi, K. Shimada, H. Namatame, and M. Taniguchi, “Direct observation of Tomonaga-Luttinger-liquid state in carbon nanotubes at low temperatures,” *Nature*, vol. 426, pp. 540–544, December 2003.

[31] M. Bockrath, “Luttinger-liquid behaviour in carbon nanotubes,” *Nature*, vol. 397, pp. 598–601, 1999.

[32] J. P. Eisenstein, L. N. Pfeiffer, and K. W. West, “Field-induced resonant tunneling between parallel two-dimensional electron systems,” *Applied Physics Letters*, vol. 58, no. 14, pp. 1497–1499, 1991.

[33] O. M. Auslaender, A. Yacoby, R. de Picciotto, K. W. Baldwin, L. N. Pfeiffer, and K. W. West, "Tunneling spectroscopy of the elementary excitations in a one-dimensional wire," *Science*, vol. 295, no. 5556, pp. 825–828, 2002.

[34] Y. Tserkovnyak, B. I. Halperin, O. M. Auslaender, and A. Yacoby, "Interference and zero-bias anomaly in tunneling between luttinger-liquid wires," *Phys. Rev. B*, vol. 68, p. 125312, September 2003.

[35] O. M. Auslaender, H. Steinberg, A. Yacoby, Y. Tserkovnyak, B. I. Halperin, K. W. Baldwin, L. N. Pfeiffer, and K. W. West, "Spin-charge separation and localization in one dimension.," *Science (New York, N.Y.)*, vol. 308, pp. 88–92, April 2005.

[36] H. Steinberg, G. Barak, A. Yacoby, L. N. Pfeiffer, K. W. West, B. I. Halperin, and K. Le Hur, "Charge fractionalization in quantum wires," *Nature Physics*, vol. 4, p. 116, December 2007.

[37] Y. Jompol, C. J. B. Ford, J. P. Griffiths, I. Farrer, G. A. C. Jones, D. Anderson, D. A. Ritchie, T. W. Silk, and A. J. Schofield, "Probing Spin-Charge Separation in a Tomonaga-Luttinger Liquid," *Science*, vol. 325, pp. 597–601, July 2009.

[38] M. Moreno, C. J. B. Ford, Y. Jin, J. P. Griffiths, I. Farrer, G. A. C. Jones, D. A. Ritchie, O. Tsyplyatyev, and A. J. Schofield, "Nonlinear spectra of spinons and holons in short GaAs quantum wires," *Nature Communications*, vol. 7, p. 12784, September 2016.

[39] M. Pogrebinskii, "Mutual drag of charge carriers in the semiconductor- dielectric- semiconductor system," *Sov. Phys. Semicond.*, vol. 11, no. 4, p. 637, 1977.

[40] P. J. Price, "Hot electron effects in heterolayers," *Physica B+C*, vol. 117-118, pp. 750 – 752, 1983.

[41] V. L. G. Fenton, V. B. Pevzner, and E. W, "Coulomb drag in the ballistic electron transport regime," *Journal of Physics: Condensed Matter*, vol. 10, no. 11, p. 2551, 1998.

[42] T. J. Gramila, J. P. Eisenstein, A. H. MacDonald, L. N. Pfeiffer, and K. W. West, "Mutual friction between parallel two-dimensional electron systems," *Phys. Rev. Lett.*, vol. 66, pp. 1216–1219, March 1991.

[43] A.-P. Jauho and H. Smith, "Coulomb drag between parallel two-dimensional electron systems," *Phys. Rev. B*, vol. 47, pp. 4420–4428, February 1993.

[44] A. G. Rojo, "Electron-drag effects in coupled electron systems," *Journal of Physics: Condensed Matter*, vol. 11, no. 5, p. R31, 1999.

[45] M. I. Muradov and V. L. Gurevich, "On the temperature dependence of ballistic coulomb drag in nanowires," *Journal of Physics: Condensed Matter*, vol. 24, no. 13, p. 135304, 2012.

[46] R. Klesse and A. Stern, "Coulomb drag between quantum wires," *Physical Review B*, vol. 62, pp. 16912–16925, December 2000.

[47] A. P. Dmitriev, I. V. Gornyi, and D. G. Polyakov, "Coulomb drag between ballistic quantum wires," *Phys. Rev. B*, vol. 86, p. 245402, December 2012.

[48] A. M. Lunde, K. Flensberg, and L. I. Glazman, "Three-particle collisions in quantum wires: Corrections to thermopower and conductance," *Phys. Rev. B*, vol. 75, p. 245418, June 2007.

[49] T. Micklitz, J. Rech, and K. A. Matveev, "Transport properties of partially equilibrated quantum wires," *Phys. Rev. B*, vol. 81, p. 115313, March 2010.

[50] A. Levchenko, Z. Ristivojevic, and T. Micklitz, "Interaction-induced corrections to conductance and thermopower in quantum wires," *Phys. Rev. B*, vol. 83, p. 041303, January 2011.

[51] M.-T. Rieder, T. Micklitz, A. Levchenko, and K. A. Matveev, "Interaction-induced backscattering in short quantum wires," *Phys. Rev. B*, vol. 90, p. 165405, October 2014.

[52] M. Pustilnik, E. G. Mishchenko, L. I. Glazman, and A. V. Andreev, "Coulomb drag by small momentum transfer between quantum wires," *Phys. Rev. Lett.*, vol. 91, p. 126805, September 2003.

[53] D. N. Aristov, "Luttinger liquids with curvature: Density correlations and coulomb drag effect," *Phys. Rev. B*, vol. 76, p. 085327, August 2007.

[54] A. V. Rozhkov, "Density-density propagator for one-dimensional interacting spinless fermions with nonlinear dispersion and calculation of the coulomb drag resistivity," *Phys. Rev. B*, vol. 77, p. 125109, March 2008.

[55] R. G. Pereira and E. Sela, "Spin-charge coupling in quantum wires at zero magnetic field," *Phys. Rev. B*, vol. 82, p. 115324, September 2010.

[56] T. Fuchs, R. Klesse, and A. Stern, "Coulomb drag between quantum wires with different electron densities," *Phys. Rev. B*, vol. 71, p. 045321, January 2005.

[57] G. A. Fiete, K. Le Hur, and L. Balents, "Coulomb drag between two spin-incoherent luttinger liquids," *Phys. Rev. B*, vol. 73, p. 165104, April 2006.

[58] B. N. Narozhny and I. L. Aleiner, "Mesoscopic fluctuations of the coulomb drag," *Phys. Rev. Lett.*, vol. 84, pp. 5383–5386, June 2000.

[59] N. A. Mortensen, K. Flensberg, and A.-P. Jauho, "Coulomb drag in coherent mesoscopic systems," *Phys. Rev. Lett.*, vol. 86, pp. 1841–1844, February 2001.

[60] A. Levchenko and A. Kamenev, "Coulomb drag in quantum circuits," *Phys. Rev. Lett.*, vol. 101, p. 216806, November 2008.

[61] R. Sánchez, R. López, D. Sánchez, and M. Büttiker, "Mesoscopic coulomb drag, broken detailed balance, and fluctuation relations," *Phys. Rev. Lett.*, vol. 104, p. 076801, February 2010.

[62] M. Büttiker and R. Sánchez, "A closer look at charge drag," *Nature Nanotechnology*, vol. 6, p. 757, October 2011.

[63] M. Kellogg, J. Eisenstein, L. Pfeiffer, and K. West, "Evidence for 2kf electron–electron scattering processes in coulomb drag," *Solid State Communications*, vol. 123, no. 12, pp. 515 – 519, 2002.

[64] P. Debray, V. Zverev, O. Raichev, R. Klesse, P. Vasilopoulos, and R. S. Newrock, "Experimental studies of coulomb drag between ballistic quantum wires," *Journal of Physics: Condensed Matter*, vol. 13, no. 14, p. 3389, 2001.

[65] M. Yamamoto, M. Stopa, Y. Tokura, Y. Hirayama, and S. Tarucha, "Negative coulomb drag in a one-dimensional wire," *Science*, vol. 313, no. 5784, pp. 204–207, 2006.

[66] J. H. Davies, I. A. Larkin, and E. V. Sukhorukov, "Modeling the patterned two-dimensional electron gas: Electrostatics," *Journal of Applied Physics*, vol. 77, no. 9, pp. 4504–4512, 1995.

[67] O. E. Raichev, "Phonon-mediated drag between one-dimensional electron systems," *Phys. Rev. B*, vol. 64, p. 035324, June 2001.

[68] M. Weckwerth, J. Simmons, N. Harff, M. Sherwin, M. Blount, W. Baca, and H. Chui, "Epoxy bond and stop-etch (ebase) technique enabling backside processing of (al)gaas heterostructures," *Superlattices and Microstructures*, vol. 20, no. 4, pp. 561 – 567, 1996.

[69] W. Pan, J.-S. Xia, V. Shvarts, D. E. Adams, H. L. Stormer, D. C. Tsui, L. N. Pfeiffer, K. W. Baldwin, and K. W. West, "Exact quantization of the even-denominator fractional quantum hall state at $\nu = 5/2$ landau level filling factor," *Phys. Rev. Lett.*, vol. 83, pp. 3530–3533, October 1999.

[70] C. Dean, *A Study of the Fractional Quantum Hall Energy Gap at Half Filling*. PhD thesis, McGill University, 2008.

[71] G. Gamez and K. Muraki, "$\nu = 5/2$," *Phys. Rev. B*, vol. 88, p. 075308, August 2013.

[72] M. Pioro-Ladrière, J. H. Davies, A. R. Long, A. S. Sachrajda, L. Gaudreau, P. Zawadzki, J. Lapointe, J. Gupta, Z. Wasilewski, and S. Studenikin, "Origin of switching noise in GaAsal$_x$ga$_{1-x}$As lateral gated devices," *Phys. Rev. B*, vol. 72, p. 115331, September 2005.

[73] A. Savitzky and M. J. E. Golay, "Smoothing and differentiation of data by simplified least squares procedures.," *Analytical Chemistry*, vol. 36, no. 8, pp. 1627–1639, 1964.

[74] B. Braunecker, P. Simon, and D. Loss, "Nuclear magnetism and electron order in interacting one-dimensional conductors," *Phys. Rev. B*, vol. 80, p. 165119, October 2009.

[75] A. C. Graham, M. Pepper, M. Y. Simmons, and D. A. Ritchie, "Anomalous spin-dependent behavior of one-dimensional subbands," *Phys. Rev. B*, vol. 72, p. 193305, November 2005.

[76] B. Trauzettel, R. Egger, and H. Grabert, "Coulomb Drag Shot Noise in Coupled Luttinger Liquids," *Physical Review Letters*, vol. 88, p. 116401, February 2002.

[77] K. Matveev and L. Glazman, "Conductance and coulomb blockade in a multi-mode quantum wire," *Physica B: Condensed Matter*, vol. 189, no. 1, pp. 266 – 274, 1993.

[78] R. De-Picciotto, M. Reznikov, M. Heiblum, V. Umansky, G. Bunin, and D. Mahalu, "Direct observation of a fractional charge," *Nature*, vol. 389, p. 162, September 1997.

[79] S. Bilodeau, "Bluefors tail design," gervaislab internal report, McGill University, 2016.

[80] F. Teyssandier and D. Prêle, "Commercially Available Capacitors at Cryogenic Temperatures," in *Ninth International Workshop on Low Temperature Electronics - WOLTE9*, (Guaruja, Brazil), 2010.

[81] K. Rasmussen and C. J.S. Olsen, "Measuring fractional quantum hall effect," bachelor's thesis, University of Copenhagen, 2013.

[82] M. T. Mihnev, J. R. Tolsma, C. J. Divin, D. Sun, R. Asgari, M. Polini, C. Berger, W. A. de Heer, A. H. MacDonald, and T. B. Norris, "Electronic cooling via interlayer Coulomb coupling in multilayer epitaxial graphene," vol. 6, p. 8105, September 2015.

[83] M. Schütt, P. M. Ostrovsky, M. Titov, I. V. Gornyi, B. N. Narozhny, and A. D. Mirlin, "Coulomb drag in graphene near the dirac point," *Phys. Rev. Lett.*, vol. 110, p. 026601, January 2013.

[84] K. Lee, J. Xue, D. C. Dillen, K. Watanabe, T. Taniguchi, and E. Tutuc, "Giant frictional drag in double bilayer graphene heterostructures," *Phys. Rev. Lett.*, vol. 117, p. 046803, July 2016.

[85] F. Lung, "Thermal Coulomb Drag in a Bi-Layer Semiconductor System," 2008.

[86] F. Lung and D. C. Marinescu, "Thermoelectric effect in a bi-layer system," *Physica E: Low-Dimensional Systems and Nanostructures*, vol. 43, no. 10, pp. 1769–1773, 2011.

[87] V. Zlatic and R. Monnier, *Modern Theory of Thermoelectricity.* OUP Oxford, 2014.

[88] A. Levchenko, "Plasmon Decay and Thermal Transport from Spin-Charge Coupling in Generic Luttinger Liquids," *Physical Review Letters*, vol. 113, p. 196401, November 2014.

[89] R. López and D. Sánchez, "Nonlinear heat transport in mesoscopic conductors: Rectification, peltier effect, and wiedemann-franz law," *Phys. Rev. B*, vol. 88, p. 045129, July 2013.

[90] C. L. Kane and M. P. A. Fisher, “Thermal Transport in a Luttinger Liquid,” no. 5, pp. 0–3, 1996.

[91] I. V. Krive, “Thermoelectric effects in a Luttinger liquid,” *Low Temperature Physics*, vol. 27, p. 821, September 2001.

[92] I. Romanovsky, I. Krive, E. Bogachek, and U. Landman, “Thermopower of an infinite Luttinger liquid,” *Physical Review B*, vol. 65, pp. 1–9, 2002.

[93] S. Apostolov, D. E. Liu, Z. Maizelis, and A. Levchenko, “Thermal transport and quench relaxation in nonlinear Luttinger liquids,” *Physical Review B*, vol. 88, p. 045435, July 2013.

[94] N. Wakeham, A. F. Bangura, X. Xu, J.-F. Mercure, M. Greenblatt, and N. E. Hussey, “Gross violation of the Wiedemann-Franz law in a quasi-one-dimensional conductor,” *Nat Commun*, vol. 2, p. 396, July 2011.

[95] L. W. Molenkamp, H. Van Houten, C. W. J. Beenakker, R. Eppenga, and C. T. Foxon, “Quantum oscillations in the transverse voltage of a channel in the nonlinear transport regime,” *Physical Review Letters*, vol. 65, no. 8, pp. 1052–1055, 1990.

[96] L. W. Molenkamp, T. Gravier, H. van Houten, O. J. A. Buijk, M. A. A. Mabesoone, and C. T. Foxon, “Peltier coefficient and thermal conductance of a quantum point contact,” *Phys. Rev. Lett.*, vol. 68, pp. 3765–3768, June 1992.

[97] O. Chiatti, J. T. Nicholls, Y. Y. Proskuryakov, N. Lumpkin, I. Farrer, and D. A. Ritchie, “Quantum thermal conductance of electrons in a one-dimensional wire,” *Phys. Rev. Lett.*, vol. 97, p. 056601, August 2006.

[98] M. Dresselhaus, G. Chen, M. Tang, R. Yang, H. Lee, D. Wang, Z. Ren, J. Fleurial, and P. Gogna, “New directions for low-dimensional thermoelectric materials,” *Advanced Materials*, vol. 19, no. 8, pp. 1043–1053.

[99] E. Pop, “Energy dissipation and transport in nanoscale devices,” *Nano Research*, vol. 3, pp. 147–169, March 2010.

[100] D. Sánchez and H. Linke, “Focus on thermoelectric effects in nanostructures,” *New Journal of Physics*, vol. 16, no. 11, p. 110201, 2014.

[101] F. Giazotto, T. T. Heikkilä, A. Luukanen, A. M. Savin, and J. P. Pekola, "Opportunities for mesoscopics in thermometry and refrigeration: Physics and applications," *Rev. Mod. Phys.*, vol. 78, pp. 217–274, March 2006.

[102] D. Li, Y. Wu, P. Kim, L. Shi, P. Yang, and A. Majumdar, "Thermal conductivity of individual silicon nanowires," *Applied Physics Letters*, vol. 83, no. 14, pp. 2934–2936, 2003.

[103] R. J. T. Bunyan, M. J. Uren, J. C. Alderman, and W. Eccleston, "Use of noise thermometry to study the effects of self-heating in submicrometer soi mosfets," *IEEE Electron Device Letters*, vol. 13, pp. 279–281, May 1992.

[104] P. G. Mautry and J. Trager, "Investigation of self-heating in vlsi and ulsi mosfets," in *International Conference on Microelectronic Test Structures*, pp. 221–226, March 1990.

[105] L. T. Su, J. E. Chung, D. A. Antoniadis, K. E. Goodson, and M. I. Flik, "Measurement and modeling of self-heating in soi nmosfet's," *IEEE Transactions on Electron Devices*, vol. 41, pp. 69–75, January 1994.

[106] K. A. Jenkins and K. Rim, "Measurement of the effect of self-heating in strained-silicon mosfets," *IEEE Electron Device Letters*, vol. 23, pp. 360–362, June 2002.

[107] K. A. Jenkins and J. Y. C. Sun, "Measurement of i-v curves of silicon-on-insulator (soi) mosfet's without self-heating," *IEEE Electron Device Letters*, vol. 16, pp. 145–147, April 1995.

[108] B. M. Tenbroek, M. S. L. Lee, W. Redman-White, J. T. Bunyan, and M. J. Uren, "Self-heating effects in soi mosfets and their measurement by small signal conductance techniques," *IEEE Transactions on Electron Devices*, vol. 43, pp. 2240–2248, December 1996.

[109] W. Jin, W. Liu, S. K. H. Fung, P. C. H. Chan, and C. Hu, "Soi thermal impedance extraction methodology and its significance for circuit simulation," *IEEE Transactions on Electron Devices*, vol. 48, pp. 730–736, April 2001.

[110] T. Y. Lee and R. M. Fox, "Extraction of thermal resistance for fully-depleted soi mosfets," in *1995 IEEE International SOI Conference Proceedings*, pp. 78–79, October 1995.

[111] M. Reyboz, R. Daviot, O. Rozeau, P. Martín, and M. Paccaud, "Compact modeling of the self heating effect in 120 nm multifinger body-contacted soi mosfet for rf circuits," *2004 IEEE International SOI Conference (IEEE Cat. No.04CH37573)*, pp. 159–161, 2004.

[112] E. Pop, D. Mann, Q. Wang, K. Goodson, and H. Dai, "Thermal conductance of an individual single-wall carbon nanotube above room temperature," *Nano Letters*, vol. 6, no. 1, pp. 96–100, 2006. PMID: 16402794.

[113] H. Maune, H.-Y. Chiu, and M. Bockrath, "Thermal resistance of the nanoscale constrictions between carbon nanotubes and solid substrates," *Applied Physics Letters*, vol. 89, no. 1, p. 013109, 2006.

[114] E. Pop, D. A. Mann, K. E. Goodson, and H. Dai, "Electrical and thermal transport in metallic single-wall carbon nanotubes on insulating substrates," *Journal of Applied Physics*, vol. 101, no. 9, p. 093710, 2007.

[115] S. Jezouin, F. D. Parmentier, A. Anthore, U. Gennser, A. Cavanna, Y. Jin, and F. Pierre, "Quantum limit of heat flow across a single electronic channel," *Science*, vol. 342, no. 6158, pp. 601–604, 2013.

[116] M. Banerjee, M. Heiblum, A. Rosenblatt, Y. Oreg, D. E. Feldman, A. Stern, and V. Umansky, "Observed quantization of anyonic heat flow," *Nature*, vol. 545, pp. 75–79, May 2017. Letter.

[117] N. Stojanovic, J. M. Berg, D. H. S. Maithripala, and M. W. Holtz, "A microelectrothermal bridge circuit with complementary parameter estimation algorithm for direct measurement of thermal conductivity," *Journal of Microelectromechanical Systems*, vol. 19, pp. 265–272, April 2010.

[118] Y. Y. Proskuryakov, J. T. Nicholls, D. I. Hadji-Ristic, A. Kristensen, and C. B. Sørensen, "Energy-loss rate of a two-dimensional electron gas measured using a mesoscopic thermometer," *Phys. Rev. B*, vol. 75, p. 045308, January 2007.

[119] V. Narayan, M. Pepper, J. Griffiths, H. Beere, F. Sfigakis, G. Jones, D. Ritchie, and A. Ghosh, "Unconventional metallicity and giant thermopower in a strongly interacting two-dimensional electron system," *Phys. Rev. B*, vol. 86, p. 125406, September 2012.

[120] V. Narayan, M. Pepper, and D. A. Ritchie, "Thermoelectric and electrical transport in mesoscopic two-dimensional electron gases," *Comptes Rendus Physique*, vol. 17, no. 10, pp. 1123 – 1129, 2016. Mesoscopic thermoelectric phenomena / Phénomènes thermoélectriques mésoscopiques.

[121] S. S. Buchholz, E. Sternemann, O. Chiatti, D. Reuter, A. D. Wieck, and S. F. Fischer, "Noise thermometry in narrow two-dimensional electron gas heat baths connected to a quasi-one-dimensional interferometer," *Phys. Rev. B*, vol. 85, p. 235301, June 2012.

[122] E. S. Tikhonov, D. V. Shovkun, D. Ercolani, F. Rossella, M. Rocci, L. Sorba, S. Roddaro, and V. S. Khrapai, "Local noise in a diffusive conductor," *Scientific Reports*, vol. 6, p. 30621, July 2016.

[123] Z. Iftikhar, A. Anthore, S. Jezouin, F. D. Parmentier, Y. Jin, A. Cavanna, A. Ouerghi, U. Gennser, and F. Pierre, "Primary thermometry triad at 6mK in mesoscopic circuits," *Nature Communications*, vol. 7, p. 12908, September 2016.

[124] D. Maradan, L. Casparis, T.-M. Liu, D. E. F. Biesinger, C. P. Scheller, D. M. Zumbühl, J. D. Zimmerman, and A. C. Gossard, "Gaas quantum dot thermometry using direct transport and charge sensing," *Journal of Low Temperature Physics*, vol. 175, pp. 784–798, June 2014.

[125] C. Altimiras, H. le Sueur, U. Gennser, A. Cavanna, D. Mailly, and F. Pierre, "Non-equilibrium edge-channel spectroscopy in the integer quantum Hall regime," *Nature Physics*, vol. 6, pp. 34–39, January 2010.

[126] V. Venkatachalam, S. Hart, L. Pfeiffer, K. West, and A. Yacoby, "Local thermometry of neutral modes on the quantum Hall edge," *Nature Physics*, vol. 8, p. 676, August 2012.

[127] P. Thulstrup, S. Bilodeau, and G. Gervais, "Designing a platform for thermoelectric transport experiments in 1d," b.s. thesis, McGill University, 2017.

[128] M. R. Tonks, D. Gaston, P. C. Millett, D. Andrs, and P. Talbot, "An object-oriented finite element framework for multiphysics phase field simulations," *Computational Materials Science*, vol. 51, no. 1, pp. 20 – 29, 2012.

[129] P. J. Price, "Hot electrons in a gaas heterolayer at low temperature," *Journal of Applied Physics*, vol. 53, no. 10, pp. 6863–6866, 1982.

[130] A. Mittal, "Electron-Phonon Scattering Rates in GaAs/AlGaAs 2DEGs below 0.5K," *Thesis*, 1996.

[131] J. Billiald, D. Backes, J. König, I. Farrer, D. Ritchie, and V. Narayan, "Determining energy relaxation length scales in two-dimensional electron gases," *Applied Physics Letters*, vol. 107, p. 022104, July 2015.

[132] B. Sothmann, R. Sánchez, and A. N. Jordan, "Thermoelectric energy harvesting with quantum dots," *Nanotechnology*, vol. 26, no. 3, p. 032001, 2015.

[133] B. Sothmann, R. Sánchez, A. N. Jordan, and M. Büttiker, "Rectification of thermal fluctuations in a chaotic cavity heat engine," *Physical Review B*, vol. 85, p. 205301, May 2012.

[134] B. Roche, P. Roulleau, T. Jullien, Y. Jompol, I. Farrer, D. A. Ritchie, and D. C. Glattli, "Harvesting dissipated energy with a mesoscopic ratchet," *Nature Communications*, vol. 6, p. 6738, April 2015.

[135] H. Thierschmann, R. Sánchez, B. Sothmann, F. Arnold, C. Heyn, W. Hansen, H. Buhmann, and L. W. Molenkamp, "Three-terminal energy harvester with coupled quantum dots," *Nature Nanotechnology*, no. August, pp. 1–6, 2015.

[136] F. Hartmann, P. Pfeffer, S. Höfling, M. Kamp, and L. Worschech, "Voltage Fluctuation to Current Converter with Coulomb-Coupled Quantum Dots," *Physical Review Letters*, vol. 114, no. 14, p. 146805, 2015.

[137] H. Thierschmann, F. Arnold, M. Mittermüller, L. Maier, C. Heyn, W. Hansen, H. Buhmann, and L. W. Molenkamp, "Thermal Gating of Charge Currents with Coulomb Coupled Quantum Dots," p. 12, February 2015.

[138] B. A. Schmidt, K. Bennaceur, S. Gaucher, G. Gervais, L. N. Pfeiffer, and K. W. West, "Specific heat and entropy of fractional quantum hall states in the second landau level," *Phys. Rev. B*, vol. 95, p. 201306, May 2017.